

Vol. 36/ 1&2
January, 2024

ISRAPS Bulletin

**TSRP-2024
SPECIAL ISSUE**



Guest Editor
Dr. Rajib Ghosh

A Publication of
Indian Society for
Radiation and Photochemical Sciences



Represents

<p>Light Conversion, UAB www.lightcon.com</p>	<ul style="list-style-type: none"> - Femtosecond Lasers - Wavelength Tunable Lasers - Microcopy Sources - Spectroscopy Systems - OPCPA Systems
<p>Ekspla, UAB www.ekspla.com</p>	<ul style="list-style-type: none"> - Nanosecond Lasers - Picosecond Lasers - Femtosecond Lasers - Ultrafast Fiber Lasers - Tunable Wavelength Lasers - Laser Spectroscopy - High Intensity Lasers - Laser Electronics
<p>Quantum Light Instruments www.qlinstruments.com</p>	<ul style="list-style-type: none"> - DPSS Nd: Yag and Nd:YLF Air-cooled, Water Free Q-Switched lasers - Air-Cooled DPSS Tunable Wavelength Q-Switched Lasers - Lasers for IR Spectroscopy - High Repetition Rate OPO
<p>QS Lasers, UAB www.qslasers.com</p>	<ul style="list-style-type: none"> - Picosecond and Sub-Nanosecond Lasers
<p>SuperLight Photonics BV www.superlightphotonics.com</p>	<ul style="list-style-type: none"> - Portable, battery operated, light weight (<1 Kg) Supercontinuum generation module (400-1000nm/100MHz/20fs)
<p>Viulase GmbH www.viulase.com</p>	<ul style="list-style-type: none"> - Diode-Pumped Ti-Sapphire Ultrafast Laser Oscillators
<p>Magnitude Instruments www.magnitudeinstruments.com</p>	<ul style="list-style-type: none"> - Benchtop Transient Absorption (TA) Spectrometers (ns-ms Spectroscopy)

Message from the President and Secretary, ISRAPS

Dear ISRAPS members,

Greetings from the Executive Council of ISRAPS!

We wish you all a very Happy New Year 2024 and take this opportunity to acknowledge the contribution of all the members for actively participating in various activities of ISRAPS.

One of the important events of ISRAPS, Trombay Symposium on Radiation & Photochemistry (TSRP-2024), is being organized in DAE Convention Centre, Bhabha Atomic Research Centre, Mumbai during January 07-11, 2024. The ISRAPS bulletin (TSRP-2024 special issue), released on this occasion, is a collection of articles on the recent developments in the field of radiation and photochemistry, from eminent scientists invited in TSRP-2024. The Executive Council (EC) of ISRAPS takes this opportunity to thank Dr. Rajib Ghosh, the Guest Editor of this special issue, for his efforts to bring out a scientifically up-to-date bulletin containing nine articles of varied interests in the field of advanced techniques in radiation and photochemistry. Support from all the contributors is also acknowledged for making this special issue very informative.

ISRAPS promotes, as you are aware, dissemination of information on frontier research in the field of radiation and photochemistry as well as in the fields of spectroscopy, nanomaterials, atmospheric chemistry, supramolecular chemistry, radiation polymerization, radiation biology, medicine and many other related subjects. In this regard, ISRAPS has been actively involved in organizing thematic discussion meetings and symposia this year. The “National Symposium on Radiation and Photochemistry (NSRP-2023),” was organized at BITS Pilani, Goa Campus during January 05-07, 2023. The symposium was a grand success in terms of sharing of knowledge in the advanced areas of radiation and photochemistry. All the young researchers were quite excited to share their research work in the poster presentation. The EC thanks all the participants, especially Prof. Mainak Banerjee from BITS Pilani, Goa Campus, for contributing to the success of NSRP-2023. Recently, we have successfully organized ISRAPS One-day Discussion Meeting on “Emerging Role of Laser in Understanding Surfaces and Interfaces” on October 21, 2023, at Department of Physics, IIT Ropar. The EC thanks Prof. Kailash C. Jena, IIT Ropar and all the speakers and participants for contributing to the success of the discussion meeting. Experts from leading research groups in the country delivered talks in their areas of research.

Once again, we wish to express our sincere gratitude to all the members of ISRAPS for their constant support and encouragement, and look forward to your valuable suggestions and active participation in the forthcoming events of ISRAPS.



Dr. Awadhesh Kumar
President, ISRAPS



Dr. (Mrs.) J. Mohanty
Secretary, ISRAPS



INDIAN SOCIETY FOR RADIATION AND PHOTOCHEMICAL SCIENCES (ISRAPS)

EXECUTIVE COUNCIL (2021-2023)

President

Dr. Awadhesh Kumar

Vice-Presidents

Prof. C. T. Aravindakumar

Prof. A. S. Kumbhar

Secretary

Dr. (Mrs.) J. Mohanty

Jt. Secretary

Dr. P. Mathi

Treasurer

Dr. Atanu Barik

Executive Members

Dr. N. Choudhury

Prof. S. K. Gundimeda

Dr. M. C. Rath

Dr. V. S. Tripathi

Dr. G. R. Dey

Dr. Virendra Kumar

Dr. (Mrs.) S. Sen Gupta

Dr. P. D. Naik

Prof. K. R. Genwa

Dr. M. Kumbhakar

Dr. P. Sharma

Dr. A. C. Bhasikuttan

Co-opted Members

Prof. Santosh Chidangil

Prof. J. P. Mittal

Dr. R. Puspallata

Prof. A. K. Singh

Prof. Anindya Datta

Dr. D. B. Naik

Dr. S. K. Sarkar

Dr. Avesh K. Tyagi

Dr. S. Dutta Choudhury

Dr. C. N. Patra

Prof. K. K. Sharma

Prof. S. Wategaonkar

Web Master

Dr. Abhishek Das

Contact details:

C/o Radiation & Photochemistry Division
Bhabha Atomic Research Centre, Mumbai-400085

E-mail: israps.secretary@gmail.com

Telephone:(022)- 25593771/25592668/25590302



ISRAPS Bulletin

A Publication of
Indian Society for Radiation and Photochemical Sciences

Editor Desk...

Dear ISRAPS Members and TSRP-2024 Delegates,

I am extremely happy to present this special issue of the ISRAPS Bulletin on the auspicious occasion of the Trombay Symposium on Radiation and Photochemistry- 2024 (TSRP-2024). Since last three decades, the TSRP conference series has been a very important forum for the radiation and photochemical researchers across the globe. Continuing the rich tradition of ISRAPS to bring forth a special issue during every TSRP, I am honored to guest-edit this special issue of the bulletin, which showcases some of the contemporary research in the area of radiation and photochemistry.

This issue presents nine articles on varied topics of current interest contributed by some of the esteemed invited speakers of TSRP-2024. The first article provides a perspective on the microscopic heterogeneity in condensed phase using various spectroscopic approaches. The second article highlights interface sensitive vibrational sum frequency generation spectroscopy of biologically relevant interaction of anesthetic molecules with lipids. The third article summarizes current understanding on emerging optical properties of manganese doped low dimensional perovskite materials. Next two articles detail spectroscopic understanding of resonance energy transfer between dyes - metal nanoparticle system and photon upconversion in lanthanide doped inorganic crystals. The sixth article attempts to showcase prospects of engineered three dimensional composite electrode materials for various catalytic applications. Aggregation induced emission based chemodosimetric detection of important analytes is elucidated in the seventh article. Finally, the last two articles cover the research in the field of radiation chemistry, highlighting the application of nuclear techniques for corrosion protection in metal alloys and use of gamma radiation and electron beam for synthesis of semiconducting nanoparticles in aqueous solution.

These interesting topics provide a great deal of information in the respective field of the research area. I believe these informative articles will stimulate thought-provoking ideas to take up challenging problems to address contemporary problems in both basic and applied research in the field of Radiation and Photochemistry. On behalf of ISRAPS, I sincerely acknowledge the active cooperation from all the contributors to this issue. I take this opportunity to thank ISRAPS for entrusting me with the guest editorial responsibility.

Rajib Ghosh (Guest Editor)
Radiation & Photochemistry Division
Bhabha Atomic Research Centre, Mumbai-85, INDIA



Contents

Message from the President and Secretary, ISRAPS	i
Editor's Desk	iii
Perspective on Heterogeneity through Spectroscopic Approaches <i>Pratik Sen</i>	1
Understanding the Interaction of Anesthetic Molecule with Lipids Using the Vibrational Sum Frequency Generation Spectroscopy <i>Biswajit Biswas, Prashant Chandra Singh</i>	10
Mn-doping in Low-dimensional Perovskites for Tunable Optical Properties <i>Tushar Debnath</i>	14
Understanding the Resonance Energy Transfer between Fluorescent Bimetallic Nanoparticles and Organic Dye molecules <i>AmitAkhuli, Aditi Mahanty, Sahadev Barik, Amita Mahapatra Debabrata Chakraborty, and Mology Sarkar</i>	24
Broad Photon Upconversion in Lanthanide Doped Inorganic Crystals <i>Annu Balhara, and Santosh K. Gupta</i>	35
Engineered 3D Composite based Electrodes for Efficient Catalysis <i>Indra Sulania, Ambuj Tripathi, Ranjeet K Karn, Elham Chamanehpour, Ajani Lakmini Jayarathna and Y K Mishra</i>	50
A Chromene-Tetraphenylethylene AIEgen-based Chemodosimeter for Highly Selective Turn-off Detection of Bisulfite Ions and Nitroaromatics <i>Akhil A. Bhosle, Mainak Banerjee, Viraj G. Naik, Amrita Chatterjee</i>	58
Application of nuclear technique for development of inhibitors for corrosion protection of different alloys <i>Jayashree Biswal, V. K. Sharma, H. J. Pant</i>	70
Radiation-induced synthesis of semiconductor nanoparticles in aqueous solution - a promising method <i>A. Guleria and M. C. Rath</i>	76

Perspective on Heterogeneity through Spectroscopic Approaches

Pratik Sen

Department of Chemistry, Indian Institute of Technology Kanpur, Kanpur 208 016, UP, India

Abstract

Molecular level structure and dynamics decide the functionality of a solvent. One fascinating aspect of such structure and dynamics is the heterogeneity. Generally, dynamic heterogeneity in a media is recognized by the viscosity decoupling of the dynamics (i.e., $\tau_x \propto \left(\frac{\eta}{T}\right)^p$ with $p \neq 1$). In this review, a physical understanding of such dynamic heterogeneity is presented. We have recognized that though dynamically heterogeneous media shows viscosity decoupling, the vice-versa is not automatically true. Therefore, one should be cautious in relating viscosity decoupling to dynamic heterogeneity. We developed two novel analytical methods to interrogate this issue. The first one is based on selective probing of differently diffusing sub-populations and the second one is based on the photo-selection of different subpopulations in a heterogeneous system. Realizing that the molecular origin of dynamic heterogeneity is structural heterogeneity, we also have developed a new fluorescence method, i.e. shift of excitation spectra at the blue edge of emission (BEEms), as a new methodology to probe structural or spatial heterogeneity.

Key words: Dynamic heterogeneity, Spatial heterogeneity, Viscosity decoupling, REES, BEEms

The word heterogeneity literally means diverse or different. One can easily sense heterogeneity if one mixes two or more solid substances. However, in the case of liquid mixtures, heterogeneity (if any) is challenging to comprehend. Apparently, it seems to be homogenous. Homogeneity refers to the state of being similar kind or having a uniform structure or composition throughout. In chemistry, homogeneity is an essential concept in the study of solutions, where it refers to the uniform distribution of solute molecules in the solvent. Typical solvents are said to be homogeneous as the properties (such as viscosity, diffusion coefficient, density, polarity, etc.) measured in any region in space (with a length scale larger than the molecular dimension) are the same. On the other hand, heterogeneous media have non-uniform composition and properties. Our recent understanding proposed that in heterogeneous media, microdomains are formed, wherein the dynamics is different from the rest of the medium, and different microdomains relax at different rates. Moreover, these microdomains

are interconvertible with some timescale. These microdomains facilitate/hinder diffusion but do not affect the relaxation of the entire system. Hence, diffusion and relaxation are decoupled, and the entire system is said to have dynamic heterogeneity. Proof of such dynamic heterogeneity comes from the breakdown of Stokes-Einstein (SE) or Stokes-Einstein-Debye (SED) relationships when the measurement time is smaller or comparable to the inter-region fluctuation time scale, and of course, when the signal is acquired from specific microdomains.

The driving force for the formation of such microdomains is presumably the force imbalance. Even in the simplest chemical system, if we think about how the molecules are arranged and how different forces act between them, it will not be tough to imagine why there should be a force imbalance. In fact, imagining a force-balance condition and a perfect homogenous system will be difficult. If this is the case, why are most of the systems homogenous and only some heterogeneous? The question is probably not

rightly framed. It should be “Why does most of the system appear or seem to be homogenous?”. There is a difference between being homogenous and appearing to be homogenous. If an experiment detects heterogeneity, it is confirmed that heterogeneity is present in the system. However, if one observes homogeneity in an experiment, it may be possible that the experimental technique cannot detect heterogeneity.

The tricky part is to have an experimental method for which information from a very local environment can be obtained. Fluorescence experiments provide exactly this opportunity owing to their unmatched spatial and temporal resolution. Different types of fluorescence experiments are available that provide information from different times and length scales. For example, fluorescent anisotropy measurement provides information about the rotational dynamics in ps-ns timescale and nm length scale. Diffusion measurement (employing fluorescence correlation spectroscopy) provides information about the translational dynamics in μs -ms timescale and μm length scale. SE and SED equations relate how these dynamics depend on the viscosity and temperature of the medium as

$$\tau_t = \frac{1}{D_t} = \frac{6\pi\eta r_s}{kT}$$

$$\tau_r = \frac{1}{D_r} = \frac{8\pi\eta r_s^3}{kT}$$

where, k is the Boltzmann's constant, η is the viscosity, and r_s is the spherical radius of the solute molecule. Thus, a plot of $\log(\tau)$ vs $\log\left(\frac{\eta}{T}\right)$ should yield a straight line with a unity slope.

$$\log(\tau) = \log\left(\frac{\eta}{T}\right) + C \quad (3)$$

However, in several systems, the dynamics are fractional power dependent on the temperature-reduced viscosity, $\left(\frac{\eta}{T}\right)^p$. In such cases, the relationship is best described by^{1,2,3,4}

$$\log(\tau) = p \log\left(\frac{\eta}{T}\right) + C \quad (4)$$

where p . This means that the dynamics (translation, rotation, etc.) are decoupled from the medium viscosity. This decoupling of dynamics is indicative of the presence of dynamics heterogeneity. Although the “decoupling” has been used in the literature to indicate the breakdown of SE/SED relationships, it does not mean that the diffusion is completely independent of viscosity; instead, it is differently coupled.

Back in 1969, Goldstein argued that diffusion in liquids occurs by different mechanisms at different temperature ranges.⁵ At low temperatures (near glass transition temperature), the molecule translates by hopping and needs to cross a substantial potential energy barrier to reach from one free energy well to another. Moreover, the activation energy barrier has a distribution that leads to heterogeneous dynamics in the system. Whereas, at high temperatures, it is mainly a free diffusion.⁶ Later, in 1992, Fujara *et al.* reported a dramatically different temperature dependency of translational and rotational dynamics of orthoterphenyl.⁷ In 1995, Tarjus *et al.* explained this by considering spatially heterogeneous dynamics through microdomain formation.⁸ Following these initial works, the viscosity decoupling has been considered to be a signature of dynamic heterogeneity and has been detected in glass-forming liquids,⁸⁻⁹ polymers,¹⁰ ionic liquids,¹¹⁻¹³ deep eutectic solvents,¹⁴⁻¹⁶ and binary solvent mixtures.¹⁷⁻¹⁸ It has been proposed that in such cases, the constituents form clusters, which are locally preferred conformations in terms of the free energy, and relax differently than the entire system. Despite of considerable effort towards the understanding of viscosity decoupled dynamics and dynamic heterogeneity, the picture is still unclear. Also, there was no analytical expression to estimate dynamic heterogeneity, and a slope > 1 of the log-log plot has never been identified as the presence of dynamic heterogeneity.

In 2021, we took a simple model where microdomain formation inside the liquid medium

is considered. A visualization of this situation is given in figure 1 with domains represented by different colours denoting different relaxation rates. We conjectured that the SE relationship is upheld separately in both the bulk medium and the microdomains but that the activation energy of the viscous flow differs in these two scenarios.¹ We had demonstrated that, in this case, the SE relationship changed to

$$\log(\tau_\mu) = \log\left(\frac{\eta_{bulk}}{T}\right) + \left(\frac{\Delta E}{2.303RT}\right) + C \quad (5)$$

where $\Delta E = E_\mu - E_{bulk}$. The presence of the second term on the right-hand side of equation 5 leads to viscosity decoupling (see figure 2). Consequently, all that is needed to anticipate

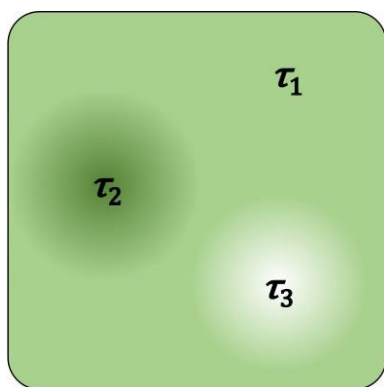


Figure 1. Depiction of dynamically heterogeneous systems having microdomains. One microdomain is relaxing with time constant₁, and the other is relaxing with time constant₂. We might observe heterogeneous dynamics (i) if τ_1 and τ_2 are sufficiently different, (ii) the exchange rate between τ_1 and τ_2 is slow compared to the probing time, and (iii) the experiment acquires data from the microdomain.

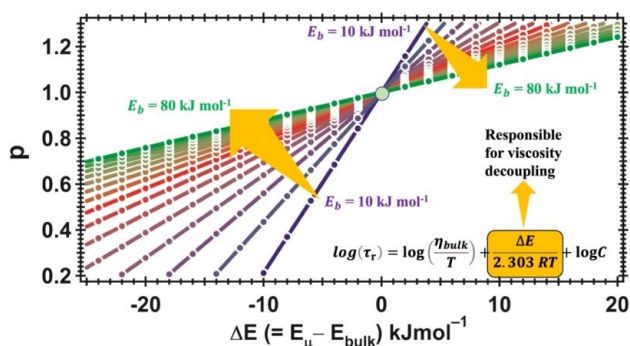


Figure 2. A representation of the analytical prediction of dynamic heterogeneity, viscosity decoupling and its relationship with the activation energy of the viscous flow.

the p-value is the value. A viscometer made it simple to obtain, and temperature-dependent fluorescence detection of a barrierless molecular rotor allowed us to obtain . In this manner, dynamic heterogeneity might be predicted without the need for dynamic experiments. Using this method, we could predict the -values for three deep eutectic solvents, and the results agreed with previous experimental findings. This suggests that probing the dynamics in micro regions is necessary to observe the heterogeneity. Previously, Mazza *et al.* in 2007 tagged faster and slower moving molecules separately using MD simulation,¹⁹ which leads us to think that if we can selectively probe different sub-populations of the system e xperimentally, interesting results could be obtained. If different populations behave similarly, there should not be any heterogeneity in the system.

We realized that relating viscosity decoupling to dynamic heterogeneity requires critical attention. While dynamically heterogeneous media will show a breakdown from the SE/SED relationship ($p \neq 1$), the vice-versa is not automatically true as the decoupling may also originate from the deviation of the basic assumption of SE/SED relations like, solvent is continuum, solute is spherical, chargeless and rigid, solute translate only a tiny distance in each step, diffusion is stochastic, etc.² For translational dynamics, we devised a unique approach using single molecular level fluorescence correlation spectroscopy (FCS) to identify dynamic heterogeneity effectively. Along with the unmatched spatial resolution of fluorescence, the requirement of extremely low probe concentration (nM level) in the FCS study might be beneficial in selective sampling from micro-heterogenous regions. Our approach was based on detecting the temperature evolution of distinct diffusion time regimes in a heterogeneous system from a single measurement. We hypothesized that if the system is not dynamically heterogeneous, the -values for different diffusion time regimes will be the same, even if the value of

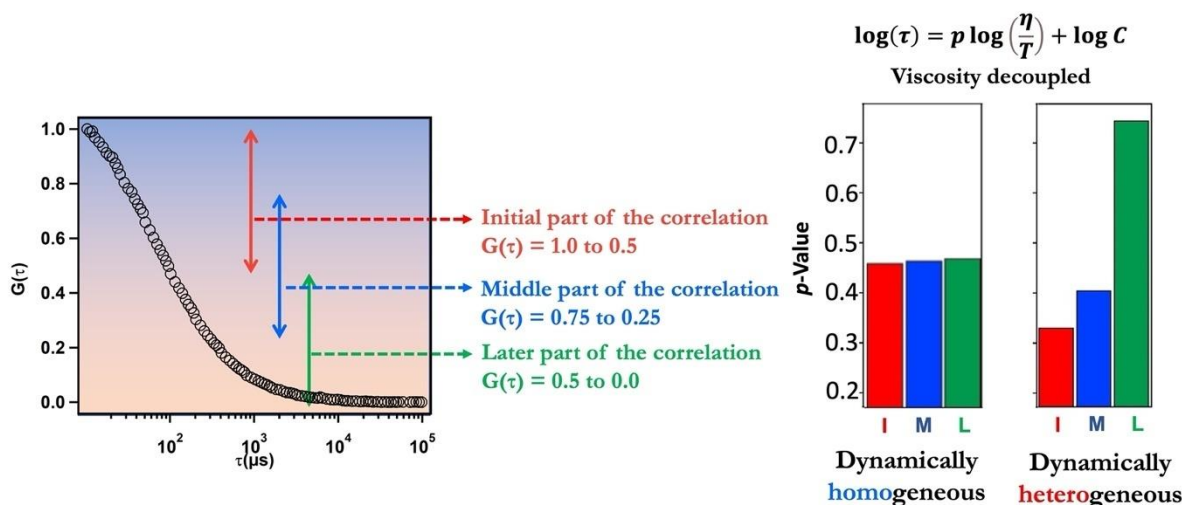


Figure 3. Different portions of the fluorescence intensity autocorrelation function from FCS used for analysis are presented. The entire correlation contains information of all diffusing timescales. The initial part (red arrow), middle part (blue arrow) and later part (green arrow) of the correlation are selected to put weightage on the different diffusion times in a heterogeneous system. The right panels represent viscosity decoupled dynamics. The subpopulation dependent decoupling suggests the existence of dynamically heterogeneous media.

significantly differs from unity (Figure 3).² Among the four studied systems, two were complex deep eutectic solvents (DESs), and the other two were molecular liquids, all exhibiting viscosity decoupling, albeit varying degrees, according to a plot of $\log(\tau)$ vs. $\log(\frac{\eta}{T})$. This apparently suggests the presence of dynamic heterogeneity in all four systems. However, our analysis indicates that two DESs are dynamically heterogeneous, whereas two molecular liquids, dimethylformamide and glycerol, are dynamically homogenous. We argued that, in contrast to the conventional approach, differences in the degree of viscosity decoupling for differently diffusing

subpopulations might be a superior criterion to identify dynamic heterogeneity, and this concept can be extended to rotational diffusion as well.

Consequently, we applied a similar concept in rotational dynamics as well. We recognize that a solvatochromic probe will be solvated to varying degrees in distinct microdomains, resulting in diverse subpopulations, and the excitation/emission wavelength dependent measurements can be used to select these subpopulations (Figure 4). We expected that the dynamics of a homogeneous system might (or might not) exhibit viscosity decoupling, but the

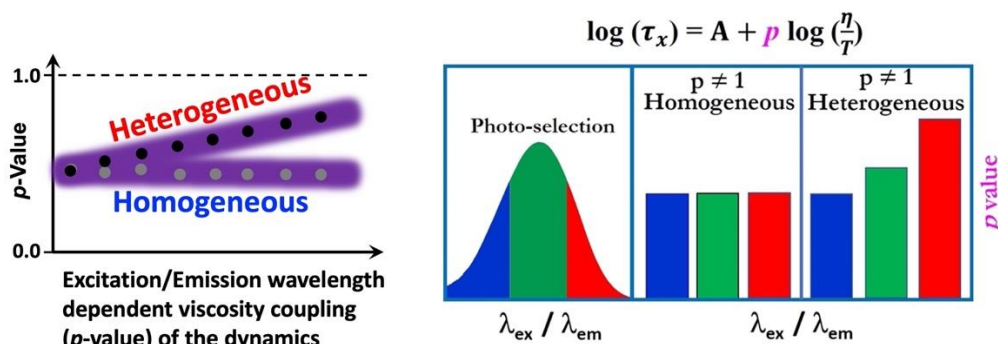


Figure 4. Hypothesis describing a Way Out to Achieve a better Relationship between Dynamic Heterogeneity and Viscosity Decoupling. Photo selection of different subpopulations can be achieved either by varying the excitation or emission wavelength.

level of decoupling should not alter at different excitations (or at different emissions). On the other hand, in a heterogeneous media, the extent of viscosity decoupling (ν -value) should vary with excitation (or emission). We investigated four different solvent media as a proof of concept. Overall, we suggest that the difference in ν -value for the dynamics of different subpopulations may be a superior criterion for probing heterogeneity.³

The discussion of heterogeneity so far is about dynamic heterogeneity. If one thinks about why dynamics are heterogeneous, the probable answer that comes to mind is structural heterogeneity. Direct experimental probing of such structural heterogeneity is rare,^{20,21} tough and does not always correlate well with dynamical heterogeneity.^{22,23} However, if there is heterogeneity in dynamics, something must

also be present in the structure. In figure 5, effort was made to distinguish different dynamical regions of figure 1 by lines. If an experiment can confirm the presence of such areas having different structural arrangements, then spatial heterogeneity will be established. However, if an experiment cannot confirm the presence of these lines, that does not mean that these regions are absent. The difference in the structural signal could be too subtle to distinguish themselves experimentally. This structural heterogeneity is called spatial heterogeneity. In the literature, dynamic and spatial heterogeneity are often found to be used interchangeably, like “Spatially Heterogeneous Dynamics” and “Spatio-Temporal Heterogeneity”.^{22,23} Thus, one can very much use “spatial heterogeneity” in place of “dynamic heterogeneity” if the spatial aspect of heterogeneity is paramount.

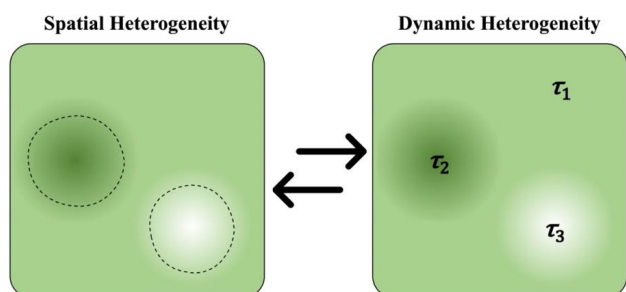


Figure 5. Possible relation between spatial and dynamic heterogeneity.

The easiest way to probe structural heterogeneity is the fluorescence based red edge excitation shift (REES) experiment.^{24,25} Generally, the fluorescence spectrum does not depend on the excitation wavelength (Kasha’s rule). However, in some cases (solvatochromic fluorophores), one observes excitation dependent emission, especially when excited at the red edge of the absorption spectrum. This is known as

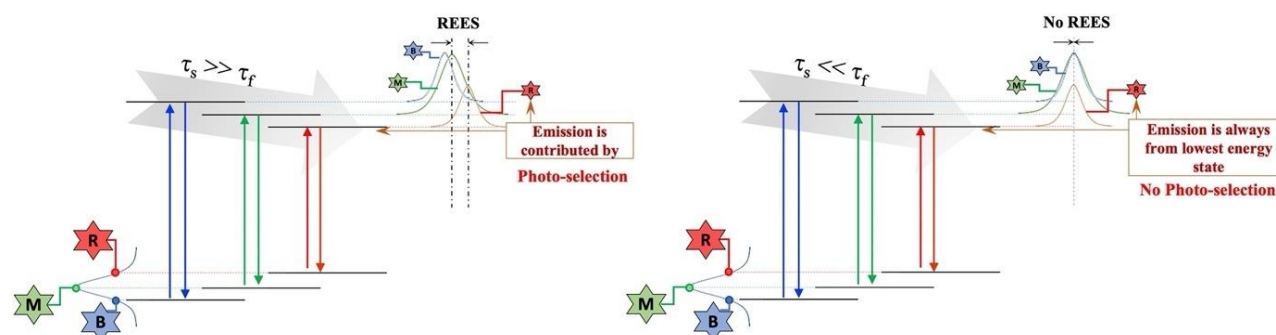


Figure 6. A schematic description of the molecular origin of REES. In a heterogeneous distribution of fluorophore, photoexcitation at the blue edge (blue line, B), absorption maxima (green line, M), and red edge (red line, R) will excite the molecules at different excited states. When the solvent relaxation is much slower (left panel), emission occurs before complete solvation. In this case, the emission occurs from a partially solvent-relaxed state for the high-energy excitation. As a result, we observe REES. When the solvent relaxation is much faster than the excited-state lifetime (right panel), emission occurs mainly from the completely solvated state, irrespective of the excitation. In this case, there is no REES. Although the extent of heterogeneity is the same in both cases, observed REES is different and is controlled by τ_f/τ_s ratio.

REES. The molecular origin of REES lies in the heterogeneous distribution of the excitation and emission energy of the fluorophore.⁴ In such a scenario, excitation at different wavelengths along the absorption spectrum raises the molecules to differently solvated excited states. In the case of red edge excitation, only the highly solvated fluorophores can be photo-selected. If solvent relaxation (τ_s) is faster than the excited state lifetime (τ_f), then emission always occurs from the completely solvated state, and REES is not observed. However, for slow solvent relaxation ($\tau_f < \tau_s$), fluorescence might occur before the solvent relaxation is complete, and one should observe REES (Figure 6). Therefore, the presence of REES means that there is a spatial heterogeneity, but the absence of REES does not guarantee that there is no spatial heterogeneity as REES severely depends on the τ_f/τ_s ratio of the probe.⁴

Recently, we developed a novel edge effect leading to the shift of excitation spectra at the blue edge of the emission (we named this BEEms) to perceive the structural heterogeneity that does not suffer from τ_f/τ_s the problem.⁴ The excitation spectra depict the range of excitation wavelength that can make the fluorophore fluorescent. At $t = 0$, the contribution comes only from the Frank-Condon state which depends on the emission wavelength

$$E(\lambda_{em}, t = 0) = E_{fc}(\lambda_{em}) \quad (6)$$

However, over a longer time, the spectrum should contain contributions from all the species. Considering a two-state model (where population decay due to excited state lifetime is not considered), the situation can be expressed as

$$E(\lambda_{em}, t = \infty) = \frac{E_{fc}(\lambda_{em}) + E_{sol}(\lambda_{em})}{2} \quad (7)$$

The time evolution of the excitation spectrum under this condition can be written as

$$E(\lambda_{em}, t) = \frac{E_{fc}(\lambda_{em}) + E_{sol}(\lambda_{em})}{2} + \left[E_{fc}(\lambda_{em}) - \frac{E_{fc}(\lambda_{em}) + E_{sol}(\lambda_{em})}{2} \right] e^{-\frac{t}{\tau_s}} \quad (8)$$

In this case, the population decay can be expressed as

$$P(\lambda_{em}, t) = P_0(\lambda_{em}) \frac{1/\tau_s}{1/\tau_f - 1/\tau_s} \left(e^{-\frac{t}{\tau_s}} - e^{-\frac{t}{\tau_f}} \right) \quad (9)$$

Where P_0 is the total number of excited state species at time $t = 0$ that depends upon the emission wavelength (λ_{em}). Therefore, the steady state excitation spectrum can be represented as

$$Ex^{SS}(\lambda_{em}) = \int_0^\infty [E(\lambda_{em}, t) P(\lambda_{em}, t)] dt \quad (10)$$

Putting the value of $E(\lambda_{em}, t)$ from equation 8 and from equation 9, equation 10 yields $Ex^{SS}(\lambda_{em}) =$

$$P_0(\lambda_{em}) E_{sol}(\lambda_{em}) \tau_f \left[\frac{1}{4 \left(1 - \frac{\tau_f}{\tau_s}\right)} - \frac{1}{2 \left(\frac{\tau_s}{\tau_f} - 1\right)} + \frac{1}{2 \left(1 - \frac{\tau_f}{\tau_s}\right) \left(1 + \frac{\tau_s}{\tau_f}\right)} \right] + P_0(\lambda_{em}) E_{fc}(\lambda_{em}) \tau_f \left[\frac{3}{4 \left(1 - \frac{\tau_f}{\tau_s}\right)} - \frac{1}{2 \left(\frac{\tau_s}{\tau_f} - 1\right)} - \frac{1}{2 \left(1 - \frac{\tau_f}{\tau_s}\right) \left(1 + \frac{\tau_s}{\tau_f}\right)} \right] \quad (11)$$

When, $\frac{\tau_f}{\tau_s} \ll 1$

$$Ex^{SS}(\lambda_{em}) = P_{fc}(\lambda_{em}) \tau_f \left[\frac{1}{2} E_{eq}(\lambda_{em}) + \frac{1}{2} E_{fc}(\lambda_{em}) \right] \quad (12)$$

and, when $\frac{\tau_f}{\tau_s} \gg 1$

$$Ex^{SS}(\lambda_{em}) = P_{fc}(\lambda_{em}) \tau_f \left[\frac{1}{4} E_{eq}(\lambda_{em}) + \frac{3}{4} E_{fc}(\lambda_{em}) \right] \quad (13)$$

In both the limiting cases, the excitation maxima depend on the emission wavelength. On the other hand, in the case of REES, the analytical form can be written as

$$Em^{SS}(\lambda_{ex}) = \tau_f P_0(\lambda_{ex}) \left[I_{sol} + I_{fc}(\lambda_{ex}) \frac{1}{1 + \frac{\tau_f}{\tau_s}} - I_{sol} \frac{1}{1 + \frac{\tau_f}{\tau_s}} \right] \quad (14)$$

When $\tau_s \ll \tau_f$,

$$Em^{SS}(\lambda_{ex}) = \tau_f P_0(\lambda_{ex}) I_{sol}. \quad (15)$$

Therefore, irrespective of the excitation wavelength, emission originates from the completely solvated state when $\tau_s \ll \tau_f$. Thus, no REES will be observed. However, when $\tau_s \gg \tau_f$, the steady state spectrum becomes

$$Em^{SS}(\lambda_{ex}) = \tau_f P_0(\lambda_{ex}) I_{fc}(\lambda_{ex}). \quad (16)$$

In this case, emission does depend on the Frank-Condon state and, therefore, will depend on the excitation wavelength. We simulated how the steady state excitation and emission spectrum changes as a function of $\frac{\tau_f}{\tau_s}$ ratio according to equations 11 and 14, respectively, which are shown in figures 7. Here, the Frank-Condon and solvated states are represented as a Gaussian function, $e^{-\frac{(\lambda-\lambda_{max})^2}{\sigma^2}}$, with $\lambda_{max} = 400$ nm and 430 nm, respectively, and $\sigma = 30$ nm. We also consider that there is no inherent Stokes shift.

Visual inspection of figure 7 suggests that even if there is a difference between $I_{fc}(\lambda_{ex})$ and I_{eq} , REES can not be observed when is higher. This means that REES sense the heterogeneity fairly only when $\frac{\tau_f}{\tau_s}$ is lower (as in the case of viscous liquid or protein core) but fails miserably at higher $\frac{\tau_f}{\tau_s}$ (as in the case of most of the molecular liquids and proteins in the denatured state). However, if there is a difference between $E_{fc}(\lambda_{em})$ and E_{eq} , BEEms can be observed even when $\frac{\tau_f}{\tau_s}$ is higher, and

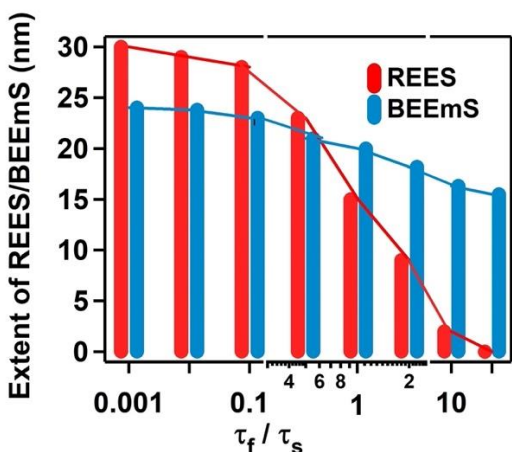


Figure 7. At the same degree of heterogeneity (a difference of 30 nm in the spectral maxima of FC state and equilibrium state), REES and BEEms are plotted as a function of $\frac{\tau_f}{\tau_s}$.

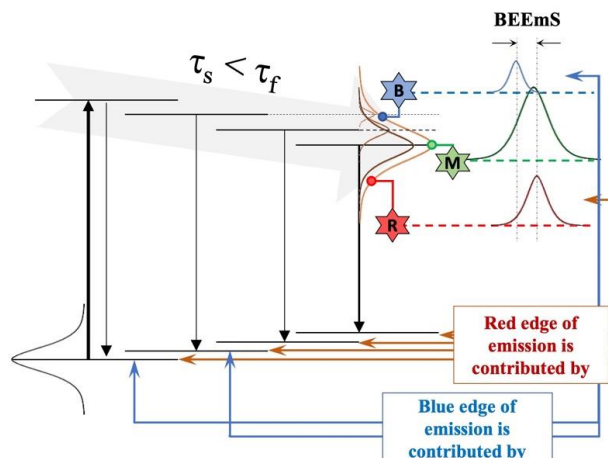


Figure 8. A schematic description of the molecular origin of BEEms when the solvent relaxation is much faster. Emission, in this case, occurs from the complete solvated state irrespective of the excitation wavelength (No REES in this case; see figure 6). The excitation spectrum taken at the emission maximum and at the red edge will have the contribution mainly from the highly solvated (red) species. The excitation spectrum recorded at the blue edge of the emission spectrum has the contribution mainly from the poorly solvated (blue) state with little assistance from moderately solvated (green) and highly solvated (red) species. In such a scenario, one sees a gradual shift in the excitation spectrum to the blue side as the probing emission wavelength shifts toward the blue edge of the emission spectrum. Even when emission originates primarily from the complete solvated state, the feeble contribution from the poorly solvated state can be photo selected, and BEEms can be observed.

BEEms can sense heterogeneity irrespective of $\frac{\tau_f}{\tau_s}$ value. The energy diagram representation of BEEms is presented in figure 8. When the solvent relaxation time is greater than the excited state lifetime, one would see that the emission from the solvated state is mainly contributed by the moderately solvated species. Here, the solvent relaxation time is greater than the fluorescence lifetime, so the emission does take place before the relaxation. On the other hand, the emission at the blue edge of the emission spectrum will generate an excitation spectrum that is similar to the absorption spectrum of the less solvated molecules. Thus, there will be a shift of excitation spectra depending on the emission wavelength.⁴For the case of faster solvent relaxation time than the excited state lifetime, the

situation in BEEemS remains the same, and one would observe a shift in the excitation spectrum, and heterogeneity can be estimated.⁴

We used BEEemS to measure heterogeneity where REES failed. The usefulness of BEEemS and its recent applications are

- (i) It is based on steady-state fluorimetry. Due to vast availability and simplicity in experiment and analysis, this method has the potential to be routinely used.
- (ii) It does not depend on environmental rigidity (unlike the famous REES). BEEemS depends on solvation feebly and can be utilized positively in many directions. Some taken examples are (a) It detects spatial heterogeneity in a so-called homogeneous deep eutectic solvent, (b) It furnishes that heterogeneity in the denatured state of a protein actually increases, which is expected from the textbook knowledge of protein folding-funnel hypothesis, yet very difficult to demonstrate experimentally.
- (iii) The available techniques, in general, cannot be applied to the multi domain proteins that form more than 70% of total proteins in Eukaryotes. Our method overcomes this drawback by providing domain-specific information of the heterogeneity.

Conclusion:

This review attempts to give a comprehensive understanding on heterogeneity based on our most current investigations. A simple analytical model was constructed and validated to understand and predict dynamic heterogeneity in a media. We further argued that viscosity decoupling could be observed only if information of dynamics can be selectively acquired from microheterogeneous regions. We identified that while dynamically heterogeneous media will show a breakdown from the Stokes-Einstein (SE) relationship ($p \neq 1$), the vice-versa is not automatically true. Therefore, one should be cautious in relating viscosity decoupling to dynamic heterogeneity. We developed two novel analyses to determine dynamic heterogeneity from viscosity decoupling

in a better way. One analysis is based on selective probing of different diffusion time regimes in a heterogeneous system from a single measurement and on photo-selection of different subpopulations in a heterogeneous solvent. Next, the molecular level understanding of the source of dynamic heterogeneity has been correlated with structural heterogeneity. To get an actual estimate of the structural or spatial heterogeneity, the shift of excitation spectra at the blue edge of emission (BEEemS) has been presented as a new methodology. This newly developed method has some unique advantages, and owing to its experimental simplicity and analysis, it is expected to be used routinely by various scientific communities.

References:

1. Das, N. and Sen, P., *Physical Chemistry Chemical Physics*, **2021**, 23(29), 15749-15757.
2. Das, N., Subba, N. and Sen, P., *Journal of Photochemistry and Photobiology A: Chemistry*, **2023**, 436, 114361.
3. Tarif, E., Das, N. and Sen, P., *The Journal of Physical Chemistry B*, **2023**, 127(32), 7162-7173.
4. Das, N., Khan, T. and Sen, P., *Chemical Physics*, **2023**, 112138.
5. Goldstein, M., *The Journal of Chemical Physics*, **1969**, 51(9), 3728-3739.
6. Kumar, P., Buldyrev, S.V., Becker, S.R., Poole, P.H., Starr, F.W. and Stanley, H.E., *Proceedings of the National Academy of Sciences*, **2007**, 104(23), 9575-9579.
7. Fujara, F., Geil, B., Sillescu, H. and Fleischer, G., *Zeitschrift für Physik B Condensed Matter*, **1992**, 88, 195-204.
8. Tarjus, G. and Kivelson, D., *The Journal of Chemical Physics*, **1995**, 103(8), 3071-3073.
9. Chen, B., Sigmund, E.E. and Halperin, W.P., *Physical Review Letters*, **2006**, 96(14), 145502.
10. Adhikari, M., Karmakar, S. and Sastry, S., *The Journal of Physical Chemistry B*, **2021**, 125(36), 10232-10239.
11. Patra, S. and Samanta, A., *The Journal of Physical Chemistry B*, **2012**, 116(40), 12275-12283.
12. Yamaguchi, T., Mikawa, K.I., Koda, S., Fujii, K., Endo, H., Shibayama, M., Hamano, H. and Umebayashi, Y., *The Journal of Chemical Physics*, **2012**, 137(10), 104511.
13. Wu, E.C., Kim, H.J. and Peteanu, L.A., *The Journal of Physical Chemistry B*, **2017**, 121(5), 1100-1107.
14. Khan, T., Tarif, E., Awano, Y., Lozada, L.S., Das, N., Tominaga, K. and Sen, P., *Journal of Molecular Liquids*, **2023**, 389, 122882.
15. Tarif, E., Mondal, J. and Biswas, R., *The Journal of Physical Chemistry B*, **2019**, 123(44), 9378-9387.
16. Subba, N., Das, N. and Sen, P., *The Journal of Physical Chemistry B*, **2020**, 124(31), 6875-6884.

17. Chatteraj, S., Chowdhury, R., Ghosh, S. and Bhattacharyya, K., *The Journal of Chemical Physics*, **2013**, 138(21), 214507.
18. Gazi, H.A.R. and Biswas, R., *The Journal of Physical Chemistry A*, **2011**, 115(12), 2447-2455.
19. Mazza, M.G., Giovambattista, N., Stanley, H.E. and Starr, F.W., *Physical Review E*, **2007**, 76(3), 031203.
20. Weeks, E.R., Crocker, J.C., Levitt, A.C., Schofield, A. and Weitz, D.A., *Science*, **2000**, 287(5453), 627-631.
21. Berthier, L., Biroli, G., Bouchaud, J.P., Cipelletti, L., Masri, D.E., L'Hôte, D., Ladieu, F. and Pierno, M., *Science*, **2005**, 310(5755), 1797-1800.
22. Richert, R., 1996. *Physical Review B*, **1996**, 54(22), 15762.
23. Ediger, M.D., *Annual Review of Physical Chemistry*, **2000**, 51(1), 99-128.
24. Hu, Z. and Margulis, C.J., *Proceedings of the National Academy of Sciences*, **2006**, 103(4), 831-836.
25. Demchenko, A.P., *Luminescence: the journal of biological and chemical luminescence*, **2002**, 17(1), 19-42.



Pratik Sen earned his MSc in 2001 from Visva-Bharati University and PhD in 2006 from the Indian Association for Cultivation of Science, Kolkata, India. After post-doctoral research at the Molecular Spectroscopy Laboratory, RIKEN, Japan, he joined the Department of Chemistry, Indian Institute of Technology Kanpur, as an assistant professor in December 2008 and became a full professor in November 2018. He is currently holding the Poonam and Prabhu Goel chair at IIT Kanpur. His primary research interest is to gain physical insight into how dynamics in various length and timescale control chemistry. The studied system ranges from small molecules to complex biosystems to simple solutions. His group mainly uses ultrafast laser and single molecular level spectroscopies as a tool for this endeavour. Further, he intends to develop new methodologies in fluorescence spectroscopy. Dr. Sen has received several awards and recognition for his research, which includes the Young Scientist Medal from Indian National Science Academy (INSA), New Delhi in 2012; Young Faculty Research Fellowship from IIT Kanpur, 2015-2017; Member, Indian National Young Academy of Sciences (INAYAS), 2016-2020; Young Faculty Research Fellowship, Ministry of Electronics & Information Technology, Government of India in 2018, Fellowship of the Royal Society of Chemistry (FRSC) in 2021 and Bronze Medal of Chemical Research Society of India (CRSI) in 2021.

Understanding the Interaction of Anesthetic Molecule with Lipids Using the Vibrational Sum Frequency Generation Spectroscopy

Biswajit Biswas, Prashant Chandra Singh*

*School of Chemical Sciences, Indian Association for the Cultivation of Science,
Jadavpur, Kolkata 700032 India
sppcs@iacs.res.in

Abstract

The interaction of the anesthetic molecules with lipids associated with the membrane is important to understand its action mechanism. In this study, we have performed the vibrational sum frequency generation (VSFG) study of the negatively charged air/DPPG/water and zwitterionic air/DPPC/water interface in the absence and presence of propofol has been performed. The OH stretch of water at the air/DPPG/water interface decreases with the addition of propofol which has been assigned to the reorganization of the hydrogen bonding of water molecules with the OH group of propofol. In contrast, the change in the OH stretch of water is marginal on the addition of the propofol which indicates that the probability of the interaction of propofol interaction with zwitterionic lipid is slim. This study indicates that propofol prefers to interact with the negatively charged lipid rather than the zwitterionic lipid associated with the membranes.

Introduction:

Anesthetic molecules are an important component of medical treatment, particularly in surgery. Anesthetic molecules disturb the nerve signal from the brain and body without inducing any pain and create a reversible state of unconsciousness. 2, 6-di-isopropylphenol (propofol, Figure 1) is frequently used anesthetic drug due to the favorable pharmacokinetic and pharmacodynamic profile.¹ Propofol is used in several medical applications such as mechanical ventilation, intensive care unit, radiation therapy, and magnetic resonance imaging due to its less side effects than inhaler anesthetic molecules. The intrusion of propofol into the bloodstream depends on its diffusivity, partition coefficient, and acid-base equilibrium.²

Despite the use of general anesthetic molecules, its action mechanism is yet not well established. There are few candidates which have been recognized as possible targets of the anesthetic molecules. Sodium channels are one of the primary targets that anesthetic molecules

affect. Proposed mechanistic theories suggest that propofol can target membrane lipids, water, membrane-associated enzymes, and ion channels.³ It has been shown that Local anesthetics may interact with membrane lipids to change the fluidity, order, microviscosity, and permeability of membranes and also influence the electrostatic potential across lipid bilayers, which may affect the functions of voltage-gated ion channels.⁴ Indeed, it has been recently suggested that the role of membrane lipids and specific membrane components in anesthetic mechanisms should be reverified.⁴

In this study, we have studied the effect of propofol on the interfacial water beneath the negatively charged (1, 2-dipalmitoyl-sn-glycero-3-phospho-rac-1-glycerol sodium salt (DPPG)) and zwitterionic (1,2-dipalmitoyl-sn-glycero-3-phosphocholine (DPPC)) phospholipids (Figure 1) using the state of the art vibrational sum frequency generation (VSFG) technique. It is well established that the VSFG technique provides information about the interface in a selective and sensitive manner.⁵⁻⁸ DPPG and DPPC lipids

are chosen as they are an integral part of the membranes. The findings suggest that the OH stretch of water at the air/DPPG/water interface decreases with the addition of propofol which has been assigned to the reorganization of the hydrogen bonding of water molecules with the OH group of propofol. In contrast, the change in the OH stretch of water is marginal on the addition of the propofol which indicates that the probability of the interaction of propofol with zwitterionic lipid is slim. This study indicates that propofol prefers to interact with the negatively charged lipid rather than the zwitterionic lipid associated with the membranes.

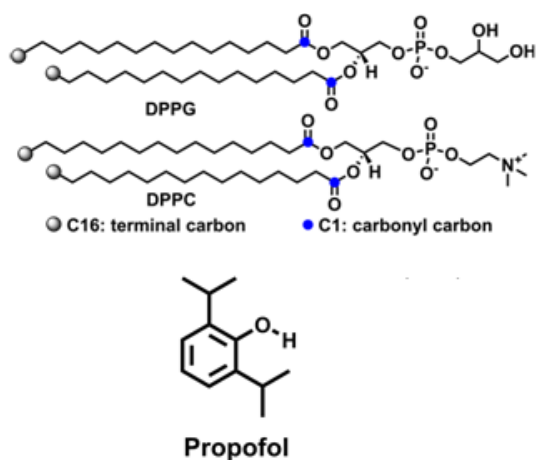


Figure 1: Structure of DPPG and DPPC lipid and the propofol molecule.

Methods and Materials

The details of the VSFG system have been described in detail elsewhere.⁸ Briefly, fundamental output from the Nd:YAG laser (EKSPLA, PL2231 series, pulse width: 25 ps, repetition rate: 50 Hz, wavelength: 1064 nm) has been used to generate the visible pulse (ω_1) of 532 nm by the frequency doubling (EKSPLA, SFGH500). A tunable IR pulse (ω_2 , tunable wavelength: 1300–4000 cm^{-1}) has been generated by an optical parameter amplifier (EKSPLA, PG-501-DFG) which has been pumped by the remaining 532 nm. ω_1 and ω_2 pulses have been overlapped spatially and temporally to generate the VSFG signal. The incident angles of ω_1 and ω_2 pulses are 58.2° and 55.6° , respectively. The

VSFG signal is detected by a photomultiplier tube (Hamamatsu, R11528) coupled with a monochromator (Princeton instruments, SP series). The VSFG signal from the z-cut quartz surface has been used to normalize the VSFG signal from the sample. All the measurements were performed at 298 ± 3 K. Anionic DPPG and zwitterionic DPPC lipids were purchased from Sigma Aldrich. Lipid solutions were prepared in chloroform and spread on the water to form the monolayer. The propofol was purchased from Sigma-Aldrich and used in the same condition. The surface pressure (π) values of the lipids monolayer-water interfaces were 35 ± 5 mN/m depicted in the liquid-compressed phase of lipids. The addition of propofol does not affect the surface pressure of the lipid monolayer significantly in the liquid-compressed phase. Milli-Q water ($18.2 \text{ M}\Omega\text{cm}$ resistivity) was used for sample preparation. The surface tension of the samples was measured using the Du Nouy ring (Kruss, Germany).

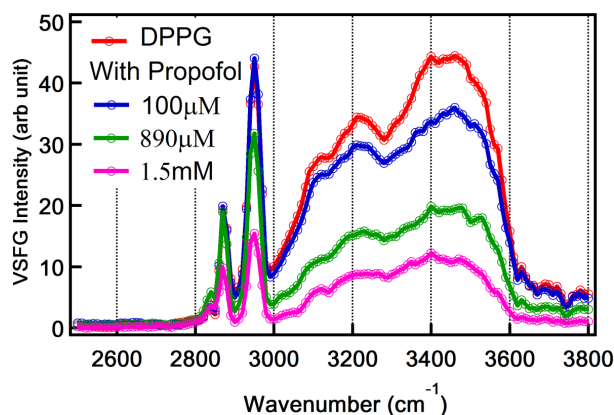


Figure 2: The SSP polarized VSFG spectra of the anionic air/DPPG/water interface in the presence of different concentrations of propofol. The surface pressure of DPPG during the measurement was 35 ± 5 mN/m ($\sim 57.2 \pm 1.8 \text{ \AA}^2/\text{molecule}$) depicting the liquid compressed (LC) phase of lipid. The addition of propofol does not affect the surface pressure of lipids within the uncertainty of the measurement.

Results and Discussion

Figure 2 shows the SSP polarized VSFG spectra of negatively charged air/DPPG/water interface in the absence and presence of the

different concentrations of propofol. The spectral feature in the range of 2800-300 cm^{-1} corresponds to the C-H stretch of the hydrocarbon chain of the DPPG lipid whereas the VSFG signal in the range of 3000-3600 cm^{-1} belongs to the OH stretch of the interfacial water in the beneath of air/DPPG/water interface. The OH signal of water at the air/DPPG/water interface is significantly higher (~ 5 times) than the air/water interface due to the fact that water at the air/DPPG/water is oriented due to the formation of the electric double layer created by the negative charge present in the head group of the DPPG lipid and counterion.⁹

With the addition of 100 μM propofol, the intensity of the OH stretch of the water at the air/DPPG/water interface decreases. With further increment of propofol, the intensity of the water at the air/water interface decreases, although, the intensity of the water at the air/DPPG/water interface in the presence of 1.5mM is still higher than the case of air/water case. The higher signal of water at the lipid interface is due to the enhanced orientation of hydrogen-bonded water due to the negative charge of the lipid. Hence, the decrease in the water signal on the addition of the DPPG could either be due to the reduction of the

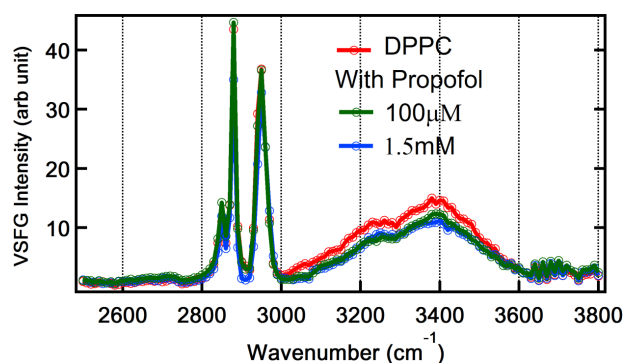


Figure 3: (a) The SSP polarized VSFG spectra of zwitterionic air/DPPC/water interface on the addition of different concentrations of dopamine. The changes in the CH_3 -ss, CH_2 -ss, and CH_3 -ss/ CH_2 -ss of the hydrocarbon chain of DPPC for the various concentrations of dopamine are depicted in (b), (c), and (d), respectively. The surface pressure of the DPPC during the measurement was 35 ± 5 mN/m ($\sim 44.5 \pm 1.2$ $\text{\AA}^2/\text{molecule}$) depicting the LC phase of the lipid. The addition of dopamine does not affect the surface pressure of lipids within the uncertainty of the measurement.

negative surface charge of the lipid or due to the rearrangement of the hydrogen bonding induced by the negative charge. Propofol molecule has no charge; hence, it is not possible to screen the net surface charge of the DPPG lipid molecule. However, the propofol molecule has the OH group which can form the hydrogen bonding of the water molecules beneath to the air/DPPG/water interface. Hence, the decrease in the water signal in the presence of the propofol could be due to the rearrangement of hydrogen bonding of water molecules with the propofol at the air/DPPG/water interface rather than the charge screening effect.

The VSFG spectrum of the C-H stretch of the hydrocarbon chain of DPPG at the air/DPPG/water interface depicts signals at 2850, and 2875 cm^{-1} along with relatively broad peaks with double peak features centered at 2950 and 2965 cm^{-1} , respectively. The spectral features at 2850 and 2875 cm^{-1} have been attributed to CH_2 -ss and CH_3 -ss of the hydrocarbon chain of DPPG lipid, whereas, broad features containing the peaks around 2950 and 2965 cm^{-1} have been assigned to its CH_3 -FR and CH_3 -as, respectively.¹⁰ The intensity of the C-H signal of lipids decreases with the addition of propofol. However, it is difficult to assign this decrease as the change in the hydrocarbon of lipid molecules as the propofol molecules also have C-H stretch which contributes to the same reason as well as the background signal of the water molecules also decreases with the addition of propofol. Nevertheless, it is apparent from the data that propofol molecules may perturb the hydrogen bonding environment near the negatively charged lipid interface.

Figure 3 shows the SSP-polarized VSFG spectra of the zwitterionic air/DDPC/water interface in the absence and presence of the different concentrations of propofol. The VSFG spectrum of the air/DPPC/water interface is in accordance with the earlier studies as the intensity of the water signal at the air/DPPC/water interface is higher than that in the air/

water interface (Figure S1c). Irrespective of the zero net charge on DPPC, it possesses a higher dipole moment (~24 Debye) due to the presence of NH_3^+ and PO_4^- . In earlier studies, it has been suggested that the high dipole moment of the DPPC orient the surface water which results in the higher VSFG signal of interfacial water at the air/DPPC/water than the air/water interface.¹¹ With the addition of propofol, the OH stretch signal of water changes marginally. Similarly, the change in the C-H stretch of the hydrocarbon change of DPPC lipid is almost unchanged with the addition of propofol. The change in the O-H stretch of water and the C-H stretch of the hydrocarbon chain of the lipid indicates that propofol does not prefer to interact with the zwitterionic lipid.

Conclusion

In order to understand the possible interaction of the anesthetic propofol with the lipid molecules associated with the membrane, the VSFG study of the negatively charged air/DPPG/water and zwitterionic air/DPPC/water interface in the absence and presence of propofol has been performed. The OH stretch of water at the air/DPPG/water interface decreases with the addition of propofol which has been assigned to

the reorganization of the hydrogen bonding of water molecules with the OH group of propofol. In contrast, the change in the OH stretch of water is marginal on the addition of the propofol which indicates that the probability of the interaction of propofol interaction with zwitterionic lipid is slim. This study indicates that propofol prefers to interact with the negatively charged lipid rather than the zwitterionic lipid associated with the membranes.

References

1. Sahinovic, M. M.; Struys, M. M. R. F.; Absalom, A. R., *Clin. Pharmacokinet.* **2018**,57 (12), 1539-1558.
2. Dinis-Oliveira, R. J., *Biomed. Res. Int.* **2018**,2018, 6852857.
3. Kopeć, W; Telenius, J; Khandelia H.,*FEBS Journal.* **2013**, 280(12, 2785-2805.
4. Högberg, C.; Lyubartsev, AP; *Biophysical Journal.* **2008**; 94(2), 525-531.
5. Gopalakrishnan, S.; Liu, D.; Allen, H. C.; Kuo, M.; Shultz, M. J., *Chem. Rev.* **2006**,106 (4), 1155-1175.
6. Shen, Y. R.; Ostroverkhov, V., *Chem. Rev.* **2006**,106 (4), 1140-1154.
7. Nihonyanagi, S.; Mondal, J. A.; Yamaguchi, S.; Tahara, T., *Annu. Rev. Phys. Chem.* **2013**,64, 579-603.
8. Biswas, B.; Sarkar, S.; Singh, P. C., *J. Phys. Chem. C* **2020**,124 (33), 18063-18069.
9. Mondal, J. A.; Nihonyanagi, S.; Yamaguchi, S.; Tahara, T., *J. Am. Chem. Soc.* **2010**,132 (31), 10656-10657.
10. Watry, M. R.; Tarbuck, T. L.; Richmond, G. L., *J. Phys. Chem. B* **2003**,107 (2), 512-518.
11. Ohto, T.; Backus, E. H. G.; Hsieh, C.-S.; Sulpizi, M.; Bonn, M.; Nagata, Y., *J. Phys. Chem. Lett.* **2015**,6 (22), 4499-4503.



Prashant Chandra Singh did Ph.D. from Indian Institute of technology Bombay. He did the postdoctoral study with Professor Arthur Suits from Wayne State University, USA and Professor Tahei Tahara from RIKEN, Japan, He joined as an assistant professor at Indian Association from the Cultivation of Science, Jadavpur, Kolkata. He is currently professor at the same institute. His research interest is to understand the structure and activity of the complex biomolecular systems using the state of art spectroscopic techniques.



Biswajit Biswas got the master degree from the Indian Institute of technology, Kharagpur. He joined Ph.D. in 2015 with Professor Prashant Chandra Singh at Indian Association from the Cultivation of Science, Jadavpur, Kolkata. He achieved PhD degree in 2021 and currently post doctorate fellow at Ohio state university, USA.

Mn-doping in Low-dimensional Perovskites for Tunable Optical Properties

Tushar Debnath*

Centre for Nanotechnology, Indian Institute of Technology Guwahati, Guwahati, Assam 781039, India

*Email:t.debnath@iitg.ac.in, debnathtushar@gmail.com

Abstract

Mn-doping into halide perovskite nanocrystals (PNCs) may lead to outstanding optical, electrical, and magnetic properties. In the last few years, extensive research efforts have been devoted to tailoring different synthesis strategies to dope Mn into PNCs, leading to exciting optoelectronic properties. In this review, we have highlighted our recent contribution to developing the field of Mn-doped PNCs. In particular, we have emphasized the Mn-doping-induced quantum confinement effect in the perovskite host via lattice rearrangement. We then summarized the unique interfacial Mn-doping into low-dimensional perovskites using oleylamine as a shuttling ligand that transports Mn from the aqueous to non-aqueous phase and finally delivers to the PNCs. Such a strategy allows us to incorporate Mn in as low as 1.2 nm layer perovskite NPLs, the smallest reported so far, with the simultaneous emergence of exceptional optical properties, e.g. giant exciton Stokes shift. A charge transfer phenomenon via transient Mn^{3+} is proposed to account for the observation of giant exciton Stokes shift. Ultrafast exciton-to-dopant energy transfer dynamics and their thickness dependence are also discussed. Finally, the development of chemically coupled, photostable Mn-doped PNCs and Ca-quinolate complex nanocomposite is discussed in the context of a stable white light emitter.

Introduction

Semiconductor nanocrystals (NCs) or, quantum dots (QDs) offer tunable optical properties that enable their multi-dimensional use in photovoltaics, optoelectronics, bioimaging, etc. which is the underlying reason for rewarding the Nobel Prize in chemistry for *the discovery and synthesis of quantum dots* in 2023. The research on QDs started in the early 80's and expanded manifold during 90's triggered by the seminal work by Bawendi et al. for the synthesis of size-controlled colloidal QDs.¹ Beyond conventional QDs, several other nanocrystalline materials emerge, e.g. perovskite nanocrystals, graphene, two-dimensional chalcogenides, carbon dots, etc. which are also contributing to the growth of this field.

In particular, lead-halide perovskite nanocrystals (PNCs) are gaining increasing attention in contemporary research due to their

unique physical properties and novel application possibilities like single-photon emitters for quantum technologies.² By controlling the size and composition, one can easily tune the optical properties of PNCs in the entire visible region.^{3,4} In addition, the introduction of dopant impurities e.g., Mn^{2+} also enables tunable optical, electrical, and magnetic properties of PNCs.⁵ The introduction of Mn^{2+} ions in PNCs leads to strong exciton-dopant interaction, enabling exciton-to-dopant energy and charge transfer processes, and is responsible for promising performance in light-emitting-diodes (LEDs) and solar cells.⁶⁻⁹ The transfer of exciton energy to the Mn dopant is the underlying reason for the observation of orange emission due to the spin-forbidden ${}^4T_1 - {}^6A_1$ transition (Mn^{2+} d-d transition). Researchers are often engaged with the improvement of the Mn-emission via the energy transfer process, whereas the influence of doping on the lattice arrangement and the subsequent effect on

the exciton remains elusive and needs to be understood from a fundamental point of view.

From the synthesis perspective, most reports use a direct colloidal synthesis approach to produce high-quality Mn-doped lead-halide PNCs, where all the precursors are taken into one pot and Cs-precursor is injected at high temperature (hot-injection method).^{5,10} However, in this approach the Mn-precursor (e.g. MnCl_2) faces strong competition from the Pb-precursor (PbCl_2) due to bond energy mismatch, leading to less effective Mn-doping. In contrast, the post-synthetic approach has emerged as a versatile method for the chemical transformation of PNCs, both in terms of phase structure composition and morphology.^{4, 11, 12} The post-synthetic approach has been used for doping in PNCs on a few occasions, however, is often limited to single phase and/or miscible bi-phase where the presence of miscible polar solvent (e.g. DMF, acetone, HBr) sacrifices quality and stability of the product.

In this review, we first highlight the influence of Mn-dopant on the excitons in CsPbBr_3 perovskite nanocubes via lattice arrangement. Our results suggest incorporation of Mn-dopant

leads to quantum confinement of the host perovskite excitons. We then highlight some of our recent developments of post-synthetic Mn-doping in low-dimensional perovskites via water-hexane interfacial strategy. This unique approach allows us to incorporate Mn in as small as 1.2 nm perovskite layer, which is the smallest Mn-doped perovskite system reported and leads to the emergence of distinctive optical properties. The exciton-to-Mn energy transfer dynamics also has been discussed via ultrafast spectroscopy which proceeds in 100's of ps timescale. Finally, we show that Mn-doped PNC-based nanocomposite may result in the development of a photostable white-light-emitter with properties close to the bright mid-day sunlight.

Mn-doping induced exciton quantum confinement

We developed a simple one-pot approach¹³ for synthesizing Mn-doped CsPbCl_3 NCs, where along with PbCl_2 and MnCl_2 precursors, Cs-precursors were also added in the reaction vessel, unlike other typical recipes where Cs-precursor is injected at high temperature. All the precursors, together with ligands and solvent were then subjected to tip-sonication for ~15

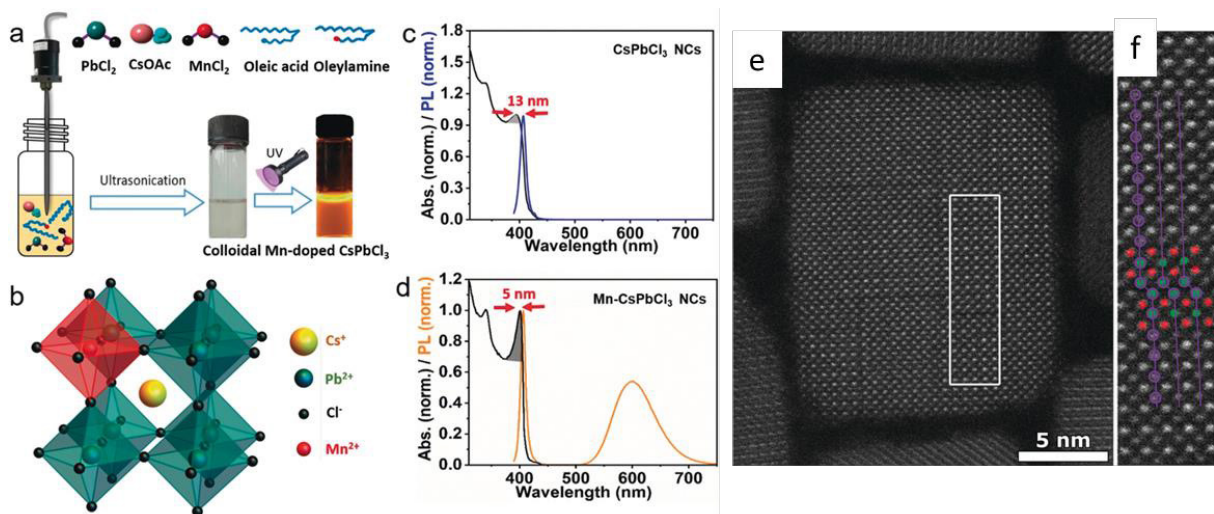


Figure 1. a) Schematic of the synthesis method for the one-pot Mn-doped CsPbCl_3 NCs via tip-sonication. The photographs of the obtained solution under daylight and UV light are also shown. b) Crystal structure of Mn-doped CsPbCl_3 . Optical absorption and PL spectra of c) CsPbCl_3 and d) Mn-doped CsPbCl_3 NCs. e, f) Atomically resolved HAADF-STEM image of Mn-doped CsPbCl_3 NCs, clearly showing the R.P. defect planes (red: Pb/Mn-Cl, green: Cs). The lattices are shifted half a unit cell at the grain boundary.¹³

mins, resulting formation of Mn-doped CsPbCl₃ NCs, which were then centrifuged to purify the product (Fig. 1a, 1b). The optical absorption and photoluminescence (PL) spectra of undoped and Mn-doped CsPbCl₃ NCs are shown in Fig. 1c and 1d, respectively. While undoped CsPbCl₃ NCs have typical exciton absorption at ~390 nm and PL emission at ~400 nm, the Mn-doped CsPbCl₃ NCs show an additional broad PL emission at ~600 nm, corresponding to the orange emission. The appearance of orange emission due to the Mn²⁺ d-d transition confirms the successful incorporation of Mn²⁺ into the CsPbCl₃ lattice.

In addition to the Mn-related PL at 600 nm, there are two more distinct differences present in the optical spectra of the undoped and doped NCs in Fig. 1c, 1d. One can clearly see the exciton absorption becomes more pronounced upon Mn-doping (grey shaded areas), along with a significant reduction in the exciton Stokes shift (13 nm vs. 5 nm). Importantly, we observed a continuous blue shift of the absorption and PL spectra with increasing Mn-amount. All these observations suggest quantum confinement of the excitons upon Mn incorporation. As Mn²⁺ is supposed to replace Pb²⁺ during doping, one should expect it would also alter the lattice rearrangement since the size of both atoms differs. To this end, we performed atomically resolved high-angle annular dark-field scanning transmission electron microscopy (HAADF-STEM). As shown in Fig. 1e, f, one can evidently see multiple atomic dislocations within a single nanocrystal. Further, these defects were identified as Ruddlesden-Popper (R.P.) defects, where the (Pb/Mn)-Cl atomic planes are shifted by half a unit cell at the border of the defects. Similar R.P. defects were also observed in pure as well as mixed halide perovskites.^{14, 15} The individual domains separated by these R.P. defects can confine charge carriers, leading to quantum confinement of excitons upon Mn-doping, as evident from the optical measurements. The quantum confinement of excitons in the subdomains within a single NC may result in enhanced exciton oscillator strength that possibly

contributes to the observation of pronounced exciton resonance in Fig. 1d.

Mn-doping at the water-hexane interface using a shuttling ligand

While the previously described one-pot strategy is quite appealing for Mn-doped PNC synthesis, one of the limitations is the limited solubility of Mn-salt in organic solvent, leading to less efficient Mn-loading. We find Mn-halide salt has maximum solubility in an aqueous medium, and therefore, it would be great if one can transport Mn-salt from aqueous to a non-aqueous phase where perovskite resides, for doping. Although perovskites are extremely unstable in the presence of water and moisture, recent reports on the chemical transformation of PNCs via a water-triggered strategy¹⁶⁻¹⁸ motivated us to develop a unique strategy for Mn-doping at the water-hexane interface. In this approach,¹⁹ we first prepared CsPbBr₃ nanoplatelets (NPLs) in hexane following a previous recipe, on which different amount of MnBr₂ dissolved aqueous solution was added in 40:1 ratio at room temperature and stirred for 1 h (Fig. 2a). The blue PL of the CsPbBr₃NPLs was then turned into pinkish orange under UV-light, indicating formation of Mn-doped CsPbBr₃NPLs. The HAADF-STEM images in Fig. 2b - e clearly show the formation of undoped and Mn-doped NPLs, where no obvious change in the morphology was observed upon Mn incorporation. Fig. 2f depicts the optical absorption and PL spectra of undoped and Mn-doped CsPbBr₃NPLs. The undoped NPLs show strong exciton resonance at 456 nm and a single PL emission at 461 nm, corresponding to the 5 monolayer (ML) thickness of the NPLs. As the MnBr₂ concentration increases in water (from 2M to 7M) during the interfacial synthesis, a new broad PL emission in 550 - 700 nm is apparent due to Mn-related d-d transition, implying successful doping. The intensity of the Mn-PL at 618 nm increases with increasing Mn-amount in water, though the exciton absorption and PL peaks remain unchanged. The success of the doping is also confirmed via other techniques,

such as electron paramagnetic resonance (EPR) spectroscopy, and Inductively Coupled Plasma-Optical Emission-Spectrometry (ICP-OES).

To understand the doping mechanism at the water-hexane interface, and more importantly, how the Mn-salt is transported from the aqueous to non-aqueous phase, we carefully performed a set of controlled measurements using a two-step synthesis (TPS) strategy. As there are different ligands, e.g. oleic acid (OA), and oleylamine (OLA) present, we believe they might have played a major role in the Mn-salt transportation. In an ideal TPS strategy, the first step is to obtain Mn-salt in the hexane phase from water using only one type of ligand to understand the role

of each ligand individually. In the second step, this Mn-enriched hexane solution is added to NPIs to achieve the doping. Generally, Mn-salt saturated aqueous solution is added to hexane solution containing only one type of ligand and vortexed for 1 min. Then the upper phase is carefully taken out, primarily containing ligands in hexane, and added to NPIs solution. PL under UV-light as well as PL spectra of the corresponding solutions for different precursors (e.g., individual Mn-salt, ligand OLA or, OA) are shown in Fig. 2g. When OLA is used as a ligand and MnX_2 ($X=Cl, Br$) is used in the first step, Mn-doping is successful and can be evident from the appearance of pinkish orange color under

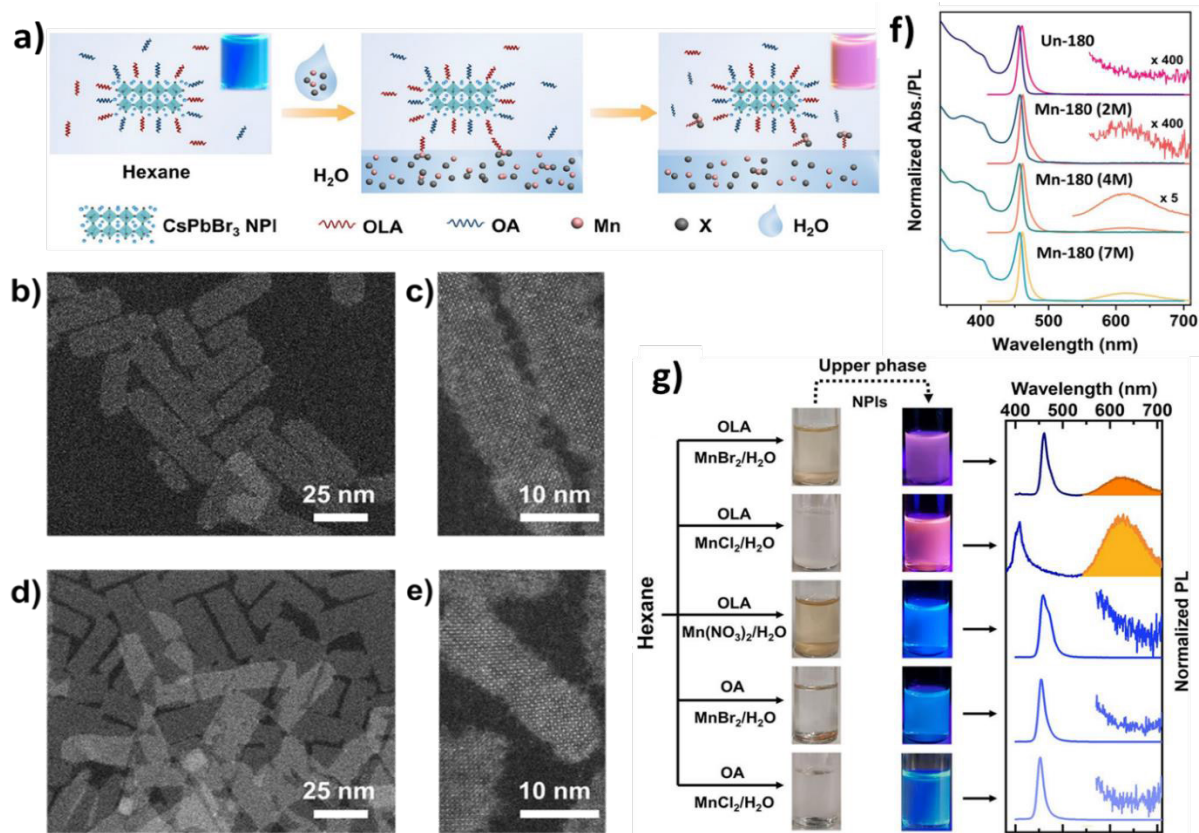


Figure 2. a) Schematic presentation of MnX_2 doping at the water-hexane interface using OLA shuttle ligand. The photographs of undoped and Mn-doped $CsPbBr_3$ NPIs under UV light are shown in the inset. b, d) HAADF-STEM images of undoped and Mn-doped $CsPbBr_3$ NPIs, and the corresponding high-resolution images in c, e), respectively. f) UV-vis absorption and PL spectra of undoped and Mn-doped NPIs, with various $MnBr_2$ concentrations (2M to 7M) in the water. (Inset) expanded PL spectra in the 550 – 700 nm region. g) Two-step Mn-doping strategy at the water-hexane interface to confirm the shuttling role of OLA. At first, a mixture of appropriate ligands in hexane and Mn-salt in water is shown under daylight. The upper phase is then added to $CsPbBr_3$ NPIs, and the resulting solutions under UV light are shown. The corresponding PL spectra are also shown on the right.¹⁹

UV-light as well as broad Mn-PL, peaking at ~ 624 nm (Fig. 2g). However, the reaction fails when OA is used in the first step instead of OLA, for both MnBr_2 and MnCl_2 , as the solution still remains blue under UV-light and no broad PL emission is observed around 600 nm. This observation clearly suggests the critical role of OLA in the transportation of Mn-halide salt from the aqueous to non-aqueous phase, where OLA acts as a shuttling ligand. Here, it is important to note that OLA transports Mn-halide as a whole from the aqueous to non-aqueous phase where not only Mn^{2+} is incorporated but also halide ion exchange takes place. This is evident from the OLA/ MnCl_2 case, where the exciton PL peak is also blue shift to 409 nm from 461 nm due to the formation of Mn-doped $\text{CsPb}(\text{Br}/\text{Cl})_3\text{NPLs}$. Importantly, the Mn-PL emission becomes much more intense due to an efficient exciton-to-dopant energy transfer phenomenon in the Cl-Br mixed halide NPLs.

When we performed the reaction using $\text{Mn}(\text{NO}_3)_2$ in the presence of OLA, the upper phase turned brownish, indicating Mn^{2+} is transported to hexane from water. However, when the upper phase comprising Mn^{2+} is added to the NPLs solution, doping was unsuccessful, as no Mn-PL was observed and the solution remain blue under UV light. Here although $\text{Mn}(\text{NO}_3)_2$ is transported to the hexane phase, it cannot achieve doping, indicating a critical role of halides, without which the doping failed. A similar result was also observed with Mn-acetate salt.²⁰ We propose during entering from water to hexane, Mn^{2+} remains in coordination with the anions (X^- , NO_3^{2-}) and OLA. In the presence of halides, Mn^{2+} form a high-spin complex with an effective ionic radius of 83 pm, while for the NO_3^{2-} it form a low-spin complex, having a less effective ionic radius (67 pm). Such a decrease in ionic radius reflects a drop in the octahedral factor for the crystal structure containing Mn^{2+} and Br from 0.42 to 0.34, falling out of the possible radius ratio (0.41 to 0.9). As a result, Mn^{2+} from $\text{Mn}(\text{NO}_3)_2$ cannot sufficiently stabilize the crystal

structure and thus is unlikely to replace Pb^{2+} to form Mn-doped $\text{CsPbBr}_3\text{NPLs}$. Overall, the beautiful interfacial strategy not only reveals the shuttling role of OLA but also the critical role of halides in maintaining a proper octahedral factor for Mn^{2+} doping in perovskites.

Charge and energy transfer processes in Mn-doped $\text{CsPbX}_3\text{NPLs}$

The newly developed water-hexane interfacial strategy allows us to prepare thickness-dependent Mn-doping in $\text{CsPbX}_3\text{NPLs}$, down to 2 ML thickness, corresponding to as small as a 1.2 nm layer.²⁰ Fig. 3a compares the optical absorption and PL spectra of 2 – 5 ML undoped $\text{CsPbBr}_3\text{NPLs}$, prepared at room temperature. Fig. 3b compares the optical spectra of corresponding Mn-incorporated $\text{CsPbCl}_3\text{NPLs}$, showing clear Mn-PL between 550 – 700 nm, where MnCl_2 was used during the water-hexane interfacial doping. The 2 ML undoped NPLs shows a strong exciton resonance at ~ 425 nm and the corresponding PL at ~ 428 nm (Fig. 3a). The 2 ML Mn-doped NPLs shows an even stronger resonance at ~ 343 nm (Fig. 3b), which is strongly blue-shifted than the undoped counter-part due to Cl-exchange, as the doping was performed using MnCl_2 aqueous solution. The sharp resonance in the absorption spectrum is attributed to strong quantum confinement along the 1.2 nm thickness direction, which is much smaller than the exciton Bohr radius of CsPbBr_3 . With increasing thickness of the NPLs, the absorption spectra become broad and both absorption and PL red shift in the undoped NPLs (Fig. 3a). In contrast, although the exciton absorption becomes broad and red-shifted with increasing thickness in the Mn-doped NPLs, the PL stays nearly unaltered (Fig. 3b). In effect, the exciton Stokes shift becomes much higher in Mn-doped NPLs than the corresponding undoped NPLs. In Fig. 3c, we have shown the comparison of exciton Stokes shift of the undoped and Mn-doped NPLs, as a function of thickness, while Fig. 3d depicts the corresponding exciton PL peak positions. One can evidently see that the exciton Stokes

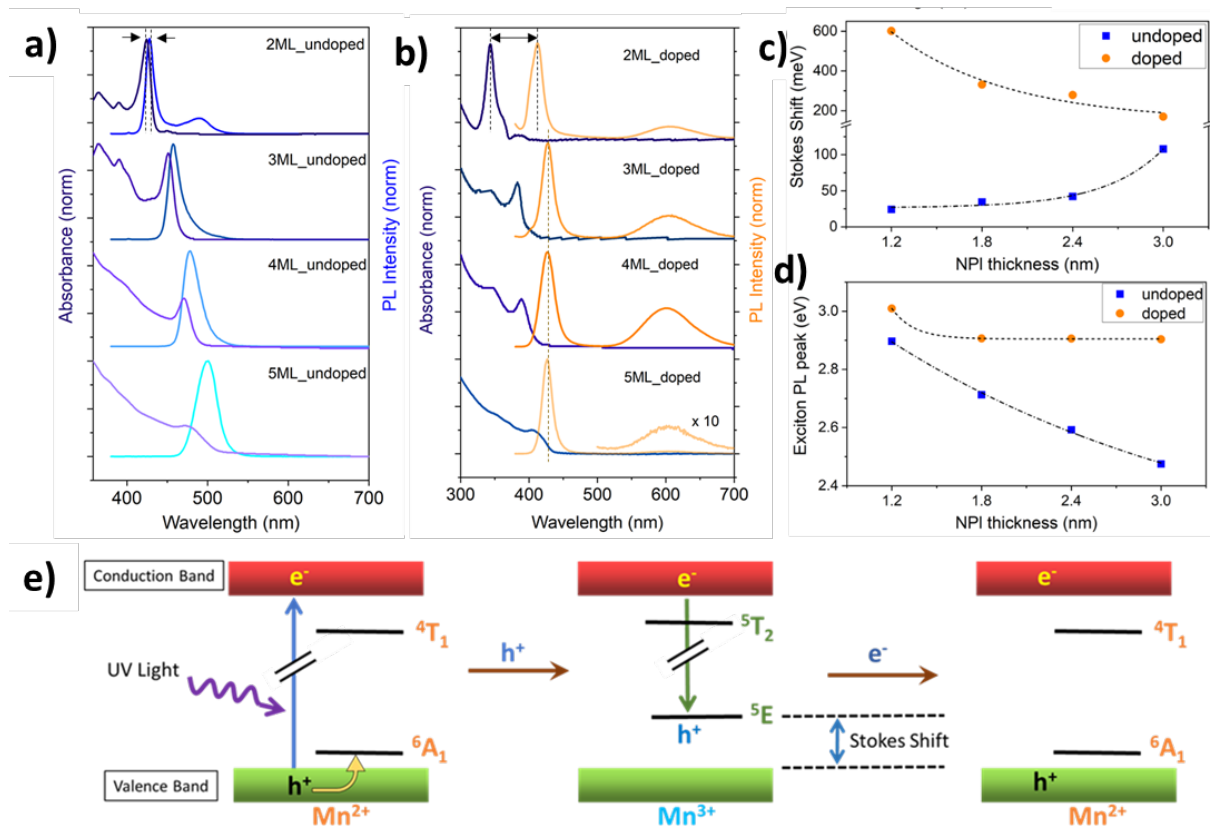


Figure 3. UV-vis absorption and PL spectra of 2 – 5 ML a) CsPbBr₃ NPIs and b) Mn-doped CsPbCl₃ NPIs. c) Exciton Stokes shift and d) Exciton PL peak position of the undoped and doped NPIs as a function of the NPI thickness. e) Proposed model for the highly enhanced Stokes shift in the Mn-doped NPIs via formation of the transient Mn³⁺.²⁰

shift increases drastically to ~600 meV upon Mn-doping in 2 ML (i.e. 1.2 nm thick) NPIs in comparison to the 2 ML undoped NPIs where only ~25 meV Stokes shift was observed (Fig. 3c). With increasing the thickness, the exciton Stokes shift decreases in the doped NPIs, while reverse phenomena were observed in the undoped NPIs. Importantly, from Fig. 3d it appears the exciton PL peak is thickness independent in the Mn-doped NPIs, in contrast to the undoped NPIs where strong thickness dependence was observed. In the Mn-doped NPIs, the exciton PL always appears at 427 nm, except at 2 ML thickness where slightly blue-shifted PL (~412 nm) was observed.

To explain the origin of the highly enhanced exciton Stokes shift in the Mn-doped CsPbCl₃ NPIs, we proposed the following model, shown in Fig. 3e. Upon photoexcitation, the electron-hole pair is generated in the Mn-doped CsPbCl₃ NPIs,

and subsequently in an ultrafast timescale, the hole may transfer to Mn²⁺, leading to the formation of transient Mn³⁺, which is now ready to accept an electron from the conduction band of the host NPIs. The recombination of this electron with the hole in the 5E state of Mn³⁺ gives the characteristic PL, which is highly Stokes shifted. Earlier charge transfer phenomenon and detection of transient Mn³⁺ has been observed both theoretically and experimentally in semiconductor NCs, including perovskite materials.^{7-9, 21, 22} Here, the PL peak position in Mn-doped NPIs is strongly dependent on the host conduction band and the 5E state of the Mn³⁺. The energetic position of the atomic-like 5T₂ – 5E states of the Mn³⁺ are generally independent of the host lattice, similar to the 4T₁ – 6A₁ states in the Mn²⁺.²³ Thus, upon decreasing the thickness, the bandgap of the Mn-doped NPIs increases, but the energetic position of the 5T₂ – 5E

remains nearly unchanged. Consequently, the PL emission of the Mn-doped NPLs remains nearly unaltered with the thickness variation as shown in Fig. 3d.

The energy transfer (ET) dynamics from the host NPLs to the Mn-dopant were also investigated by ultrafast transient absorption (TA) spectroscopy.¹⁹ Fig. 4a and 4d depict TA spectra at a few different time delays of the undoped and Mn-doped CsPbBr₃ NPLs, corresponding to 4 ML thickness (the pristine NPLs were prepared at 100 °C). Fig. 4c shows the corresponding TA time traces at the bleaching maxima. While the early time TA traces look very similar, the TA kinetics becomes much faster at a longer timescale in the Mn-doped CsPbBr₃ NPLs. The major difference between the undoped and Mn-doped NPLs is that the Mn-doped NPLs has an additional deactivation channel via ET to the Mn-dopant, leading to the Mn-PL (Fig. 4d). Therefore, the faster recombination kinetics at the longer time delays is assumed to be due to

the exciton-to-dopant ET process. To quantify the ET timescale, we subtracted the two transients (after normalizing at a longer time delay of ~1 ns) (inset in Fig. 2c). The exponential fitted time constant reveals the ET timescale of ~168 ps for this sample. The ET timescale of the Mn-180 NPLs, which corresponds to 5 ML thickness, is also estimated similarly to show an even slower ET timescale (~311 ps). The ET efficiency of these two samples (4 ML and 5 ML doped) was estimated to be ~91% and ~73%, respectively.

Application of Mn-doped Perovskite NCs as a Photostable White-light-emitter

In the above sections, we have summarized the optical tunability of several Mn-doped low-dimensional perovskites which were obtained via different synthesis approaches. In this section, we will highlight how we have utilized such Mn-doped perovskites for their possible application as white-light emitters. We chose orange emitting Mn-doped CsPbCl₃ NCs (HPNCs) and cyan

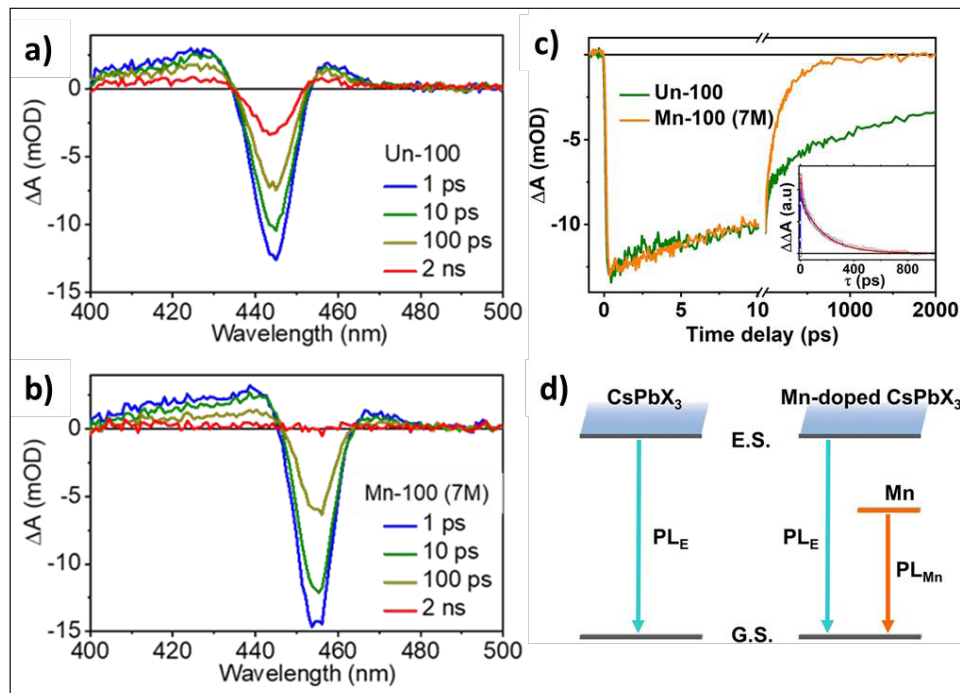


Figure 4. Transient absorption spectra at different time delays of the a) undoped and b) Mn-doped CsPbBr₃ NPLs. c) Corresponding kinetics at the bleaching maxima. (Inset) the difference between the two kinetics ($\Delta\Delta A$), after normalizing at a longer time delay (~ns). The solid red line is the exponential fit. d) Schematic within the exciton picture, showing exciton PL in the undoped and both exciton and Mn-PL in the Mn-doped NPLs.¹⁹

emitting calcium quinolate (CaQ_2) complex to fabricate a nanocomposite (Fig. 5a).²⁴ The nanocomposite was found to be photostable as compared to the Mn-doped CsPbCl_3 HPNCs due to surface chloride-calcium interaction. Fig. 5b and 5c show the TEM and HRTEM images of Mn-doped CsPbCl_3 HPNCs, revealing the cubic morphology of the nanocrystals. The TEM and HRTEM images of the CaQ_2 -HPNCs nanocomposite are shown in Fig. 5d, 5e, indicating the unchanged size and shape of the nanocrystals. The inverse fast Fourier transform (I-FFT) pattern also shows a similar lattice spacing of 0.4 nm, corresponding to the (110)

plane (Fig. 5c and 5e). As shown in Fig. 5f, the PL spectrum of the Mn-doped CsPbCl_3 HPNCs (thin film) shows excitonic PL at 405 nm and Mn-related broad PL at 585 nm, corresponding to color chromaticity coordinate of (0.47, 0.42) (Fig. 5g). This results in orange emission under UV-light (both in solution and thin film), see Fig. 5h. The PL spectrum of the CaQ_2 -HPNCs nanocomposite (Fig. 5f) shows triple emission, peaking at 405 nm, 464 nm and 585 nm, where the emission at 464 nm (cyan) comes from the CaQ_2 complex. In effect, the synchronized contribution of the triple emission from the nanocomposite leads to the emergence of white

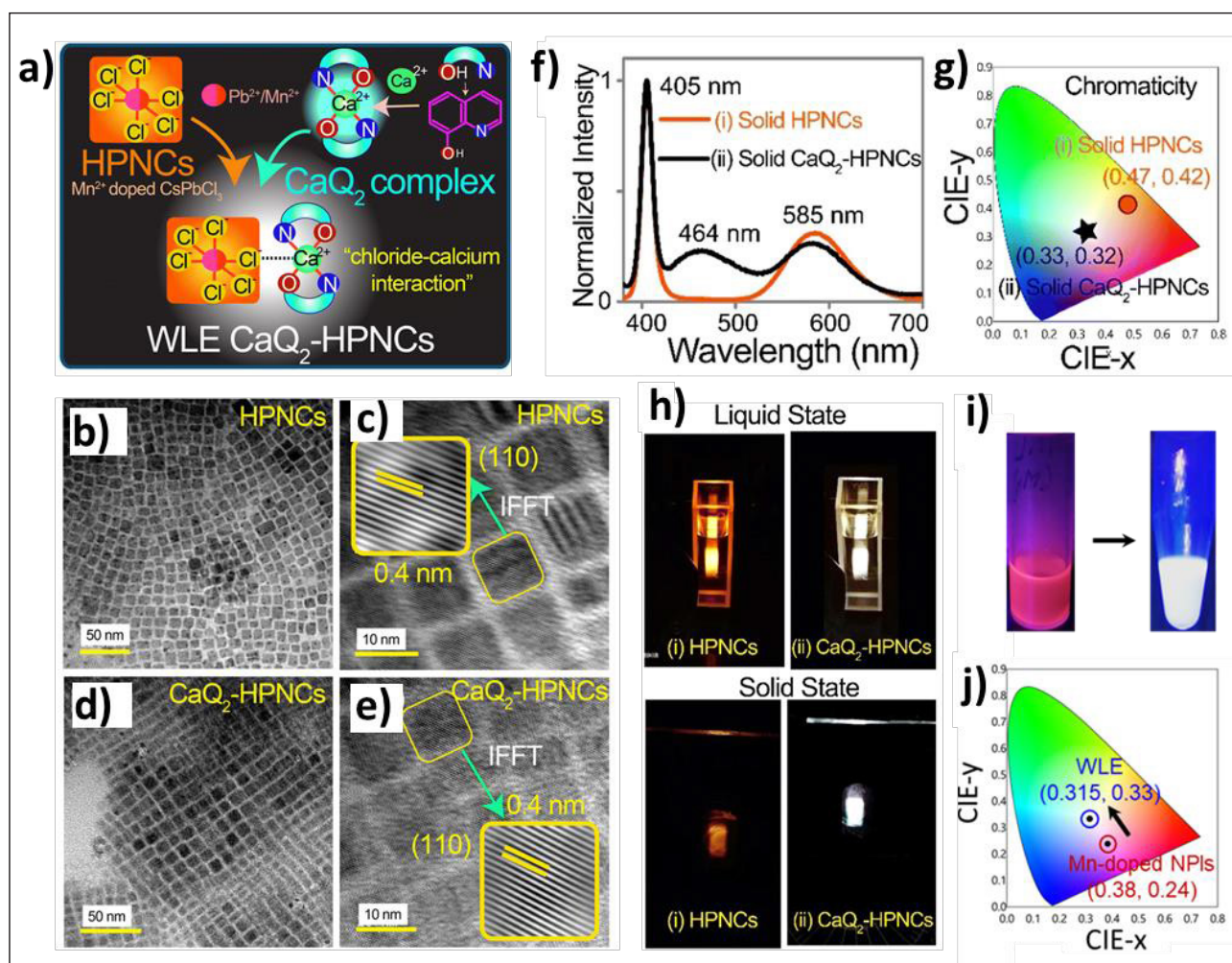


Figure 5. a) Schematic illustration of the formation of CaQ_2 -HPNCs nanocomposite. b-e) TEM and HRTEM images of Mn-doped CsPbCl_3 HPNCs and Mn-doped CsPbCl_3 HPNCs/ CaQ_2 nanocomposite. Inset in c) and e) shows I-FFT analysis of the corresponding samples. f) PL spectra, g) color chromaticity coordinates, and h) digital photographs under UV light of the solid (thin film) and liquid (for photographs) HPNCs and CaQ_2 -HPNCs. i) Digital photographs under UV-light and j) color chromaticity coordinate of the Mn-doped CsPbCl_3 NPIs and the corresponding white light emitter.^{20, 24}

light emission (in both solution and solid-state, Fig. 5h). The corresponding color chromaticity coordinate of the photostablenanocomposite was found to be (0.33, 0.32). Importantly, we estimated the color rendering index (CRI) of 80, correlated color temperature (CCT) of 5483 K, and quantum yield of 54.1% for the nanocomposite, all directing properties very close to the bright mid-day sunlight. We have also fabricated a white light emitter using the giant exciton Stokes shifted Mn-doped CsPbCl₃NPIs by making a nanocomposite with CsPbBr₃ NCs, which shows color chromaticity coordinate of (0.315, 0.33) (Fig. 5i, 5j), and is indicative of the bright future of such doped NPIs.²⁰

Conclusion

To summarize, we have discussed incorporation of Mn-dopant in perovskite NCs may lead to excitonquantum confinement of the host NCs by introducing lattice rearrangement via R.P. defects. We then discussed a unique ligand shuttling approach for Mn-doping in low-dimensional perovskites at the water-hexane interface. Such a unique strategy allows us to incorporate Mn in as small as 1.2 nm thick NPIs, the smallest reported so far. This opens distinctive optical properties e.g., giant exciton Stokes shift of 600 meV as compared to only 25 meV in the corresponding undopedNPIs due to charge transfer via the transient Mn³⁺ intermediate, which may be found important avenue in light emitting devices, e.g., as white light emitter. We further discussed the exciton-to-Mndopant energy transfer dynamics and their thickness dependence in the Mn-doped CsPbBr₃NPIs. Finally, we prepared a photostable white light emitter by chemically coupling orange-emitting Mn-doped CsPbBr₃ NCs and cyan-emitting CaQ₂ complex. We believe the review composed of a unique interfacial Mn-doping strategy, and the physical and optoelectronic insights of several Mn-doped low-dimensional perovskites maystimulate advanced optoelectronic applications.

Acknowledgements

T.D. acknowledges the Department of Science & Technology (DST) and the Science and Engineering Research Board (SERB) for the Ramanujan Fellowship Award (RJF/2021/000125).

Author biography

Dr. Debnath is presently working as a principle investigator at the Centre for Nanotechnology, IIT Guwahati, India. He obtained his Ph.D. in Chemistry in 2016 from BARC, Mumbai, India. Subsequently, he moved to NTU, Singapore (2016 - 2018) as a postdoctoral fellow followed by LMU, Munich, Germany (2018 - 2022). He was optical spectroscopy group leader at the department of physics, LMU from 2019 - 2022, and then he started his independent research group at IIT Guwahati, India (2022 - present). Dr. Debnath is an expert in the field of ultrafast spectroscopy. His research interest focuses on the investigation of the fundamental photophysics of semiconductor nanocrystal materials, primarily for energy-related applications. Dr. Debnath is the recipient of several national as well as international awards, including the Alexander von Humboldt fellowship, Germany (2018), best young scientist publication award, CeNS, LMU (2020), and the Ramanujan fellowship, India (2022).

References

1. Murray, C. B.; Norris, D. J.; Bawendi, M. G., *J Am Chem Soc* **1993**, *115* (19), 8706-8715.
2. Dey, A.; Ye, J.; De, A.; Debroye, E.; Ha, S. K.; Bladt, E.; Kshirsagar, A. S.; Wang, Z.; Yin, J.; Wang, Y. et. al. *ACS Nano* **2021**, *15* (7), 10775-10981.
3. Protesescu, L.; Yakunin, S.; Bodnarchuk, M. I.; Krieg, F.; Caputo, R.; Hendon, C. H.; Yang, R. X.; Walsh, A.; Kovalenko, M. V., *Nano Lett* **2015**, *15* (6), 3692-3696.
4. Akkerman, Q. A.; D'Innocenzo, V.; Accornero, S.; Scarpellini, A.; Petrozza, A.; Prato, M.; Manna, L., *J Am Chem Soc* **2015**, *137* (32), 10276-10281.
5. Guria, A. K.; Dutta, S. K.; Das Adhikari, S.; Pradhan, N., *Acs Energy Lett* **2017**, *2* (5), 1014-1021.
6. Parobek, D.; Roman, B. J.; Dong, Y. T.; Jin, H.; Lee, E.; Sheldon, M.; Son, D. H., *Nano Lett* **2016**, *16* (12), 7376-7380.
7. Pinchetti, V.; Anand, A.; Akkerman, Q. A.; Sciacca, D.; Lorenzon, M.; Meinardi, F.; Fanciulli, M.; Manna, L.; Brovelli, S., *T Acs Energy Lett* **2019**, *4* (1), 85-93.

8. Justice Babu, K.; Kaur, G.; Shukla, A.; Kaur, A.; Goswami, T.; Ghorai, N.; Ghosh, H. N., *The Journal of Physical Chemistry Letters* **2021**,12 (1), 302-309.
9. Ricciarelli, D.; Meggiolaro, D.; Belanzoni, P.; Alothman, A. A.; Mosconi, E.; De Angelis, F., *Acs Energy Lett* **2021**,6 (5), 1869-1878.
10. Parobek, D.; Dong, Y.; Qiao, T.; Son, D. H., *Chem Mater* **2018**,30 (9), 2939-2944.
11. Mir, W. J.; Jagadeeswararao, M.; Das, S.; Nag, A., *Acs Energy Lett* **2017**,2 (3), 537-543.
12. Mir, W. J.; Mahor, Y.; Lohar, A.; Jagadeeswararao, M.; Das, S.; Mahamuni, S.; Nag, A., *Chem Mater* **2018**,30 (22), 8170-8178.
13. Paul, S.; Bladt, E.; Richter, A. F.; Doblinger, M.; Tong, Y.; Huang, H.; Dey, A.; Bals, S.; Debnath, T.; Polavarapu, L.; Feldmann, J., *Angew Chem Int Ed Engl* **2020**,59 (17), 6794-6799.
14. Akkerman, Q. A.; Bladt, E.; Petralanda, U.; Dang, Z.; Sartori, E.; Baranov, D.; Abdelhady, A. L.; Infante, I.; Bals, S.; Manna, L., *Chem Mater* **2019**,31 (6), 2182-2190.
15. Thind, A. S.; Luo, G.; Hachtel, J. A.; Morrell, M. V.; Cho, S. B.; Borisevich, A. Y.; Idrobo, J.-C.; Xing, Y.; Mishra, R., *Advanced Materials* **2019**,31 (4), 1805047.
16. Das, A.; Debnath, T., *Chemistry – A European Journal* **2023**,29 (5), e202202475.
17. Wu, L.; Hu, H.; Xu, Y.; Jiang, S.; Chen, M.; Zhong, Q.; Yang, D.; Liu, Q.; Zhao, Y.; Sun, B.; Zhang, Q.; Yin, Y., *Nano Lett* **2017**,17 (9), 5799-5804.
18. Yang, D.; Li, P.; Zou, Y.; Cao, M.; Hu, H.; Zhong, Q.; Hu, J.; Sun, B.; Duhm, S.; Xu, Y.; Zhang, Q., *Chem Mater* **2019**,31 (5), 1575-1583.
19. Wu, L.; Wang, Y.; Kurashvili, M.; Dey, A.; Cao, M.; Döblinger, M.; Zhang, Q.; Feldmann, J.; Huang, H.; Debnath, T., *Angewandte Chemie International Edition* **2022**,61 (15), e202115852.
20. Das, A.; Debnath, T., *The Journal of Physical Chemistry Letters* **2023**,14 (25), 5940-5948.
21. Debnath, T.; Maity, P.; Maiti, S.; Ghosh, H. N., *Journal of Physical Chemistry Letters* **2014**,5 (16), 2836-2842.
22. Debnath, T.; Ghosh, H. N., *J Phys Chem C* **2019**,123 (17), 10703-10719.
23. Hazarika, A.; Layek, A.; De, S.; Nag, A.; Debnath, S.; Mahadevan, P.; Chowdhury, A.; Sarma, D. D., *Physical Review Letters* **2013**,110 (26), 267401.
24. Manna, M.; Debnath, T.; Bhandari, S., *Chemical Communications* **2023**.



Dr. Debnath is presently working as a principle investigator at the Centre for Nanotechnology, IIT Guwahati, India. He obtained his Ph.D. in Chemistry in 2016 from BARC, Mumbai, India. Subsequently, he moved to NTU, Singapore (2016 - 2018) as a postdoctoral fellow followed by LMU, Munich, Germany (2018 - 2022). He was optical spectroscopy group leader at the department of physics, LMU from 2019 - 2022, and then he started his independent research group at IIT Guwahati, India (2022 - present). Dr. Debnath is an expert in the field of ultrafast spectroscopy. His research interest focuses on the investigation of the fundamental photophysics of semiconductor nanocrystal materials, primarily for energy-related applications. Dr. Debnath is the recipient of several national as well as international awards, including the Alexander von Humboldt fellowship, Germany (2018), and the Ramanujan fellowship, India (2022).

Understanding the Resonance Energy Transfer between Fluorescent Bimetallic Nanoparticles and Organic Dye molecules

AmitAkhuli,^{ab} Aditi Mahanty,^{ab} Sahadev Barik^{a,b}, Amita Mahapatra^{a,b} Debabrata Chakraborty,^{ab} and Moloy Sarkar^{ab*}

^aSchool of Chemical Sciences, National Institute of Science Education and Research (NISER), An OCC of Homi Bhabha National Institute, Jatni, Khurda, Bhubaneswar 752050, Odisha, India.

^bCentre for Interdisciplinary Sciences (CIS), NISER, Jatni, Khurda, Bhubaneswar 752050, Odisha, India.

*E-mail: msarkar@niser.ac.in

Abstract

With an aim to understand the interaction between the inorganic and organic constituents in inorganic-organic hybrid nanomaterials, we have engineered a nanocomposite system, composed of inorganic fluorescent bimetallic nanoparticles (F-AgAu) and organic dye (rhodamin B isothiocyanate, RBITC) which is different from prior hybrid systems that are incorporated by electrostatically driven self-assembly of fluorescent inorganic semiconductor quantum dots with organic dye/dye-aggregates. Before delving into the photo-physics and inter particle interaction in this inorganic-organic nanohybrid, we have synthesized F-AgAu using established protocols and characterized it through conventional methods. Steady-state and time-resolved fluorescence measurements reveal the efficient energy transfer (92%) from F-AgAu to RBITC, as demonstrated by the quenching of F-AgAu fluorescence and the simultaneous increase in RBITC fluorescence features upon excitation. Interestingly, zeta potential measurements have revealed that the interaction between F-AgAu and RBITC in the hybrid system does not follow electrostatic interaction as both components possess positive surface charges. However, the interaction of the free amine of glutathione in F-AgAu with the electrophilic carbon of the isothiocyanate group forming a stable nano-assembly, and hydrogen bonding interactions between the carboxylic group of both RBITC and the capping ligand of F-AgAu helps in overcoming the positive-positive repulsion, and facilitating efficient FRET communication. The findings of this study are expected to be helpful in designing efficient nanoscale light-harvesting devices.

Introduction

In recent years, luminescent Inorganic-organic nanohybrids are continued to be a subject of intense research, with ongoing efforts to optimize their synthesis methods and explore new applications across various scientific and technological domains.¹⁻⁸ Typically, these hybrid nanostructures are created by incorporating colloidal nanomaterials and organic dye/ organic dye aggregates, wherein the nanomaterials serve as donors for electronic excitation energy or electron transfer, and the dye/dye aggregates act as acceptors. It is known that the majority of excited state energy transfers are mediated

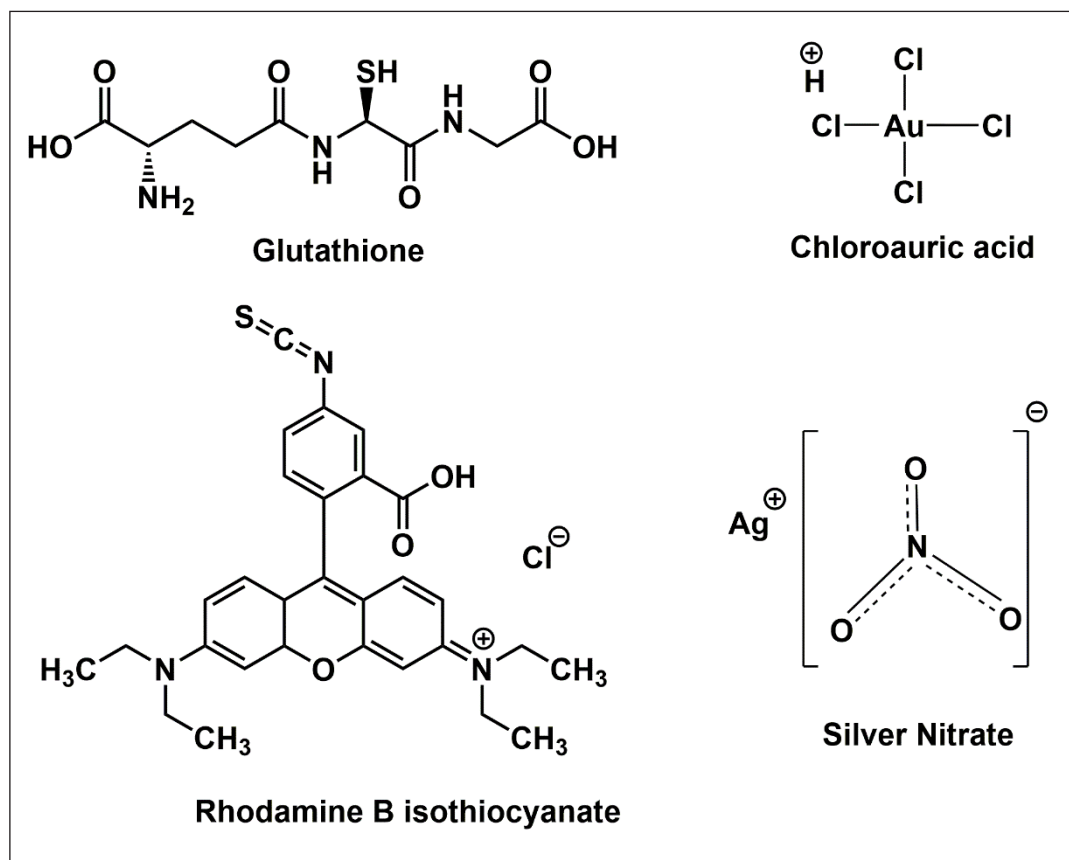
through Förster resonance energy transfer (FRET).⁹⁻¹⁰ FRET is a non-radiative energy transfer mechanism occurring from a photoexcited donor to an acceptor through dipole-dipole interactions. This phenomenon, typically effective within a range of less than 10 nanometers, serves as a crucial tool for precisely measuring dynamic changes between molecular donor-acceptor pairs within diverse complex macromolecular systems.¹¹⁻¹⁵ The combination of a donor-acceptor couple comprised of inorganic-organic hybrid associates can lead to synergistic effects, resulting in unique optical, electrical, magnetic, and catalytic properties that differ from those of the

individual constituents. In this regard, bimetallic nanoparticles (BNPs) represent a significant advancement in the field of nanotechnology, offering unique properties and applications compared to their monometallic counterparts. The combinatorial effects of incorporating two different metals into the nanoparticle framework can result in improved optical and electronic features. Additionally, these properties of BNPs can be further tailored to specific needs by adjusting the synthesis procedures, metal atoms, and capping agents. Due to this, BNPs have been employed in a wide range of applications across fields such as sensing, catalysis, biomedical, and optoelectronics.¹⁶⁻¹⁸ Particularly, the combination of BNPs with organic dye stands as a promising prospect to boost the efficiency of light harvesting processes, primarily due to the robust coupling between inorganic and organic components. However, research investigating the relationship between interparticle interactions (within inorganic metal nanoparticles and organic dye/dye aggregates) and the optical properties of these hybrid hetero-structured systems is currently limited. Therefore, developing inorganic-organic nanohybrid systems with eco-friendly nanomaterials and a thorough understanding of their mechanisms is expected to significantly contribute to designing efficient energy harvesting systems for both optoelectronic and biological applications.

In this context, it is pertinent to highlight that recent investigations have leveraged fluorescent semiconductor quantum dots (QDs) to investigate their interactions with dyes or J-aggregates. These studies on semiconductor hybrid nanoparticles mainly aim to understand how energy is transferred between semiconductor quantum dots (QDs) and J-aggregates.¹⁹⁻²³ Notably, Bawendi and co-workers^{19, 21-22}, as well as Rakovich and co-workers⁶, have independently conducted noteworthy studies. They've shown that QD/J-aggregate Förster resonance energy transfer (FRET) pairs hold promise for optoelectronic applications due to

their observed high electronic coupling between two components. In another work, Gryczynski and co-workers²⁴ have demonstrated that Bovine serum albumin (BSA) protected metal nanoclusters (Au and Ag) can effectively function as both acceptors and donors for short-lived organic fluorophores, enabling the creation of inorganic-organic nanohybrids for RET probes. The above discussions suggest that although some studies exist, the majority of research in this area involves quantum dots, carbon-based fluorophores, and organic dye molecules as donors, with AuNPs and AgNPs as acceptors. Hence, there is a scarcity of studies exploring the interaction between bimetallic nanomaterials as donors and organic dye as acceptors.

Keeping the above facts in mind, we have designed and developed an inorganic-organic hybrid associate system by integrating an inorganic luminescent bimetallic nanomaterial and organic dye to study the inter-particle electronic interaction between them. In the present hybrid system, the F-AgAu has been chosen as the inorganic component due to its water solubility and less toxic nature, whereas the organic dye (RBITC) has been chosen as the acceptor molecule as it satisfies the spectral overlap criterion for the RET process, that is, the absorption spectrum of RBITC has significant overlap with the emission spectrum of the F-AgAu that is used in this study. Prior investigating the photo-physics of this inorganic-organic nanohybrid, we have synthesised F-AgAu by following reported protocols and characterised by using conventional methods. This study has indicated a high efficiency in the energy-transfer process from F-AgAu nanoparticles to RBITC, confirming the presence of electronic coupling between the inorganic and organic components in the hybrid nanomaterial. The chemical structures of the compounds that are used in the present study are shown in Scheme 1.



Scheme 1. Molecular structures of the chemicals used in this study.

2. EXPERIMENTAL SECTION

2.1. Materials. Silver nitrate (AgNO_3), Chloroauric acid trihydrate ($\text{HAuCl}_4 \cdot 3\text{H}_2\text{O}$), L-glutathione (GSH) and Rhodamine B isothiocyanate (RBITC) were purchased from Sigma-Aldrich. All reagents were used without further purification. Milli-Q water was used throughout the experiment.

2.2. Instrumentation. Steady-state absorption and emission data were obtained using a Cary 100 Bio spectrophotometer and a Cary Eclipse fluorescence spectrophotometer, respectively. Time-resolved fluorescence measurements were conducted with a time-correlated single photon counting (TCSPC) spectrometer (Life Spec-II), utilizing a light-emitting diode ($\lambda_{\text{ex}} = 375$ nm) for probe excitation, and a dilute aqueous solution of ludox was employed to record the lamp profile. The fluorescence decay curves were analyzed through a nonlinear least squares

iteration procedure using F900 decay analysis software, with the quality of the fit assessed by chi-square (χ^2) values and weighted deviation. Zeta potential measurements were performed using a Malvern Zetasizer particle analyzer equipped with a helium-neon laser at 632 nm. Transmission electron microscopy (TEM) was employed for determining size and morphological characterization of the nanomaterials. For compositional analysis, an energy-dispersive X-ray microanalyzer attached to a field emission scanning electron microscope (FESEM) was utilized. Additionally, the incorporation of ligands over the nanomaterial surfaces was investigated using a Thermo Scientific FTIR setup.

2.3. Synthesis of Fluorescent Silver-Capped Gold Core Shell Nanoparticle (F-AgAu).

Fluorescent silver-gold nanoparticles were synthesized by slightly modifying a previously

reported protocol.²⁵ In brief, 4 mL of Milli-Q water, 2 mL of 5 mM aqueous GSH solution, 200 mL of 10 mM HAuCl₄, and 340 mL of 10 mM AgNO₃ were mixed in a 15 mL vial, resulting in the immediate appearance of a white turbid solution. Then the mixture was then subjected to ultraviolet light (350 nm) for 15 hours under vigorous stirring. A faint yellow solution was obtained, which was stored at 4°C for further use.

2.4 Sample Preparation and quantum yield calculation. All solutions were prepared in Milli-Q water. The fluorescence quantum yields of the systems were estimated using a standard reference Rhodamine 6G (R6G) dissolved in water, using the following equation

$$QY_S = \frac{I_S}{I_R} \times \frac{\eta_S^2}{\eta_R^2} \times QY_R \quad (1)$$

where QYS and QYR are the quantum yields of the sample and reference (for R6G in ethanol, QYR = 95%) respectively. IS and IR are the integrated fluorescence emission of the sample and the reference, respectively, determined by integrating the emission spectra over the whole spectral range. ZS and ZR are the refractive index of water (1.33) and ethanol (1.36), respectively.

3. Result and discussion

3.1 Characterization of F-AgAu and Au NPs.

The synthesized F-AgAu has been extensively characterized by using conventional spectroscopic and microscopic techniques. Primarily, the system is characterized by steady-state absorption and emission measurements provided in Fig. 1. It can be seen from Fig. 1(a) that F-AgAu shows a broad absorption band without any plasmonic peak. The absence of any characteristic plasmonic bands of silver and gold nanoparticles can be rationalized by considering the plasmon damping phenomenon which might have been caused in the present system due to the coating of silver nanoclusters on the surface of gold.²⁶⁻²⁸ Moreover, it can also be seen from Fig. 1(a) that F-AgAu exhibiting high fluorescence emission behaviour with an

emission maximum at 570 nm upon excitation at 375 nm. It is reported that F-AgAu is composed of a large gold nanoparticle core covered by a silver nanocluster shell.²⁵ The fluorescence behaviour of F-AgAu is reported to arise due to the fluorescence properties of the silver nanoclusters, which are synergistically stabilized by the gold core.^{25, 29} The size and morphology of the particles are determined from the TEM image (Fig. 1(b)). It can be seen from the TEM image, that the particles are spherical in shape. The estimated size of F-AgAu is ~480 nm. Elemental analysis of these systems has been performed from the EDAX spectrum, which is provided in the Figure 1d. The surface charges of these systems are determined by z-potential measurements, which are shown in the Figure 3. FTIR measurements are performed to investigate the incorporation of the ligands over the nanomaterial surface. Fig. 1(c) shows a peak at 2525 cm⁻¹ which corresponds to the -S-H stretching vibration of GSH. However, this peak disappeared in the spectrum of GSH-capped

F-AgAu, which suggests the coordination of GSH with F-AgAu via the thiol group. The peaks corresponding to the asymmetric (1599 cm⁻¹) and symmetric stretching (1517 cm⁻¹) modes of the carboxylate group of free GSH show a significant shift in F-AgAu. These FTIR data confirm the surface functionalization of F-AgAu by GSH.

3.2 Investigation of the RET process through steady state measurements

The interaction between the F-AgAu and RBTC has been studied using Förster Resonance Energy Transfer (FRET) studies. It is well known that, effective Förster Resonance Energy Transfer (FRET) communication relies on a significant overlap between the emission spectrum of the donor and the absorption spectrum of the acceptor. The success of FRET is also contingent on the close proximity of the donor and acceptor moieties, usually within a range of less than 100 Å. As shown in Figure 2a, there is a significant overlap between the emission spectrum of F-AgAu (donor) and the absorption spectrum

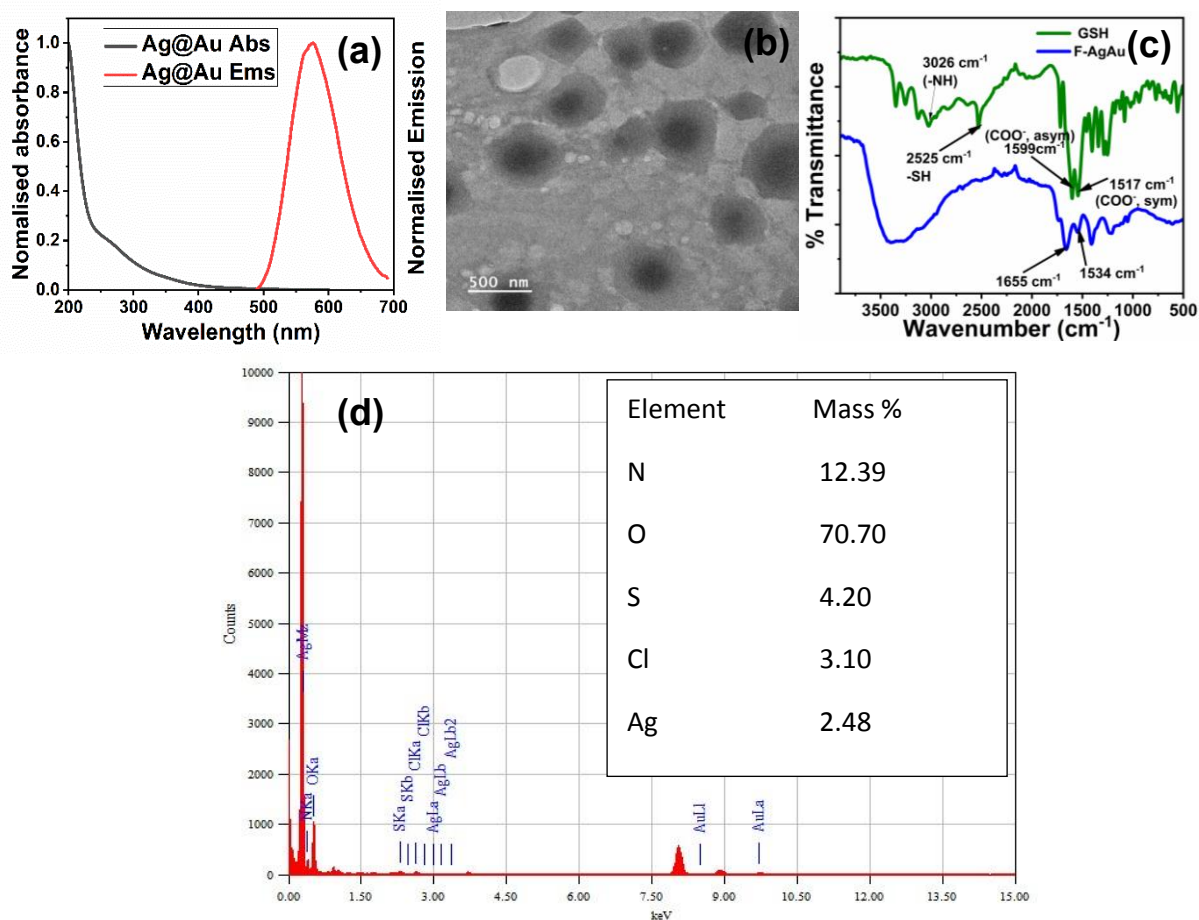


Figure 1. (a) Normalized absorption and emission spectra (b) TEM images (c) FTIR spectra and (d) EDAX spectra of F-AgAu.

of the RBITC (acceptor), confirming that they constitute a suitable FRET pair. The overlap integral $J(\lambda)$ has been estimated to be $2.79 \times 10^{17} \text{ M}^{-1} \text{ cm}^{-1} \text{ nm}^4$ by employing following equation

$$J(\lambda) = \int F_D(\lambda)\epsilon_A(\lambda)\lambda^4 d\lambda \quad (1)$$

where $F_D(\lambda)$ is the area-normalized emission spectrum of the donor, and $\epsilon_A(\lambda)$ denotes the molar absorption coefficient of the acceptor. Initially, the effect of RBITC on the optical properties of F-AgAu has been investigated through, steady-state fluorescence titration experiments which have been carried out by monitoring the fluorescence of F-AgAu with an increasing concentration of RBITC (Figure 2b).

In this study, we have excited the donor (F-AgAu) at 365 nm excitation wavelength to minimize interference from the acceptor's

(RBITC) absorption at this specific wavelength. As depicted in Figure 2b, the emission intensity of F-AgAu is significantly quenched in the presence of the RBITC, accompanied by the emergence of a pronounced emission band at the wavelength corresponding to the RBITC dye. The observed concurrent decrease in donor intensity and the rise in acceptor intensity distinctly signify energy transfer from F-AgAu to the RBITC in this hybrid structure. It's worth noting that a similar rationale has been put forward in explaining the FRET process between quantum dots (QDs) and organic dye molecules.^{7, 19, 30} It's important to note here that for the FRET process, the close association of donor and acceptor moieties in the hybrid system has been usually accomplished through dipole-dipole interaction (electrostatically driven).³¹ But in the present study, zeta potential

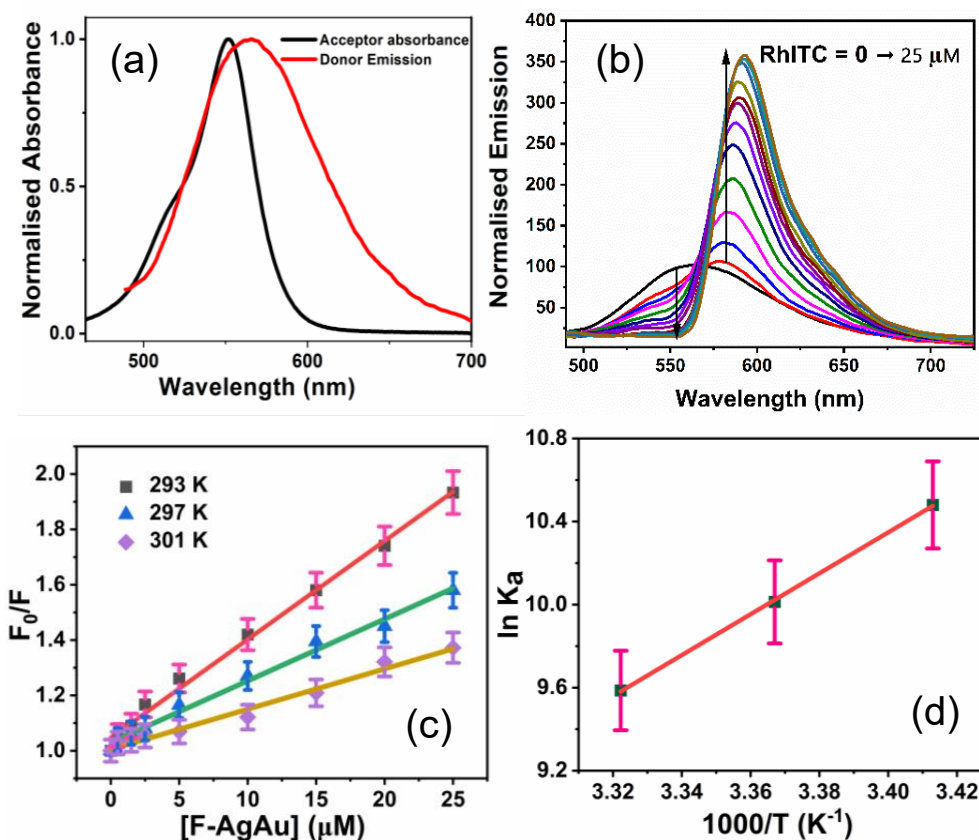


Figure 2. (a) Spectral overlap between the absorption spectrum of acceptor (RBITC) and PL spectrum of donor (F-AgAu) (b) Fluorescence spectra of F-AgAu in the presence of an increasing concentration of RBITC. (c) Stern–Volmer plots for F-AgAu at different temperatures. (d) Van’t Hoff graph for the hybrid system of F-AgAu and RBITC.

measurements (Figure 3) indicate that both F-AgAu and RBITC possess a positive surface charge, creating a positive-positive repulsion between these two components. However, the isothiocyanate group in RBITC, with a highly electrophilic carbon atom, is known to selectively interact with primary amines.³² Therefore, the free amine of glutathione (the capping ligand) in F-AgAu can engage with the electrophilic carbon of the isothiocyanate group, forming a stable nano-assembly that overcomes the positive-positive repulsion. Additionally, the hydroxyl group of the carboxylic group in both RBITC and the capping ligand can contribute to hydrogen bonding interactions. This collective interaction overcomes the positive-positive repulsion of the surface charges in both donor and acceptor, bringing the FRET pair close together to have an efficient FRET communication between them.

3.3 Thermodynamics studies

It is pertinent to mention here that understanding the thermodynamics of the binding event between donor and acceptor is very crucial as it provides valuable information on the feasibility of the process, nature of interaction, forces of binding, etc.³³⁻³⁴ To elucidate the interaction between the donor-acceptor systems, we have estimated the relevant thermodynamic parameters for the interaction between F-AgAu and RBITC by utilising the fluorescence quenching data of F-AgAu in the absence and presence of RBITC. Initially, we have resorted to Stern–Volmer (SV) analysis to investigate the quenching mechanism. The SV equation is given by:

$$\frac{F_0}{F} = 1 + K_{SV}[Q] \quad (2)$$

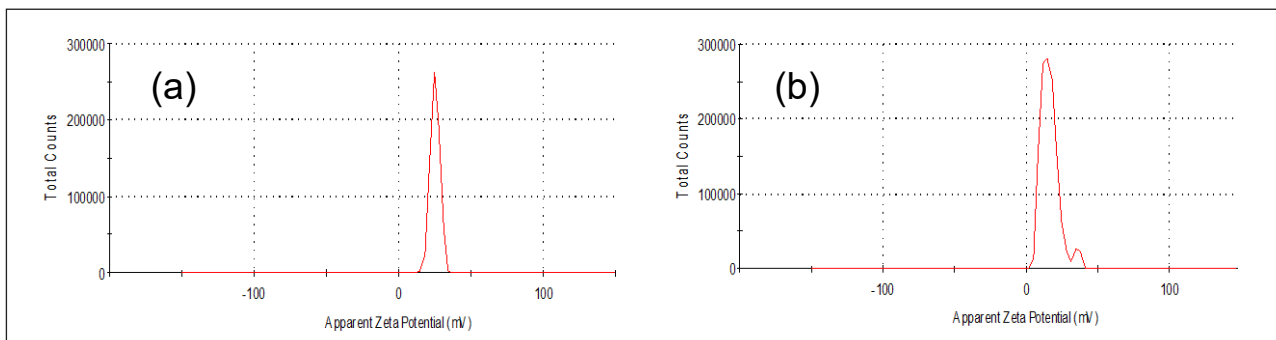


Figure 3. Zeta potential graph of (a) RBITC and (b) F-AgAu

where I_0 and I are the fluorescence intensities of F-AgAu in the absence and presence of RBITC, respectively, and K_{SV} is the Stern-Volmer constant. The plot of I_0/I vs quencher concentration ($[Q]$) at various temperatures is shown in Figure 2c. The plot in Figure 2c illustrates a linear Stern–Volmer relationship as the fluorescence quenching varies with the concentration of RBITC ($[Q]$). The obtained values of the Stern–Volmer constant (K_{SV}) and bimolecular quenching constant ($= K_{SV}/\tau_D$) at various temperature are summarized in Table 1. From the table it can be seen that the estimated bimolecular quenching constant values are in the order of $\sim 10^{12}$ M. It is to be noted here that this quenching rate constant exceeds the typically expected diffusion-controlled rate constant (10^{10} M⁻¹ s⁻¹). Furthermore, temperature-dependent fluorescence studies have indicated a significant decrease in the slope of the Stern–Volmer line as the system’s temperature rises. As a result, K_{SV} is found to decrease with increasing temperature (Table 1). This behaviour suggests

that the reduction in the fluorescence intensity of F-AgAu upon RBITC addition is predominantly static in nature. It’s worth mentioning that similar arguments supporting the static nature of the quenching process have been presented in the literature for other hybrid systems.^{2, 8, 31} In such cases, the slope of the F_0/F against $[Q]$ plot is considered for predicting the binding constant value associated with the binding event, and it can be utilized to determine thermodynamic parameters using van’t Hoff equations 3 and 4.

$$\ln K_a = -\left(\frac{\Delta H}{R}\right)\frac{1}{T} + \frac{\Delta S}{R} \quad (3)$$

$$\Delta G = \Delta H - T\Delta S \quad (4)$$

where T is the temperature, R is the gas constant, ΔH is the enthalpy change, ΔS is the entropy change, and ΔG is the free energy change on adsorption of the dye on the surface of the F-AgAu nanoparticle. The van’t Hoff plot is shown in Figure 2d and the corresponding values of ΔH and ΔS are determined from the slope and intercept of the plot, respectively which are provided in the Table 1. It can be seen from Table 1 that ΔH is negative, which indicates that the interaction between F-AgAu and the dye is exothermic. Interestingly, from Table 1, one can also see that ΔS is also negative, which indicates that the entropy of the system decreased during this process. It has been reported in previous studies[ref] that hydrogen bonding and van der Waals interaction may be the cause for the negative enthalpy change and negative entropy change.³⁵⁻³⁷ The negative value of ΔG (Table 1) demonstrates that the interaction between F-AgAu and the dye is a spontaneous process.

Table 1. Stern–Volmer Quenching Constant and Thermodynamic Parameters for the Interaction between F-AgAu and RBITC Dye at Different Temperatures:

T (K)	Ksv (10 ⁴ M ⁻¹)	Kq (10 ¹² M ⁻¹ s ⁻¹)	ΔH (kJ mol ⁻¹)	ΔS (J mol ⁻¹ K ⁻¹)	ΔG (kJ mol ⁻¹)
293	3.59	5.1			-25.5
297	2.23	3.2	-81.91	-192.47	-24.75
301	1.45	2.2			-23.98

3.4 Time-Resolved Fluorescence Measurements.

To gain deeper insights into the Förster Resonance Energy Transfer (FRET) process, we have conducted time-resolved fluorescence intensity decay measurements on F-AgAu solution in the absence and presence of RBITC. The representative fluorescence decay curves and the relevant decay parameters are provided in the Figure 4a and Table 2 respectively. The fluorescence intensity decay curves for F-AgAu nanoparticles have exhibited significant quenching of the fluorescence lifetime in the presence of RBITC. The average fluorescence lifetime of

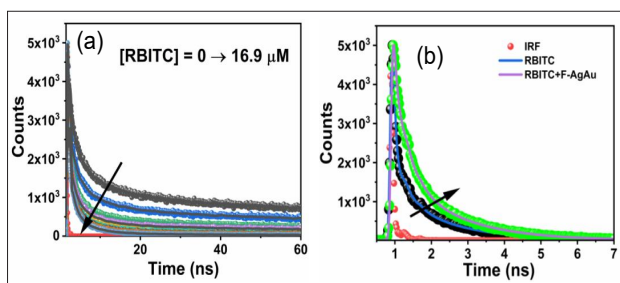


Figure 4. Time-resolved fluorescence decay curve for (a) F-AgAu in the absence and presence of RBITC and (b) RBITC and F-AgAu/RBITC hybrid system using an excitation wavelength of 375 nm.

F-AgAu is found to decrease significantly from 6.89 ns to 0.56 ns in the presence of RBITC. It is to be noted here that the applicability of Förster theory in explaining the energy-transfer process involving metal nanoclusters has been previously demonstrated.^{24, 38-39} Conversely, it should also be kept in mind that surface energy transfer mechanisms may come into play when the dipole of a molecule interacts with the continuum of energy states present in large-sized metal nanoparticles.⁴⁰⁻⁴¹ Given that silver nanoclusters interacting with RBITC possess discrete energy states, they are less likely to facilitate such coupling interactions, as indicated by previous research.⁴²

β are expressed in % scale and τ values (± 5 %) are in ns unit

Based on our experimental findings as well as literature report it can safely be depicted that the Förster mechanism of energy transfer is happening from F-AgAu to RBITC dye molecules. Therefore, in the current scenario, the data is analyzed using the Förster theory. The energy-transfer efficiency between F-AgAu and RBITC is calculated to be 92% by employing eq 5

Table 2. Fluorescence decay parameters of F-AgAu with gradual addition of RBITC dye: (Excitation wavelength is 375 nm)

RBITC (μM)	τ_1	β_1	τ_2	β_2	τ_3	β_3	$\langle\tau\rangle$
0	0.51	52	3.88	35	37.18	13	6.89
0.5	0.38	63	3.36	30	32.14	7	3.97
1.5	0.34	78	2.82	19	25.80	3	1.76
2.5	0.34	80	2.81	18	24.83	2	1.39
5	0.34	75	2.37	22	14.87	3	1.24
7.5	0.36	78	2.45	19	14.14	3	1.15
10	0.28	83	2.14	15	11.19	2	0.80
12.5	0.23	85	1.89	14	9.45	1	0.64
15	0.26	84	1.93	15	9.25	1	0.70
25	0.24	88	1.99	11	9.36	1	0.56

$$E = 1 - \frac{\tau_{DA}}{\tau_D} \quad (5)$$

where E is the energy-transfer efficiency, τ_{DA} and τ_D are the average fluorescence lifetime of the donor in the presence and absence of the acceptor, respectively. The notable FRET efficiency in this study confirms the existence of efficient electronic coupling between the inorganic F-AgAu and the organic RBITC dye in the hybrid system. It is known that the Förster distance (R_0) stands out as a pivotal parameter in the FRET model, generally falling within the range of 2-10 nm for a specific donor-acceptor system. This R_0 value is determined by using the following equation

$$R_0 = [(8.8 \times 10^{-25})(\kappa^2 \eta^{-4} \phi_D J(\lambda))]^{1/6} \quad (6)$$

where κ^2 (= 2/3) is the orientation factor of the transition dipoles of the donor and the acceptor, η is the refractive index of the medium, ϕ_D is the quantum yield of the donor, and $J(\lambda)$ is the spectral overlap integral between the donor emission and the acceptor absorption spectrum. In this study, the calculated R_0 value for the F-AgAu-RBITC pair is estimated to be 7.2 nm which falls under FRET model. The distance between donor and acceptor and the rate of energy transfer have been calculated by using eq. 7 and eq. 8 respectively.

$$E = \frac{R_0^6}{R_0^6 + r^6} \quad (7)$$

$$k_T = \frac{1}{\tau_D} \left(\frac{R_0}{r} \right)^6 \quad (8)$$

All the FRET parameters are tabulated in the Table 4. We have also examined the fluorescence intensity decay of dye aggregates in the absence and presence of F-AgAu, monitoring fluorescence at $\lambda_{em} = 590$ nm. The representative fluorescence decay plot and the relevant decay parameters are provided in Figure 4b and Table 3 respectively. The observed increment of the fluorescence lifetime of the RBITC dye, from 0.18 ns to 0.39 ns in the presence of F-AgAu (as indicated in Table 3), The variance in fluorescence lifetime values observed between the hybrid system and the free dye molecules may arise from the distinct local field environments experienced by the dye molecules in the presence of the positively charged F-AgAu particle compared to its environment in the solution. This finding strongly indicates the formation of an inorganic-organic hybrid system.⁴³

4. CONCLUSIONS

This study has investigated the photophysical properties of an inorganic-organic hybrid heterostructured material combined with fluorescent bimetallic F-AgAu and organic dye

Table 3. Fluorescence decay parameters of RBITC dye in absence and presence of F-AgAu: (Excitation wavelength is 375 nm)

Sample	τ_1	β_1	τ_2	β_2	τ_3	β_3	$\langle \tau \rangle$
RBITC	0.05	84.5	0.36	8.6	1.58	6.9	0.18
RBITC + F-AgAu	0.05	48.8	0.31	34.2	1.54	17	0.39

β are expressed in % scale and τ values (± 5 %) are in ns unit

Table 4. FRET parameters obtained from steady state and time-resolve fluorescence studies

System	$J(\lambda)$ ($M^{-1} cm^3$)	QY (%)	R_0 (nm)	E (%)	(R) (nm)	κ_T (s^{-1})
F-AgAu+RBITC	2.79×10^{17}	4	7.19	92	5.30	9.1×10^8

molecules (RBITC) by employing FRET method. The interaction between F-AgAu particles and RBITC has been examined using steady-state absorption and emission spectroscopy, as well as time-resolved fluorescence spectroscopy. Experimental results obtained from the steady state measurements have revealed a decrease in F-AgAu fluorescence intensity and a simultaneous increase in RBITC fluorescence upon selective excitation of F-AgAu. These findings, supported by fluorescence lifetime studies, confirm that the deactivation of the excited state of F-AgAu is attributed to an energy-transfer process. The energy-transfer efficiency for this hybrid system is estimated to be 92 %, indicating an efficient electronic coupling between BNPs and organic dye molecules. Therefore, outcome of the present study provides valuable insights which can be utilized for the design of efficient inorganic-organic hybrid systems for energy-related applications. Moreover, as the present hybrid structure is fabricated based on nontoxic fluorescent metal nanoparticles, it can also be used in bioimaging and sensing applications.

5. Acknowledgments

AA acknowledges the Department of Science and Technology (DST) for providing the fellowship (Reference no. DST/INSPIRE Fellowship/2018/IF180141). AA thanks the National Institute of Science Education and Research (NISER), Bhubaneswar, for infrastructure. The authors acknowledge the Centre for Interdisciplinary Sciences (CIS), NISER for TEM facilities. AM and DC acknowledges the Council of Scientific and Industrial Research (CSIR), India, for the fellowship.

6. References

- Kundu, S.; Patra, A., *Chem. Rev.* **2017**, *117*, 712-757.
- Devatha, G.; Roy, S.; Rao, A.; Mallick, A.; Basu, S.; Pillai, P. P., *Chem. Sci.* **2017**, *8*, 3879-3884.
- Thomas, A.; Sandeep, K.; Somasundaran, S. M.; Thomas, K. G., *ACS Energy Lett.* **2018**, *3*, 2368-2375.
- Ray, R.; Sarkar, A. S.; Pal, S. K., *Sol. Energy* **2019**, *193*, 95-101.
- Wang, Y.-Y.; Xiang, X.; Yan, R.; Liu, Y.; Jiang, F.-L., *J. Phys. Chem. C* **2018**, *122*, 1148-1157.
- Savateeva, D.; Melnikau, D.; Lesnyak, V.; Gaponik, N.; Rakovich, Y. P., *J. Mater. Chem.* **2012**, *22*, 10816-10820.
- Preeyanka, N.; Dey, H.; Seth, S.; Rahaman, A.; Sarkar, M., *Phys. Chem. Chem. Phys.* **2020**, *22*, 12772-12784.
- Das, A.; Roy, D.; Mandal, M.; Jaiswal, C.; Ta, M.; Mandal, P. K., *J. Phys. Chem. Lett.* **2018**, *9*, 5092-5099.
- J. R. Lakowicz, *Principles of Fluorescence Spectroscopy*, Springer, USA, **2006**.
- B. Valeur, *Molecular Fluorescence: Principles and Applications*. Wiley-VCH, Weinheim, **2002**.
- Cotlet, M.; Vosch, T.; Habuchi, S.; Weil, T.; Müllen, K.; Hofkens, J.; De Schryver, F., *J. Am. Chem. Soc.* **2005**, *127*, 9760-9768.
- Arslan, S.; Khafizov, R.; Thomas, C. D.; Chemla, Y. R.; Ha, T., *Science* **2015**, *348*, 344-347.
- Michalet, X.; Weiss, S.; Jäger, M., *Chem. Rev.* **2006**, *106*, 1785-1813.
- Zhang, Y.; Zhang, H.; Hollins, J.; Webb, M. E.; Zhou, D., *Phys. Chem. Chem. Phys.* **2011**, *13*, 19427-19436.
- Peng, X.; Chen, H.; Draney, D. R.; Volcheck, W.; Schutz-Geschwender, A.; Olive, D. M., *Anal Biochem* **2009**, *388*, 220-8.
- Christensen, S. T.; Feng, H.; Libera, J. L.; Guo, N.; Miller, J. T.; Stair, P. C.; Elam, J. W., *Nano Lett.* **2010**, *10*, 3047-3051.
- Huang, H.; Li, H.; Feng, J.-J.; Wang, A.-J., *Sens. Actuators B Chem.* **2016**, *223*, 550-556.
- Jena, P.; Bhattacharya, M.; Bhattacharjee, G.; Satpati, B.; Mukherjee, P.; Senapati, D.; Srinivasan, R., *Nanoscale* **2020**, *12*, 3731-3749.
- Halpert, J. E.; Tischler, J. R.; Nair, G.; Walker, B. J.; Liu, W.; Bulović, V.; Bawendi, M. G., *The J. Phys. Chem. C* **2009**, *113*, 9986-9992.
- Liu, S.; Sun, H.; Ma, Y.; Ye, S.; Liu, X.; Zhou, X.; Mou, X.; Wang, L.; Zhao, Q.; Huang, W., *J. Mater. Chem.* **2012**, *22*, 22167-22173.
- Freyria, F. S.; Cordero, J. M.; Caram, J. R.; Doria, S.; Dodin, A.; Chen, Y.; Willard, A. P.; Bawendi, M. G., *Nano Lett.* **2017**, *17*, 7665-7674.
- Walker, B. J.; Bulović, V.; Bawendi, M. G., *Nano Lett.* **2010**, *10*, 3995-9.
- Chakraborty, D.; Akhuli, A.; Preeyanka, N.; Sarkar, M., *J. Phys. Chem. C* **2023**, *127*, 5082-5089.
- Raut, S.; Rich, R.; Fudala, R.; Butler, S.; Kokate, R.; Gryczynski, Z.; Luchowski, R.; Gryczynski, I., *Nanoscale* **2014**, *6*, 385-391.
- Ganguly, M.; Pal, A.; Negishi, Y.; Pal, T., *Langmuir* **2013**, *29*, 2033-2043.
- Yuvasri, G. S.; Goswami, N.; Xie, J., In *Principles and Applications of Aggregation-Induced Emission*, Tang, Y.; Tang, B. Z., Eds. Springer International Publishing: Cham, 2019; pp 265-289.
- Kumar, M.; Dey, J.; Verma, M. S.; Chandra, M., *Nanoscale* **2020**, *12*, 11612-11618.
- Xu, P.; Lu, X.; Zhao, J.; Li, Y.; Chen, S.; Xue, J.; Ou, W.; Han, S.; Ding, Y.; Ni, W., *Nano* **2016**, *11*, 1650099.
- Jana, J.; Aditya, T.; Pal, T., *Dalton Trans.* **2018**, *47*, 3580-3587.
- Chaudhari, S.; Srinivasan, M., *J. Mater. Chem.* **2012**, *22*, 23049-23056.
- Agrawal, A. K.; Sahu, P. K.; Seth, S.; Sarkar, M., *J. Phys. Chem. C* **2019**, *123*, 3836-3847.
- Barbero, N.; Barolo, C.; Viscardi, G., *World J. Chem. Educ.* **2016**, *4*, 80-85.

33. Akhuli, A.; Chakraborty, D.; Agrawal, A. K.; Sarkar, M., *Langmuir* **2021**, *37*, 1823-1837.
34. Akhuli, A.; Chakraborty, D.; Preeyanka, N.; Dora, A. S.; Sarkar, M., *ACS Appl. Nano Mater.* **2023**, *6*, 4910-4924.
35. Bharmoria, P.; Rao, K. S.; Trivedi, T. J.; Kumar, A., *J. Phys. Chem. B* **2014**, *118*, 115-124.
36. Preeyanka, N.; Akhuli, A.; Dey, H.; Chakraborty, D.; Rahaman, A.; Sarkar, M., *Langmuir* **2022**, *38*, 10704-10715.
37. Ross, P. D.; Subramanian, S., *Biochemistry* **1981**, *20*, 3096-3102.
38. Ghosh, S.; Das, N. K.; Anand, U.; Mukherjee, S., *J. Phys. Chem. Lett.* **2015**, *6*, 1293-8.
39. Xiao, Y.; Shu, F.; Wong, K. Y.; Liu, Z., *Anal. Chem.* **2013**, *85*, 8493-7.
40. Yun, C. S.; Javier, A.; Jennings, T.; Fisher, M.; Hira, S.; Peterson, S.; Hopkins, B.; Reich, N. O.; Strouse, G. F., *J. Am. Chem. Soc.* **2005**, *127*, 3115-3119.
41. Akhuli, A.; Preeyanka, N.; Chakraborty, D.; Sarkar, M., *Phys. Chem. Chem. Phys.* **2023**, *25*, 17470-17481.
42. Jin, R., *Nanoscale* **2010**, *2*, 343-362.
43. Madigan, C.; Bulović, V., *Phys. Rev. Lett.* **2006**, *96*, 059901.

	Mr. Amit Akhuli received his M. Sc degree in chemistry from central university Gujarat in 2017 and joined School of Chemical Sciences NISER, Bhubaneswar in 2018 as a Ph.D. student under the supervision of Dr. Moloy Sarkar. His current research interests focus on the interaction of luminescent metal nanocluster with various biological and environmental targets analytes.
	Ms. Aditi Mahanty is currently doing her BS-MS in chemical sciences at IISER Berhampur. She is currently working on her MS-project under the guidance of Dr. Moloy Sarkar. Her current research includes understanding of the photo-physics of various nano particles in presences various analytes.
	Ms. Amita Mahapatra Received her Master degree from Ravenshaw University Cuttack in 2016. She the joined NISER in 2018 as a Ph.D. student under the supervision of Dr. Moloy Sarkar. Her current research focus includes investigation of intermolecular interaction and structural organization of room temperature ionic liquids and their implications in biological and electrochemical applications
	Mr. Debabrata Chakraborty Received his M.Sc. Degree in Chemistry from Vidyasagar University Medinipur West Bengal in 2017. He joined School of Chemical Science NISER, Bhubaneswar in 2018 as a research fellow under the supervision of Dr. Moloy Sarkar. His current research includes understanding the photo physics of perovskite materials and semiconductor quantum dots.
	Dr. Sahadev Barik obtained his M.Sc. and M.Phil. degree in chemistry from Utkal University Bhubaneswar in 2016 and 2017 respectively. Joining the School of Chemical Sciences NISER in 2018, he received his Ph.D. degree in 2023 under the guidance Dr. Moloy Sarkar. His research focus includes investigation of room temperature ionic liquids and deep eutectic solvents, exploring their structural dynamics in both pure form and amidst the influence of electrolytes and biomolecules.
	Dr. Moloy Sarkar obtained his M.Sc from the University of Burdwan in 2001. He received is Ph.D. degree from University of Hyderabad in 2007. Then he joined School of Chemical Sciences, NISER in 2009 as an assistant professor and currently working as an associate professor. His research interest includes study of photo physics of semiconductor quantum dots, perovskite nano materials and inorganic-organic nano hybrid systems for light harvesting process. Additionally, he is also interested in investigating the structural and dynamical behavior of room temperature ionic liquids and deep eutectic solvents. He has published nearly 90 research papers in peer reviewed journals and 7 students have obtained their PhD degree under his supervision.

Broad Photon Upconversion in Lanthanide Doped Inorganic Crystals

Annu Balhara,^{1,2} and Santosh K. Gupta^{1,2*}

¹Radiochemistry Division, Bhabha Atomic Research Centre, Trombay, Mumbai-400085, India

²Homi Bhabha National Institute, Anushakti Nagar, Mumbai-400094, India

Email: santoshg@barc.gov.in

Abstract:

Lanthanide-doped upconversion phosphors (UCPs) are anti-Stokes emitters, which can produce higher-energy ultraviolet/visible and near-infrared (NIR) luminescence when excited with low-energy NIR light. They are featured with non photobleaching, sharp emission peaks, super stability, low toxicity, low imaging background, and functional multimodality. These characteristics endow them to be useful as nanoprobes for diagnostic applications and imaging-guided cancer therapy. Importantly, the ability to convert tissue-penetrating NIR light into visible and ultraviolet range is quite useful in photodynamic therapy, photothermal therapies, color tunability, optical thermometry and drug delivery processes for efficacious cancer therapy. Here in this article we have explained about basic photophysics of various lanthanides ion, various mechanisms of upconversion process, few case studies on lanthanide doped UCPs wrt to solid state lighting, color tunability, photo thermal therapies, high and cryogenic temperature thermometry, singular emission and SPECT imaging. We have also included a section of various methodologies of UCNP's synthesis.

1. Introduction

Rare-earth (RE) elements consist of two Group IIIB elements (Sc and Y) and fifteen lanthanides (La to Lu). The ground state electronic configuration for Sc and Y is [Ar]3d¹4s² and [Kr]4d¹5s², respectively. Among the 15 lanthanides, four of them (La, Ce, Gd, and Lu) have the electronic configuration as [Xe]4fⁿ⁻¹5d¹6s², while other lanthanides have [Xe]4fⁿ6s² electronic configurations.¹ In general, RE exist in stable +3 oxidation state (RE³⁺) as the 2 electrons from the 6s orbital and one electron from the 5d/ 4f orbital can be easily removed. This result in a similar configuration, [Xe]4fⁿ⁻¹ of the trivalent lanthanide ions (Ln³⁺) from La³⁺ to Lu³⁺. However, some Ln³⁺ ions may exhibit unusual ionic states with +2 oxidation states (Eu²⁺ and Sm²⁺) and +4 oxidation state (Tb⁴⁺). This can be explained by the high stability of half-filled 4f shell in Eu²⁺ (f⁷) and Tb⁴⁺ (f⁷) ions. The optical properties of Ln³⁺ ions are characterized by their

f-f transitions. The completely filled outer 5s² and 5p⁶ sub-shells of Ln³⁺ ions effectively shield the 4f electrons. Therefore, electron phonon interactions of 4f electrons sharp are weak and sharp emissions arise from 4f-4f transitions.² Moreover, the long lifetimes of the excited 4f levels due to the parity forbidden intra 4f transitions favour the feasibility of UC emissions.³ The UC emissions ranging from ultraviolet (UV) to infrared (IR) region of electromagnetic spectrum can be achieved for different Ln³⁺ doped UC phosphors depending upon the energy levels. UC is defined as conversion of low energy photon to high energy photon via absorption of two photon and it depicts Anti-Stokes shift. UC can be categorized as conversion of NIR to UV, NIR to visible and visible to UV photon. Down conversion luminescence (DC) on the other hand is the conversion of high energy photon into low energy photon and display Stoke's shift. There is one more aspect of DC called as quantum cutting luminescence (QCL) wherein a high

Table 1: Different types of luminescence based on excitation mode²

Types:	Mode of excitation	Importance/ Application
Photoluminescence	Photon	LEDs, display panels
Radioluminescence	Ionizing radiation (γ , α , β , X-rays etc.)	Scintillators, biomedicine, dosimetry
Triboluminescence	Frictional and electrical forces, mechanical energy	Sensor, aerospace, defense sector, civil constructions
Bioluminescence	Biological process	Imaging, dairy industry, biocidal disinfection
Chemiluminescence	Chemical process	Pharmaceutical, clinical, analytical, gas analysis
Cathodoluminescence	Cathode ray/electron beam	Pharmaceutical, mineralogy, display
Thermoluminescence	Heating after pre storage of energy	Dosimetry, optical materials, medicine
Sonoluminescence	Ultrasounds	Chemical and allied industries, therapeutic medicine

energy photon is converted into 2 low energy photons. Further luminescence is differentiated based on the way excitation is triggered. *Table 1* categorized different types of luminescence, mode of excitation, their importance, and few specific applications.

For instance, different transitions and upconversion emissions by selecting the Ln^{3+} ions as dopants over the full visible spectrum is

illustrated by *Fig 1a, b*. Though, UC emission can be theoretically predicted for Ln^{3+} ions, the generation of UC emissions requires closely lying intermediate levels with energy similar to NIR excitation to facilitate effective photon absorption and UC processes.⁴ Mainly, Er^{3+} , Ho^{3+} and Tm^{3+} ions with ladder-like 4f energy states are dispersed as optically active centers in different host matrices to achieve UC emissions.⁵

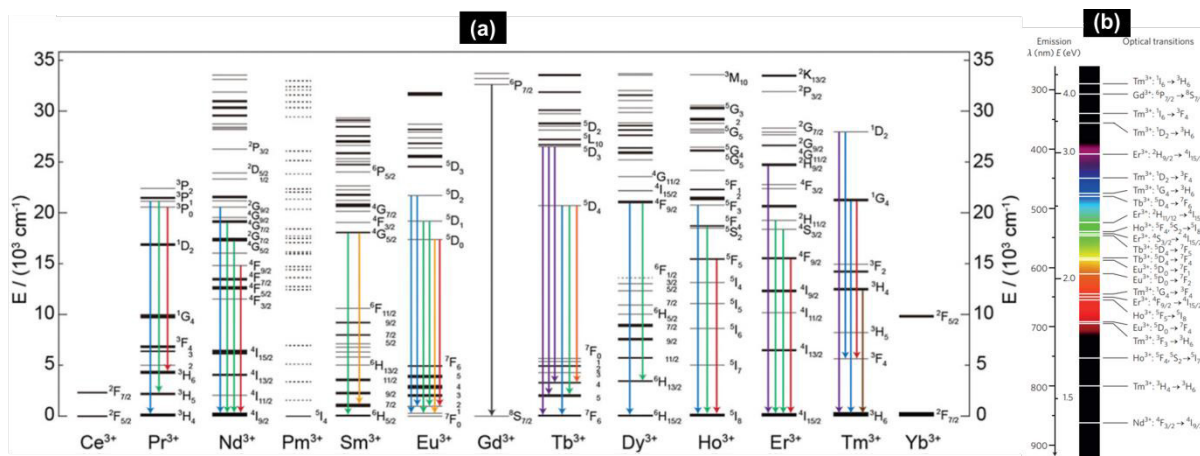


Figure 1: (a) Partial energy level diagram for lanthanide cations used for broad upconversion emissions,⁷ (b) Typical Ln^{3+} -based upconversion emission bands covering a broad range of wavelengths from ultraviolet (~290 nm) to NIR (~880 nm) and their corresponding main optical transitions.⁸

Table 2: Characteristic optical properties of Er³⁺, Ho³⁺ and Tm³⁺ ions incorporated in different phosphor materials

Lanthanide ion	Composition of UC phosphor	<i>f</i> → <i>f</i> Transitions	λ _{em} (nm)	λ _{ex} (nm)	Ref.
Er ³⁺	β-NaYF ₄ :Yb ³⁺ , Er ³⁺	² H _{9/2} → ⁴ I _{15/2} ² H _{11/2} → ⁴ I _{15/2} ⁴ S _{3/2} → ⁴ I _{15/2} ⁴ F _{9/2} → ⁴ I _{15/2}	~408 ~523 ~543 ~655	980 nm	9
	Ca ₂ MgWO ₆ :Er ³⁺ , Yb ³⁺	² H _{11/2} → ⁴ I _{15/2} ⁴ S _{3/2} → ⁴ I _{15/2} ⁴ F _{9/2} → ⁴ I _{15/2}	~531 ~549 ~661	980	10
	NaYF ₄ :Nd ³⁺ , Yb ³⁺ , Er ³⁺	² H _{11/2} → ⁴ I _{15/2} ⁴ S _{3/2} → ⁴ I _{15/2} ⁴ F _{9/2} → ⁴ I _{15/2}	~523 ~548 ~660	808	11
Ho ³⁺	CaF ₂ : Yb ³⁺ /Ho ³⁺ /Gd ³⁺	⁵ F ₄ , ⁵ S ₂ → ⁵ I ₈ ⁵ F ₅ → ⁵ I ₈ ⁵ F ₄ / ⁵ S ₂ → I ₇	~540 ~642 ~757	980	12
	LiYF ₄ :Yb ³⁺ , Ho ³⁺	⁵ F ₄ , ⁵ S ₂ → ⁵ I ₈ ³ K ₈ , ⁵ F ₂ , ⁵ F ₃ → ⁵ I ₇ ⁵ F ₅ → ⁵ I ₈	~535, 543 ~638 ~657	976	13
	Y ₂ O ₃ :Ho ³⁺ -Yb ³⁺ -Zn ²⁺	³ K ₈ → ⁵ I ₈ ⁵ F ₃ → ⁵ I ₈ ⁵ F ₄ , ⁵ S ₂ → ⁵ I ₈ ⁵ F ₅ → ⁵ I ₈ ⁵ S ₂ → ⁵ I ₇	~465 ~491 ~546 ~658 ~757	980	14
	LaNbO ₄ : Nd ³⁺ /Yb ³⁺ /Ho ³⁺	⁵ F ₄ , ⁵ S ₂ → ⁵ I ₈ ⁵ F ₅ → ⁵ I ₈	~539.6 ~651.2	808	15
Tm ³⁺	NaYF ₄ :Yb ³⁺ /Tm ³⁺ @NaYF ₄ :Yb ³⁺	¹ I ₆ → ³ H ₆ ¹ G ₄ → ³ H ₆ ¹ G ₄ → ³ F ₄ ³ F ₃ → ³ H ₆	~345 ~475 ~646 ~700	980	16
	BaLaAlO ₄ :Yb ³⁺ , Tm ³⁺	¹ G ₄ → ³ H ₆ ¹ G ₄ → ³ F ₄ ³ H ₄ → ³ H ₆	~478 ~656 ~800	980	17
	NaYF ₄ :Yb ³⁺ /Ho ³⁺ /Tm ³⁺	¹ G _{4(1,2)} → ³ H ₆ ¹ G ₄ → ³ F ₄ ³ F _{2,3} → ³ H ₆	~474, 486 ~644 ~696	980	18

⁶ In Table 2, we summarize the characteristic optical properties of Er^{3+} , Ho^{3+} and Tm^{3+} ions incorporated in different phosphor materials.

2. Mechanisms of upconversion in lanthanide doped phosphors

The UC mechanisms that are widely adopted for lanthanide-doped phosphors are: excited state absorption (ESA), energy transfer upconversion (ETU), cooperative energy transfer (CET), photon avalanche (PA), and energy migration-mediated upconversion (EMU). These mechanisms have been discussed in detail in published review articles.^{3-8, 19} In all the above UC processes, the absorption of two-photon or multi-photons occurs sequentially. In general, the ESA and ETU processes have been mainly found in UC phosphors. Very few articles have reported PA and EMU mechanisms in UC materials.

The UC emissions in singly doped upconversion phosphors originate from ESA processes that involve sequential absorption of multi-photons. Large anti-stokes shifts are possible due to the availability of long-lived intermediate 4f energy levels in lanthanide ions which was hypothesized by Bloembergen *et al.*²⁰ and Dieke *et al.*²¹ around mid-20th century. **Figure 2a** represents a typical ESA process where successive photon absorption by a single ion and relaxation to the ground state resulted in upconversion luminescence (UCL). The ESA mechanism exists in UC phosphors with single activator ions such as Er^{3+} , Ho^{3+} , and Tm^{3+} . For example, UC emissions due to ESA were reported in $\text{ZnO}:\text{Er}^{3+}$ nanocrystals by Wang *et al.*²² and Ho^{3+} doped $\text{Na}(\text{Y},\text{Gd})\text{F}_4$ by Swieten *et al.*²³ However, the efficiency of UCL is not satisfactory for singly doped UC materials due to low molar-absorption coefficient of lanthanide ions. The Er^{3+} -based UC systems have been commonly reported to display ESA process which can be ascribed to the matching of energy gap between intermediate 4f energy levels matches with NIR photon energy.²⁴ Thus, a stepwise multi-photon absorption by Er^{3+} ions can populate the high energy emissive levels

which emit upconverted visible photons.

The ETU processes offer a better alternative to achieve high UCL efficacy by utilizing energy transfer (ET) between activator-sensitizer pairs in co-doped UC materials. In literature, different activator-sensitizer (A/S) pairs have been investigated to develop efficient upconverting systems. Usually, combinations such as $\text{Yb}^{3+}/\text{A}^{3+}$ ($\text{S} = \text{Yb}^{3+}$, and $\text{A} = \text{Er}, \text{Tm}, \text{Ho}, \text{Pr}$) $\text{Nd}^{3+}/\text{A}^{3+}$ ($\text{S} = \text{Nd}^{3+}$, and $\text{A} = \text{Er}, \text{Tm}, \text{Ho}$), and $\text{Yb}^{3+}/\text{Mn}^{2+}$ have been well explored for various applications. ETU processes are operated between two ions where the excitation energy of the sensitizer ion matches with the diode lasers (980 or 808 nm). **Figure 2b** represents the ETU process, where the sensitizer ion is excited to its metastable excited level under laser excitation in the first step. The sensitizer ion works as an antenna and has high NIR photon harvesting tendency. The contained energy is then transferred to the neighboring activator ions in the ground-state or the excited-state. The excitation of activator ions to the emissive state is then followed by relaxation to ground state by emitting higher energy photons. The ETU processes can be controlled by average distance between the A/S ions and thus, the efficiency vary with the dopant ions concentration.

Figure 2c represents a CET process operated between three ion centers, with two similar absorbing excitation photons and transferring energy to the excited state of the activator ion. The interaction between the three ions induced the cooperative ET and excited activator ion relaxes back to the ground states that result in the emission of upconverted photons. Liang *et al.* reported CET process in $\text{Yb}^{3+}/\text{Tb}^{3+}$ -codoped NaYF_4 nanocrystals²⁵ due to the absence of intermediate levels in Tb^{3+} ions to absorb NIR light. Pushkar *et al.*²⁶ Demonstrated the UC emissions in $\text{BaY}_2\text{F}_8:\text{Yb}^{3+},\text{Pr}^{3+}$ phosphor by CET mechanism. Unfortunately, the efficiency of CET processes is lower compared to ETU and ESA processes.³ This can be explained by the requirement of confined excitation for a CET process which makes it rigorous.

Chivian *et al.*²⁷ Firstly discovered a PA process in a Pr³⁺-based infrared quantum counter back in 1979. The PA process is illustrated in **Figure 2d**, where in the first step, the activator ions are pumped to excited states by weak absorption of the non-resonant NIR photon in the ground state. Further, the pumping of activator ions into upper emissive states is assisted by the resonant ETU/ESA processes. This is followed by a cross-relaxation (CR) type ET between the activator ions in the upper excited states and the sensitizer ions present in the ground state. Consequently, a continuous population in the intermediate excited energy levels of both the dopant ions occurs via a looping mechanism involving ESA/ETU and CR processes. As a result, the UCL intensity can be enhanced exponentially and thus, PA processes can be utilized to develop the highly efficient UC systems for cutting edge bio-applications.²⁸ Notably, the activator ion in a PA process is the same lanthanide ion as the sensitizer.²⁹ Only a few published works have

explored the PA mechanism for UCL generation and is not popular like ESA or ETU processes. Deng *et al.*³⁰ Reported the avalanche UC in LnVO₄ (Ln = Ce and Nd) nanocrystals (NCs) with large avalanche slope values (>15).

EMU process involves four different luminescent centers: sensitizer (S), accumulator (Ac), migrator (M), and activator (A), as presented in **Figure 2e**. The whole UC mechanism can be divided into four steps, that is, (i) initially the absorption of the NIR excitation energy by sensitizer ion, (ii) ETU process populate the higher excited level of accumulator ion, (iii) trapping of excitation energy by the migrator ion from the excited accumulator, and (iv) transfer of contained energy from the migrator to the activator ion which populate its excited states followed by UCL generation on relaxation to the ground level. The choice of migrator ion is crucial in the EMU process which decides the feasibility of ET between long distant ions. In 2011, Wang

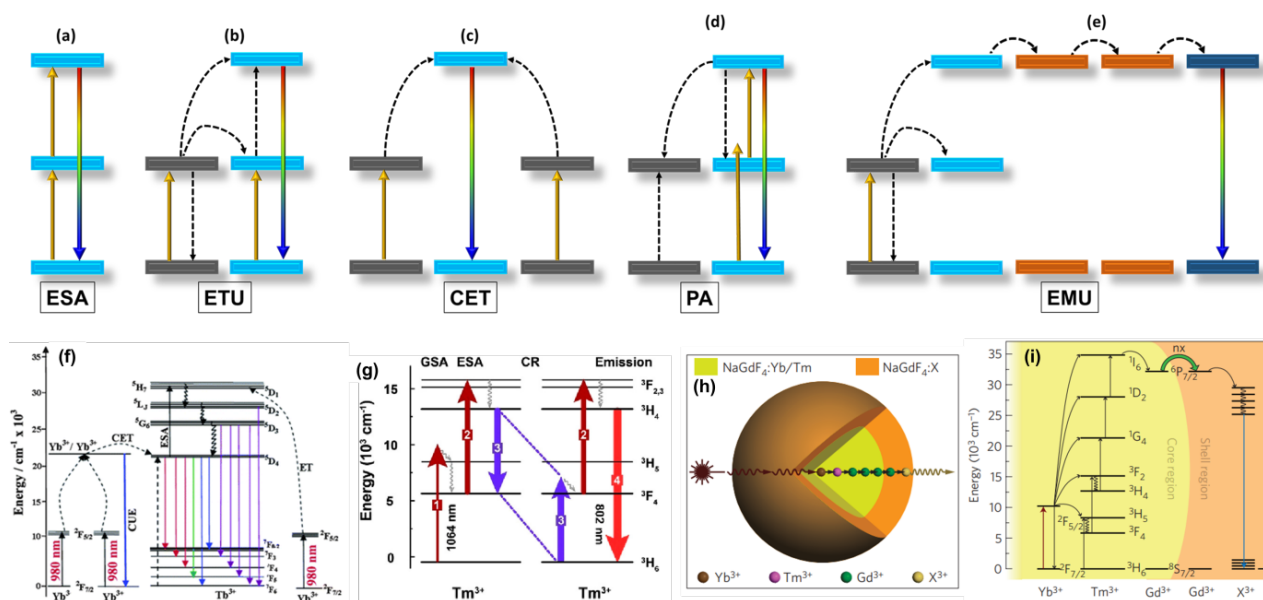


Figure 2: Schematic representations of UC mechanism of (a) ESA, (b) ETU, (c) CET (d) PA, and (e) EMU (upward, downward and dashed arrows represent the excitation, radiative emission processes and energy transfer processes, respectively). The different colored levels represents the different luminescent centers; (f) schematic representation of the partial energy levels and energy-transfer processes for Yb³⁺/Tb³⁺ up-conversion emission. CUE denotes cooperative up-conversion emission,³² (g) Schematic of energy levels and electronic transitions of Tm³⁺ for PA luminescence under 1064 nm excitation,³³ (h) schematic design of a lanthanide-doped NaGdF₄@NaGdF₄ core-shell nanoparticle for EMU (X: activator ion), and (i) proposed energy transfer mechanisms in the core-shell nanoparticle.⁶

et al. and co-workers⁶ proposed a novel ET route called as EMU in $\text{NaGdF}_4@\text{NaGdF}_4$ core-shell nanoparticles. The $\text{Yb}^{3+}/\text{Tm}^{3+}$ pair was adopted as S/Ac pair with the activator ion, A^{3+} ($\text{A} = \text{Tb}^{3+}, \text{Dy}^{3+}, \text{Eu}^{3+}$ and Sm^{3+}) doped into the core and shell layer, separately. The EMU process is particularly found to exist in core-shell structures. Most common migratory ions that have been explored are Yb^{3+} and Gd^{3+} .³¹ Future research on different combinations of other luminescent metal ions will further enlarge the scope of EMU based UC materials for bio-imaging and theranostic applications.

3. Synthesis of Lanthanide UCNPs

Upconversion nanoparticles (UCNPs) with size of <100 nm and good crystallinity have been promising for bio-imaging, PDT, PTT and theranostic applications. In recent years, various synthetic methods such as hydro (solvo) thermal, thermal decomposition, co-precipitation, sol-gel, microwave-assisted synthesis, and combustion methods have been employed for lanthanide doped UC inorganic materials in published articles. Extensive efforts have been made by the researchers to control the size, phases, morphology, and surface properties of Ln^{3+} -doped UCNPs. In this section, we will discuss different approaches used to synthesize the lanthanide UCNPs till date. The hydrothermal method has been commonly used for synthesizing highly monodisperse lanthanide UCNPs with size and shape control for potential applications. The method involves the dissolution of Ln^{3+} precursor salts (nitrates, acetates or chlorides) with other precursors into an appropriate solvent (water for hydrothermal synthesis). Usually, in case of fluoride-based host materials, NH_4F , HF , NH_4HF_2 , and NaBF_4 are used as a fluoride (F^-) precursors to synthesize REF_3 or RE-alkali metal double salts (MREF_4) UCNPs, while NaF/KF can be used for MREF_4 . A homogeneous solution is prepared by prolonged magnetic stirring or ultrasonication, which is then transferred to a Teflon-lined autoclave for heating under high temperature and pressure conditions.

In past, the synthesis of different hosts by simple hydro (solvo) thermal method with tunable morphologies has been summed up in several review articles. This method offers a convenient approach for the synthesis of nanoparticles with tunable size/shape by varying $\text{RE}^{3+}/\text{F}^-$ molar ratios, F^- precursor source, different temperatures, solvents, pH, addition of organic ligands/polymer such as cetyltrimethyl ammonium bromide (CTAB), citric acid, ethylene diamine tetra acetic acid (EDTA, oleyl amine, polyethylene glycol (PEG). The thermal decomposition method is the most applied and effective route for the synthesis of Ln^{3+} -doped UCNPs. Thermal decomposition involves dissolution of organometallic precursors in a high-boiling organic solvent with surfactants followed by the decomposition of the substance at high temperatures. The monodisperse nanoparticles are formed during the reaction via burst nucleation. In general, RE-organic compounds such as oleate, acetate, and trifluoroacetate are the metal-organic precursors. Commonly used high-boiling organic solvents are oleic acid (OA), oleylamine (OM), trioctylphosphine oxide (TOPO) and 1-octadecene (ODE). These contain long hydrocarbon chain which act as a functional capping group and is effective in preventing the aggregation of nanoparticles during the reaction. This method is atom-economical and can be employed to synthesize high-quality and uniform nanocrystals in different nm scale by optimizing the experimental parameters, such as concentration of metal precursors, reaction time and temperature, and the ratio of different solvents.

The co-precipitation method is effective for synthesizing ultra small UCNPs and their shape and size can be controlled by the experimental variables. In a few circumstances, it has been observed that crystalline nanoparticles can be made directly via co-precipitation synthesis, without the additional need for heat treatment. Coprecipitation is a widely used for preparation of core-shell based UCNPs for different bio-applications. A typical coprecipitation method for

core-shell rare earth fluorides involves reaction between metal oleate precursors and fluoride salts in oleic-octadecenoic (OA-ODE) acid solvent. Then, the growth of shell layers on the pre-synthesized core UCNPs used as seeds can be controlled by various experimental parameters. Though co-precipitation is time-consuming and laborious route, it offers control over shell composition and thickness via the modification of growth kinetics. However, UCNPs obtained from coprecipitation method have a wide size distribution (from nm to μm). In some cases, subsequent annealing of as-prepared UCNPs was required to improve the crystallinity and UCL properties.

Some researchers have applied different synthetic techniques such as sol-gel, micro-emulsion, combustion synthesis, and microwave-assisted synthesis for developing high-quality UCNPs. In a typical sol-gel process, the hydrolysis of metal alkoxide (or halide) precursors results in the polycondensation and formation of gel. The calcination of dried gel at high temperatures is required to produce crystalline nanoparticles. However, a wide particle size distribution of UCNPs by sol-gel method is not desirable for bio-application.

Microwave-assisted heating approach for UCNPs is still in the developing stage and further optimization of synthetic conditions will help in controlling UCL properties. The method involves the exposure of reactants to electromagnetic waves which produce heating of solutions in a very short time span. Therefore, microwave-assisted strategy is green synthesis with low energy consumption and requires less reaction time. Microemulsion synthesis involves the formation of

aggregated forms such as micelles or vesicles from the surfactants and precursors which function as a microreactor. This template synthesis produces NPs with size in the nm scale and control over morphology can be achieved by the presence of surfactants. But calcination is usually required to improve quality of UCNPs which may induce aggregation of NPs. This approach is effective for fabrication of UCNPs surface and their self-assembly.

4. Few Case Studies of efficient and tunable UC in inorganic oxides and applications

Both up and down convertible luminescence (UC and DC) are known in lanthanide-based phosphors depending on the choice of lanthanide ions. In UC, multiple low energy photons used in excitation are emitted as high energy photon while in down conversion process, low energy photons are emitted than those used for excitation. DC and UC hence follow Stoke's and Anti Stoke's process respectively. **Figure 3** shows the schematic of both UC and DCL process using NIR excitation employing core-shell strategy with Yb^{3+} rich core and $\text{Yb}^{3+}/\text{Er}^{3+}$ co-doped nanoparticles in shell. Such nanoparticles if tagged properly with suitable biomolecules have

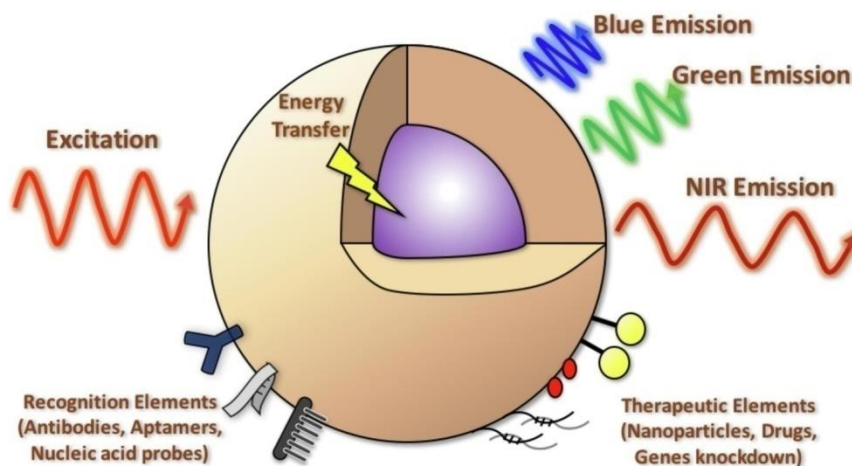


Figure 3: Schematic showing UC and DC both in Yb^{3+} and Er^{3+} co-doped core shell nanoparticles. Yellow covering represents Yb^{3+} rich shell absorbing NIR photon and transferring the energy to $\text{Er}^{3+}/\text{Yb}^{3+}$ co-doped core (represented by purple color) leading to UC blue, green, and red emissions, or DC NIR emissions, respectively. The lower part shows that tagging with suitable biomolecules may help in achieving bio-photonics and nanomedicine applications.¹⁹

an advantage in application such as bio-photonics and biomedicine. Our group has explored have explored Yb³⁺ sensitized and Tm³⁺, Er³⁺ and Ho³⁺ doping upconversion in LaF₃, La₂Zr₂O₇, Gd₂Hf₂O₇, ZnGa₂O₄, ZnAl₂O₄, etc.³⁴⁻⁴¹

Ln³⁺-based upconversion (UC) phosphors are promising for highly sensitive and non-contact optical thermometry based on temperature sensitive luminescence intensity ratios (LIR) of thermally/non-thermally coupled energy levels. LIR based optical thermometry is a promising field for contactless temperature measurement unique properties such as fast response time, non-invasiveness, contactless measurement, anti-interference ability, good temperature resistance and temperature resolution precision. Spinel exhibits optical, catalytic, magnetic and electrical properties which lead to applications in many areas such as optoelectronic devices, electronic industries, laser devices, supercapacitors, metal-ion batteries etc. However, the investigations on the use of optical thermometers in cryogenic temperature range below 300 K are rarely reported and usually display low absolute sensitivities of 10⁻³ order below room temperatures. In this work, we utilized the codoping of Mn²⁺ ions in ZnAl₂O₄:Ho³⁺/Yb³⁺ upconversion phosphor to initiate extra energy transfer pathways and investigated the temperature dependent luminescent properties from 80 to 300 K. The energy transfer between Mn²⁺ - Ho³⁺ is also effective in achieving singular red UC emissions that improves the overall bioimaging sensitivity for optical imaging. Color tunability from red to green domain on higher temperature annealing display the potential of our phosphor as a luminescence switch. The laser power dependencies and lifetime studies were performed to gain more insights into the energy transfer (ET) processes. Interestingly, we observed a complete swap in the emission properties at 80 K and 300 K in ZnAl₂O₄:Ho³⁺/Yb³⁺ due to coexisting temperature sensitive multi-phonon relaxations and non-radiative decay routes. The incorporation of Mn²⁺ turned

to be a boon for this system as Ho³⁺-Mn²⁺ ET is also temperature dependent and competes with other ET and non-radiative routes to modulate the UC emissions effectively. The codoping of Mn²⁺ ions improved the maximum absolute (S_a) and relative sensitivity (S_r) along with impressive color shift from green to red on going from 80 to 300 K which can be utilized for temperature approximation by naked eyes. The effective color tunable thermometers and a high S_a obtained in this work even at 80 K are demonstrated by limited Ln³⁺ based materials. Since cryogenic applications involves fields like bio-medical, space technology, electronics and agriculture, this study will be beneficial to design new cryogenic thermometers by judiciously altering the ET and other non-radiative channels responsible for populating excited levels. In addition, the single red component emission and paramagnetic properties of this phosphor can be explored for bimodal imaging. In another work we demonstrate the tailoring of luminescence properties via introducing Ho³⁺ - Mn²⁺ energy transfer (ET) routes with judicious codoping of Mn²⁺ ions in ZnAl₂O₄:Ho³⁺,Yb³⁺ phosphor (**Figure 4**).³⁵ Higher temperature annealing brings the color coordinates to green domain highlighting the potential for color tunable luminescence switch (**Figure 4**). Moreover, this work investigates the thermometric properties of ZnAl₂O₄:Yb³⁺, Ho³⁺ in the range of 80-300 K and influence of inducing extra ET pathways by Mn²⁺ codoping. The codoping of Mn²⁺ ions is fruitful in fourfold increase of absolute sensitivity and notably the color tunability from green through yellow to red is helpful in rough temperature estimation by naked eyes. The maximum relative (S_r) and absolute sensitivities (S_a) were estimated to be 1.89% K⁻¹ (140 K) and 0.0734 K⁻¹ (300 K), respectively (**Figure 4**). Even at 80 K, S_a of 0.00447 K⁻¹ and S_r of 0.6025% K⁻¹ were achievable in our case which is higher than most of the other Ln³⁺-based systems.

ZnAl₂O₄ and ZnGa₂O₄ based spinel material having shown exceptional performance in the

area of luminescence owing to their exceptional photophysical characteristics. Color tunable phosphors (CTPs) have demonstrated tremendous potential in recent years owing to their application in the various areas such as temperature sensors, field emission displays (FEDs), light emitting diodes (LEDs) and plasma display panels

(PDPs). Hence, there is a continuous effort being vested among scientific community for search towards efficient CTPs. Under NIR excitation $ZnAl_{2-x}Ga_xO_4: Er, Yb$ phosphors depicted UCL in green and red region and down conversion in NIR-II region.⁴⁰ Gallium insertion gradually leads to beautiful color tunability from pure red

in $ZnAl_2O_4: Er, Yb$ to orange and yellow and in between solid solution and then finally to green in $ZnGa_2O_4: Er, Yb$ (Figure 5). The maximum absolute sensitivity is found to be $11.10 \times 10^{-3} K^{-1}$ at 302 K whereas the relative sensitivity is $5.02 \times 10^{-3} K^{-1}$ at 302 K indicating the applicability of $ZnGa_2O_4: Er, Yb$ as a optical temperature sensor in the temperature range 302-473 K (Figure 5).

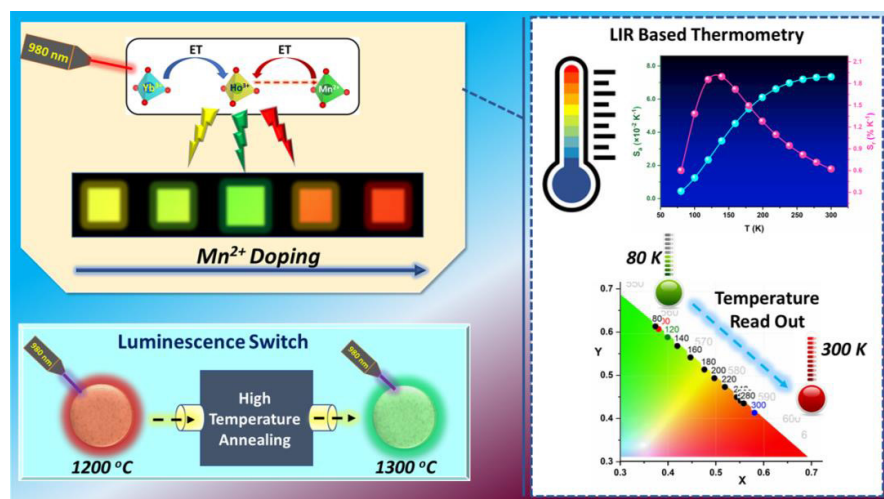


Figure 4: Enhanced Energy transfer channels in $Mn^{2+}/Ho^{3+}/Yb^{3+}$ Tri-doped $ZnAl_2O_4$ Nanophosphors leading to multifaceted application of upconvertible materials towards luminescence switching and cryogenic thermometry.³⁵

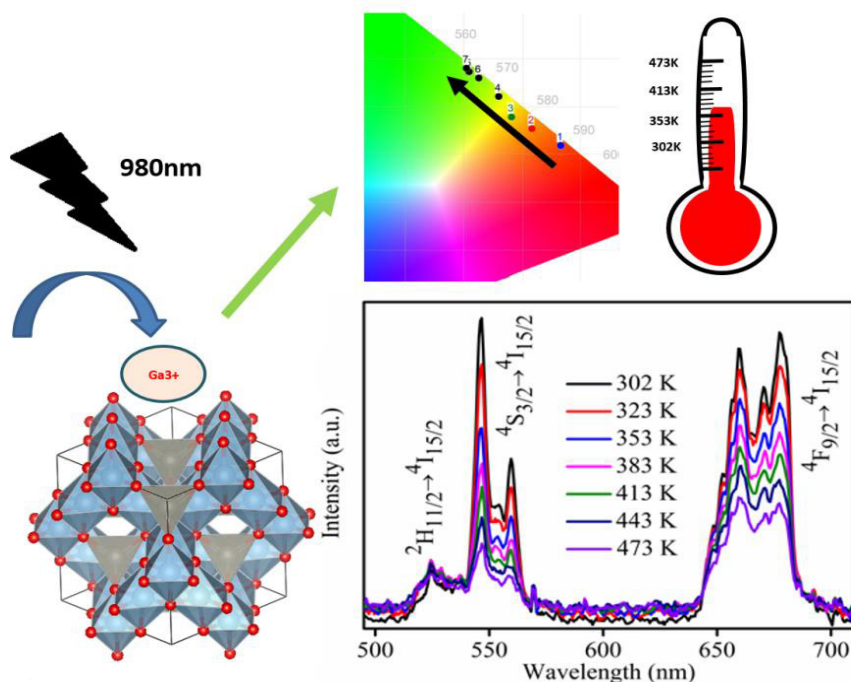


Figure 5: Color tunable phosphor triggered by compositional modulation in Al/Ga ratio and laser power along with feasibility for non-contact optical thermometry.⁴⁰

In recent years, the scientists are keenly interested in developing the multifunctional lanthanide doped upconversion (UC) materials to solve the urgent problems like diagnosis and treatment of cancer. Photothermal therapy (PTT) is a less-invasive treatment of cancer and is arousing tremendous attention over the traditional chemotherapy. The research on lanthanide doped upconversion (UC) materials have revealed their remarkable ability for advanced biomedical and theranostic applications due to strong NIR absorption and upconversion efficacies and NIR excitations have low photo-toxicity and low autofluorescence

background. Thus, in our recent work, we have developed a promising $\text{ZnAl}_2\text{O}_4:\text{Ho}^{3+}/\text{Yb}^{3+}$ UC phosphor and demonstrated its potential for optical imaging, theranostic and anti-cancer therapy and is not reported so far to the best of our knowledge. To be noteworthy, $\text{ZnAl}_2\text{O}_4:\text{Ho}^{3+}/\text{Yb}^{3+}$ UC phosphor showed strong upconversion in both ultraviolet-C (UVC) and visible region as well as downconversion (DC) to NIR-II region and thus, can be well utilized for diverse bioapplications. Benefitting from these excellent photophysical properties of $\text{ZnAl}_2\text{O}_4:\text{Ho}^{3+}/\text{Yb}^{3+}/\text{Na}^+$ UC phosphor, we performed in vitro studies with fibroblast cells and rat C6 glioma cells and impressively, our UC material showed excellent biocompatibility and efficient photothermal effect in NIR laser irradiation and rapid increase in temperature higher than 42°C required for killing of cancer cells in a time span of 10 min which is considerably good as per reported photothermal agents.⁴² As ^{166}Ho is a promising therapeutic radioisotope, we carried out preclinical studies with intrinsically radiolabeled $\text{ZnAl}_2\text{O}_4:^{166}\text{Ho}^{3+}/\text{Yb}^{3+}/\text{Na}^+$ UC

phosphor for theranostic applications for the first time via in vivo SPECT/CT imaging in healthy Wistar rats that proposed the potential of our UC material for image-guided theranostic therapy. In addition, intense germicidal UVC UC emission demonstrated by $\text{ZnAl}_2\text{O}_4:\text{Ho}^{3+}/\text{Yb}^{3+}$ UC phosphor is suitable for disinfection and further broadens its application field's particularly pandemic times like COVID-19. We strongly believe that our work contributes in the development of UC materials and put forward a great application prospect regarding sustainable biological imaging and cancer therapy. Na^+ co-doped $\text{ZnAl}_2\text{O}_4:\text{Ho}^{3+}, \text{Yb}^{3+}$ upconversion nanoparticles (UCNPs) with remarkably enhanced upconversion luminescence (UCL) have demonstrated good cellular uptake, bio/cyto compatibility and anticancer efficacy in C6 glioma cells (Figure 6).³⁴ The % cell viability of C6 cells exposed to UCNPs decreased to 46% under 980 nm near infrared light laser exhibiting excellent photothermal therapy (PTT) by the material. The Na^+ ions codoping resulted in a significant lowering of

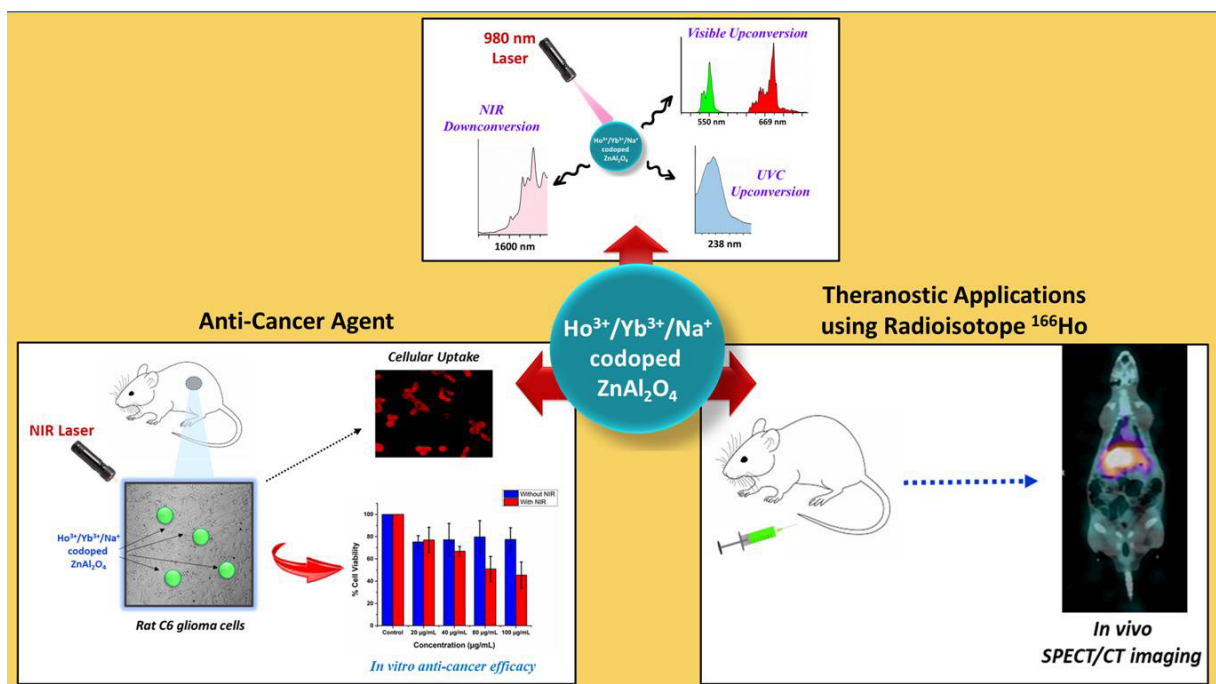


Figure 6: Remarkable enhancement in UVC and visible upconversion from $\text{ZnAl}_2\text{O}_4:\text{Yb}^{3+}, \text{Ho}^{3+}$ on Na^+ doping and its efficacy towards cancer treatment and radiolabeling agent for theranostic purpose.³⁴

zinc vacancies in $\text{ZnAl}_2\text{O}_4:\text{Ho}^{3+}, \text{Yb}^{3+}$ indicating its effective role in eliminating defect-induced non-radiative channels. Intrinsically (166-Holmium) radiolabeled $\text{ZnAl}_2\text{O}_4:\text{Yb}^{3+}, ^{166}\text{Ho}^{3+}, \text{Na}^+$ have also shown great potential towards *in vivo* single-photon emission computed tomography (SPECT) imaging (**Figure 6**).

Lanthanide (Ln^{3+}) and $\text{Yb}^{3+}/\text{Ln}^{3+}$ doped upconversion nanomaterials (UCNPs) have been extensively explored for diverse applications such as non-contact thermometry, solar cells, and bio-medicine. But improving the upconversion (UC) efficiency is a major challenge. One of the promising strategies for enhancing UC luminescence is by generating asymmetric coordination around emitter Ln^{3+} ions by co-doping of non- Ln^{3+} ions into host lattice. Owing to application of cryogenic temperature measurements in aerospace industries, metallurgy, engineering, manufacturing and basic sciences, etc. their precise and fast determination is very important.

In past, various alkali and transition metals ions have been explored as dopants to alter the symmetry around Er^{3+} ions. However, still in-depth investigations are missing for the co-doping effects of higher valent dopants. Th^{4+} is a higher valent ion than Ln^{3+} ions, and in recent years, various publications availed the advantage of Th^{4+} doping for diverse applications such as electrocatalysis, photocatalysis, and superconductors. Much to our surprise, there is not a single report on improved UC luminescence by Th^{4+} addition.

To address the above issues, tetravalent Th^{4+} co-doped $\text{YF}_3:\text{Yb}^{3+}, \text{Er}^{3+}$ nanorods were synthesized and its upconversion luminescence were explored.⁴³ The changes in Y-F and Er-F bond lengths in $\text{Yb}^{3+}/\text{Ln}^{3+}$ and $\text{Yb}^{3+}/\text{Er}^{3+}/\text{Th}^{4+}$ co-doped YF_3 systems were analyzed using DFT calculations for understanding the role of Th^{4+} co-dopants in inducing local structure distortions around Er^{3+} ions. The more asymmetric Er-F bond lengths and low symmetry Y^{3+} sites on co-doping Th^{4+} in $\text{Yb}^{3+}/\text{Er}^{3+}$ co-doped YF_3 were revealed by

the DFT results and validated the enhancement in UC emissions due to relaxation in selection rules of 4f-4f transitions of Er^{3+} ions. Moreover, we have investigated the potential of co-doped YF_3 UC nanorods for cryogenic thermal sensing. Cryogenic thermometers are rarely reported with only low sensitivities of 10^{-3} order below -70°C . Thus, we utilized various stark sub-levels having a distinct temperature-responsive intensity trend, and investigated the temperature-dependent luminescence intensity ratio (LIR) from 80 to 300 K. Benefiting from this, we have proposed an approach of using multiple luminescence intensity ratios (LIR) based thermometry involving non-thermally coupled energy levels (NTCELS). It was fruitful in achieving a more accurate temperature read-out with relative sensitivity (S_r) values $>0.4\% \text{K}^{-1}$, especially at cryogenic temperatures below -33°C (up to -193°C). While most of the reports either used TCLs or NTCELS based single LIR for temperature sensing that resulted in low S_r values at some temperature zones, in our case, the low S_r values in different temperature zones for one LIR are re-compensated by other LIRs having higher sensitivity in the same zones.

Both UC and DC was also achieved in $\text{La}_2\text{Zr}_2\text{O}_7$ pyrochlore oxide nanoparticles (not core-shell) by judicious choice of dopant and co-dopant (**Figure 8**).³⁹ The mechanism of

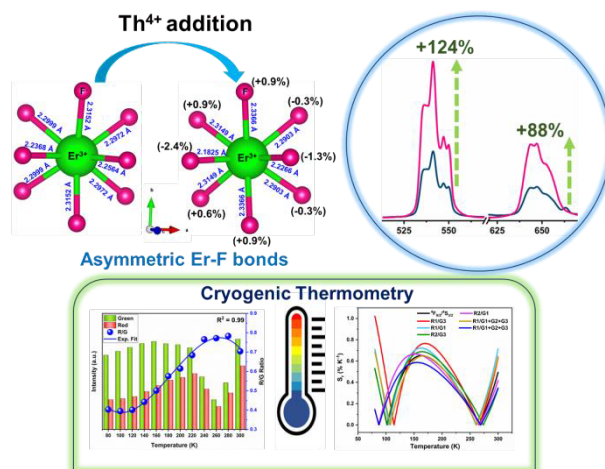


Figure 7: Improved luminescence in Th^{4+} co-doped $\text{YF}_3:\text{Yb}^{3+}, \text{Er}^{3+}$ nanorods for cryogenic thermometry⁴³

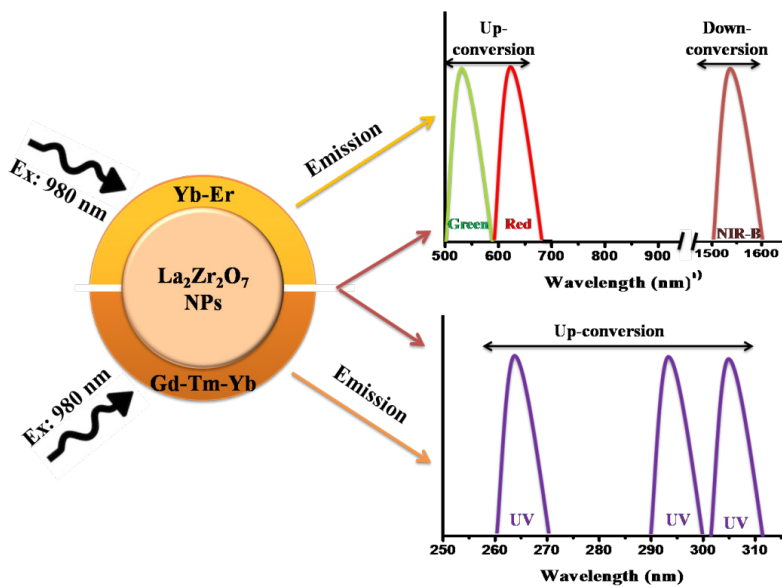


Figure 8: Schematic NIR to Visible and UV UC and NIR-A to NIR-B DC in single $\text{La}_2\text{Zr}_2\text{O}_7$ pyrochlore oxide nanoparticle-based phosphor.³⁹

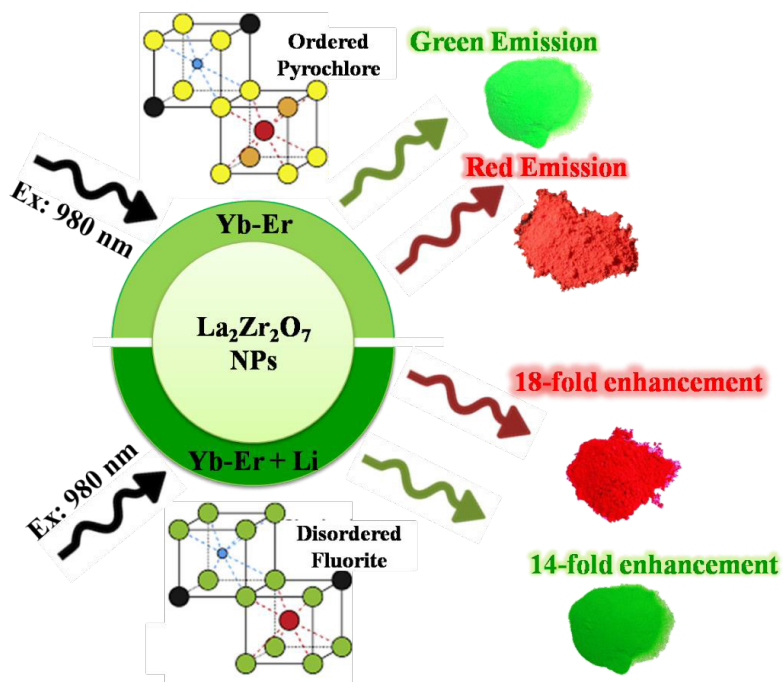


Figure 9: Schematic showing significant UC intensity enhancement in $\text{La}_2\text{Zr}_2\text{O}_7$ pyrochlore oxide nanoparticle-based phosphor induced by lithium co-doping assisted order-disorder phase transition.³⁷

energy transfer is discussed in detail in this article itself. Infact, dual UC; NIR to visible as well as NIR to UV were observed. It was also found that UC intensity can be enhanced substantially by inculcating symmetry lowering which was successfully achieved by lithium co-doped structural phase transition from ordered pyrochlore to disordered fluorite structure in $\text{La}_2\text{Zr}_2\text{O}_7$ pyrochlore oxide nanoparticles (Figure 9).³⁷

The potential of RE doped oxide nanoparticles are further elaborated in generating singular emission which is highly desirable for bioimaging applications. Only issue with Er/Yb based UC is, it always gives a mixture of red and green emissions. Biological tissues show low absorption in the red (600-700 nm) and near infrared (NIR, 700-1100 nm) region. Hence, this region of spectrum has large penetration depth in the tissues and considered ideal in bioimaging. However, the green emission from this Yb/Er combination is undesired due to its high absorption with potential of causing damage to cell/tissues. In most cases red/green ratio in $\text{Er}^{3+}/\text{Yb}^{3+}$ combination is modified by altering the ratio of dopant ions or optimizing the annealing condition. But complete prevention of green emission proved exceedingly difficult. Most of the reported literatures have produced singular red emission in UC phosphor by co-doping Mn^{2+} in $\text{Er}^{3+}/\text{Yb}^{3+}$ combination or by using Mn^{2+} consisting host such as MnF_2 , NaMnF_3 etc. Manganese, owing to multiple oxidation sates, disturbs

14. Pandey, A.; Rai, V. K., *Dalton Transactions* **2013**, 42, (30), 11005-11011.
15. Sheng, C.; Li, X.; Tian, Y.; Wang, X.; Xu, S.; Yu, H.; Cao, Y.; Chen, B., *Spectrochimica Acta Part A: Molecular and Biomolecular Spectroscopy* **2021**, 244, 118846.
16. Meng, M.; Zhang, T.; Wang, J.; Cheng, Z.; Liu, Y.; Qiao, X.; Wen, J.; Resch-Genger, U.; Long, W.; Ou, J., *ACS Applied Nano Materials* **2022**, 6, (1), 759-771.
17. Etafo, N.; Oliva, J.; Garcia, C.; Mtz-Enrriquez, A.; Ruiz, J.; Avalos-Belmontes, F.; Lopez-Badillo, C.; Gomez-Solis, C., *Inorganic Chemistry Communications* **2022**, 137, 109192.
18. Cheng, Z.; Meng, M.; Wang, J.; Li, Z.; He, J.; Liang, H.; Qiao, X.; Liu, Y.; Ou, J., *Nanoscale* **2023**.
19. Loo, J. F.-C.; Chien, Y.-H.; Yin, F.; Kong, S.-K.; Ho, H.-P.; Yong, K.-T., *Coordination Chemistry Reviews* **2019**, 400, 213042.
20. Bloembergen, N., *Physical Review Letters* **1959**, 2, (3), 84.
21. Dieke, G. H.; Crosswhite, H., *Applied optics* **1963**, 2, (7), 675-686.
22. Wang, X.; Kong, X.; Yu, Y.; Sun, Y.; Zhang, H., *The Journal of Physical Chemistry C* **2007**, 111, (41), 15119-15124.
23. van Swieten, T. P.; Yu, D.; Yu, T.; Vonk, S. J.; Suta, M.; Zhang, Q.; Meijerink, A.; Rabouw, F. T., *Advanced Optical Materials* **2021**, 9, (1), 2001518.
24. Zheng, X.; Kankala, R. K.; Liu, C.-G.; Wang, S.-B.; Chen, A.-Z.; Zhang, Y., *Coordination Chemistry Reviews* **2021**, 438, 213870.
25. Liang, H.; Chen, G.; Li, L.; Liu, Y.; Qin, F.; Zhang, Z., *Optics communications* **2009**, 282, (14), 3028-3031.
26. Pushkar', A.; Uvarova, T.; Kiiko, V., *Optics and Spectroscopy* **2011**, 111, 273-276.
27. Chivian, J. S.; Case, W.; Eden, D., *Applied Physics Letters* **1979**, 35, (2), 124-125.
28. Joubert, M.-F., *Optical Materials* **1999**, 11, (2-3), 181-203.
29. Cheng, X.; Zhou, J.; Yue, J.; Wei, Y.; Gao, C.; Xie, X.; Huang, L., *Chemical Reviews* **2022**, 122, (21), 15998-16050.
30. Deng, H.; Yang, S.; Xiao, S.; Gong, H.-M.; Wang, Q.-Q., *C. Journal of the American Chemical Society* **2008**, 130, (6), 2032-2040.
31. Su, Q.; Han, S.; Xie, X.; Zhu, H.; Chen, H.; Chen, C.-K.; Liu, R.-S.; Chen, X.; Wang, F.; Liu, X., *Journal of the American Chemical Society* **2012**, 134, (51), 20849-20857.
32. Debasu, M. L.; Ananias, D.; Pinho, S. L.; Geraldes, C. F.; Carlos, L. D.; Rocha, J., *Nanoscale* **2012**, 4, (16), 5154-5162.
33. Zhang, M.; Huang, P.; Zheng, W.; Song, X.; Shang, X.; Zhang, W.; Yang, D.; Yi, X.; Chen, X., Lanthanide-Doped KMgF_3 Upconversion Nanoparticles for Photon Avalanche Luminescence with Giant Nonlinearities. *Nano Letters* **2023**.
34. Balhara, A.; Gupta, S. K.; Aggarwal, N.; Srivastava, S.; Panda, J. J.; Patra, S.; Chakraborty, A.; Rakshit, S.; Chakravarty, R., Remarkably Enhanced Upconversion Luminescence in Na^+ Co-doped Spinel Nanoparticles for Photothermal Cancer Therapy and SPECT Imaging. *Materials Advances* **2023**.
35. Balhara, A.; Gupta, S. K.; Debnath, A. K.; Sudarshan, K., Utilizing Energy Transfer in $\text{Mn}^{2+}/\text{Ho}^{3+}/\text{Yb}^{3+}$ Tri-doped ZnAl_2O_4 Nanophosphors for Tunable Luminescence and Highly Sensitive Visual Cryogenic Thermometry. *ACS omega* **2023**, 8, (33), 30459-30473.
36. Bose, S.; Summers, J. R.; Srivastava, B. B.; Padilla-Gainza, V.; Peredo, M.; De Leo, C. M. T.; Hoke, B.; Gupta, S. K.; Lozano, K., Efficient near infrared to visible light upconversion from Er/Yb codoped PVDF fibrous mats synthesized using a direct polymer doping technique. *Optical Materials* **2022**, 123, 111866.
37. Gupta, S. K.; Abdou, M.; Zuniga, J. P.; Ghosh, P. S.; Mao, Y., Li^+ co-doping induced phase transition as an efficient strategy to enhance upconversion of $\text{La}_2\text{Zr}_2\text{O}_7:\text{Er},\text{Yb}$ nanoparticles. *Journal of Luminescence* **2020**, 224, 117312.
38. Gupta, S. K.; Garcia, M. A. P.; Mao, Y., Ultraviolet, blue and singular green upconversion from $\text{Gd}_2\text{Hf}_2\text{O}_7$ nanocrystals through dopant manipulation. *Solid State Communications* **2021**, 338, 114458.
39. Gupta, S. K.; Penilla Garcia, M. A.; Zuniga, J. P.; Abdou, M.; Mao, Y., Visible and ultraviolet upconversion and near infrared downconversion luminescence from lanthanide doped $\text{La}_2\text{Zr}_2\text{O}_7$ nanoparticles. *Journal of Luminescence* **2019**, 214, 116591.
40. Parayil, R. T.; Gupta, S. K.; Upadhyay, M. M.; Sudarshan, K.; Mohapatra, M., Tunable Upconversion in $\text{ZnAl}_2\text{O}_4:\text{Er},\text{Yb}$ Phosphors by Modulating Al/Ga Ratio and Application in Optical Thermometry. *New Journal of Chemistry* **2023**.
41. Srivastava, B. B.; Gupta, S. K.; Mao, Y., Single red emission from upconverting $\text{ZnGa}_2\text{O}_4:\text{Yb},\text{Er}$ nanoparticles co-doped by Cr^{3+} . *Journal of Materials Chemistry C* **2020**, 8, (19), 6370-6379.
42. Du, K.; Lei, P.; Dong, L.; Zhang, M.; Gao, X.; Yao, S.; Feng, J.; Zhang, H., In situ decorating of ultrasmall Ag_2Se on upconversion nanoparticles as novel nanotheranostic agent for multimodal imaging-guided cancer photothermal therapy. *Applied Materials Today* **2020**, 18, 100497.
43. Balhara, A.; Gupta, S. K.; Modak, B.; Nanda, S. S.; Dash, S.; Sudarshan, K.; Acharya, R., Th^{4+} Co-doped $\text{YF}_3:\text{Yb}^{3+}, \text{Er}^{3+}$ Nanostructures for Enhanced Visible and NIR-II Emissions and Potential Application as Cryogenic Thermometer. *ChemPhotoChem* n/a, (n/a), e202300125.



Ms. Annu is currently a 3rd year PhD student at the Radiochemistry Division, Bhabha Atomic Research Centre in Mumbai. She obtained M.Sc in Chemistry from the Indian Institute of Technology, Roorkee (IITR) in India. Her research interests include developing of multifunctional luminescent materials for various applications such as solid-state lighting, thermometry, and biomedical applications. As of today, she has published more than 10 peer reviewed international journal and presented her work in several national symposiums.



Dr. Santosh Kumar Gupta joined the 53rd batch of BARC Training School and subsequently joined the Radiochemistry Division in 2010. Dr. Gupta is the recipient of several awards notable among them are Fulbright, Indo-US and JSPS Fellowship, DAE and Scientific India Young Scientist award, IANCAS Tarun Datta Memorial Medal, Society of Materials Chemistry Bronze medal, Fulbright OLF Award and Chirantan Rasayan sanstha (CRS) silver medal. He has also been bestowed with membership of Indian national young academy of sciences (INSA-INYAS) & National academy of sciences (NASc) and young associate of Maharashtra academy of sciences (MASc). He has been elected as Fellow of the Royal Society of Chemistry (FRSC), Fellow of the Indian Chemical Society (FICS) and Fellow of the Maharashtra Academy of Sciences (FMASc) for the year 2023. He has received Royal Society of Chemistry certificate for among 10 % most cited author and ICDD certificate for contribution of new XRD pattern. He was featured in Top 2% most Influential scientists worldwide based on the Scopus publications impact consecutively for the year 2020, 2021 and 2022 prepared by Prof. John PA Loannidis of Stanford University and his team and published by Elsevier. As of today, he has published more than 235 peer reviewed international journal articles with around 5900 citations and an **h-index** of 46 and **i-10** index of 136. His area research focuses on designing light emitting materials for health, energy and environment etc.

Engineered 3D Composite based Electrodes for Efficient Catalysis

Indra Sulania^{1,3*}, Ambuj Tripathi¹, Ranjeet K Karn², Elham Chamanehpour³,
Ajani Lakmini Jayarathna^{3,4} and Y K Mishra^{3*}

¹Inter University Accelerator Centre, Materials Science Group, New Delhi 110067, India

²Department of Physics, Kolhan University, Chaibasa, 833201, India

³Mads Clausen Institute, NanoSYD, University of Southern Denmark, Alsion 6400, Denmark

⁴Sirindhorn International Institute of Technology, Thammasat University, Rangsit 12120, Thailand

Corresponding author: *Email: indra@iuac.res.in and mishra@mci.sdu.dk

Abstract

Zinc oxide tetrapods (ZNT) based thick films were synthesized with different concentration of ZNT dissolved in Polyethylene Glycol (PEG) solution through chemical routes. Synthesized solution was probe sonicated and spin coated on Glass and ITO substrates followed by characteristic analysis using SEM with EDX, FTIR and UV Vis. spectrophotometer. SEM images shows the composite formation of ZNT with PEG with their legs intact, thus forming catalysis electrode 3D network. FTIR shows the functional groups bond energies for the synthesized samples. Further, photodegradation of methylene blue dye was performed with the synthesized samples as both the materials are UV sensitive. The photodegradation rate was found to improve in the presence of composite sample due to efficient charge separation and found to be promising alternative for wastewater treatment and thus, environmental remediation. The sample would be treated with energetic ions for the enhancement in the properties further.

Keywords: ZnO tetrapods, Photocatalyst, Polymer composite, SEM, FTIR spectroscopy.

1. Introduction

With increasing pollutants in the water bodies, due to untreated wastewater being thrown into the natural sources of water from the textiles industries and households, problem of increasing wastewater has become severe with each day passing by. This continuously endangers human health and natural environment [1]. Since decades, several conventional methods such as sedimentation, filtration through chemical and membrane technologies have been used to eliminate degradation-resistant pollutants such as harmful dyes or hazardous chemicals [2-4]. As advances to tackle this challenge, photocatalytic techniques have drawn much attention due to their high efficiency and low toxicity in decomposing organic contaminants under light exposure, thus provides green and eco-friendly solutions [4]. Several photocatalysts such as CdS, TiO₂, Fe₂O₃, ZnO, SnO₂ and many

more, have been widely studied for wastewater treatment [5-7], however, few catalysts like TiO₂ show limited efficiency due to its wider bandgap² and higher electron-hole recombination [5], generally, such photocatalysts work in the range of ultraviolet light thus, making them less user friendly [6]. Therefore, it is extremely important to develop highly efficient visible-light-driven photocatalysts for the degradation of organic chemical pollutants.

In addition, it is well known that powders of photocatalyst are usually used during wastewater purification process, but it is hard to recollect these powders from the treated waters and thus, they themselves become a contamination in the due course of process in the water bodies. Therefore, thicker films or self-standing films of photocatalyst shows higher scopes and efficiency for practical wastewater treatment process, moreover, the stability of

films usually affects photocatalytic efficiency [3]. Consequently, the development of stable and highly efficient photocatalytic materials is in much demand to meet present challenges. Several studies have shown that composite materials may serve as better catalysts by improving the charge separation and transfer in the wider absorption region. Zinc oxide (ZnO) and titanium dioxide (TiO₂) are wide bandgap semiconductors and may function as photocatalysts [5, 6]. Especially, ZnO semiconducting electrodes are widely investigated for application in dye-sensitized solar cells because they exhibit a high bulk electron mobility [6, 8]. With wide band gap of ~3.37 eV, it has a large exciton binding energy of ~60 meV. It has gained a lot of interest because of advances in synthesis techniques in achieving the hierarchical shapes as per [9] specific applications such as photocatalysis due to its high photosensitivity and stability. Polyethylene Glycol (PEG) is a pore-forming agent, which occupy space in the agglomerated materials such as ZnO, thus, may be used to modify properties of various photocatalysts to affect the shape, size and crystal structure. Few reports suggests that due to different molecular weight of PEG,

the size of nanoparticle may be manipulated for proper growth of the photocatalyst material which help in improving the catalytic actions in a better way [4][10-12]. Y K Mishra *et al.* [13] have grown unique 3-dimensional ZnO structure in the form of a tetrapod (ZNT) where each of the legs are structured 105° from each other. They have been utilized for multifunctional properties and applications [14]. Therefore, it is evident that polymer composite of PEG with ZNT may act as an efficient catalysis material thus, in the present study, thicker films of PEG with 2.5% ZNT have been formed on different substrates by chemical routes and characterized for their morphological, optical and structural properties. Their performance has been recorded as a catalyst material for the organic Azo dye degradation. Such materials/electrodes have more potential than the conventional powders used for catalysis due to higher efficiency and bio-degradable for wastewater treatment thus, in environmental remediation.

1. Materials and Methods

A pure Polyethylene Glycol (PEG) polymer solution Hybri-Max™ was procured from Sigma-

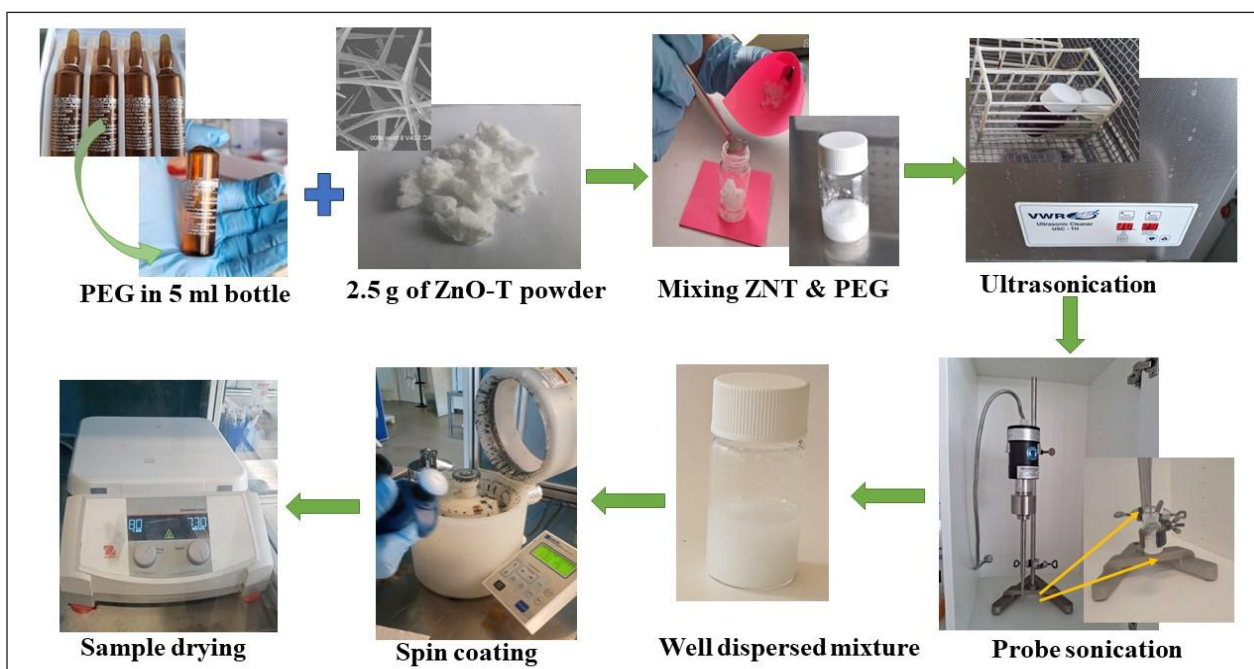


Figure 1: Schematic representation of synthesis of ZNT+PEG composite sample

Aldrich. The powder of ZnO Tetrapods (ZNT) was synthesized using Flame Transport Synthesis (FTS) technique in the laboratory using the powders of Polyvinyl Butyral (PVB) and Zn taken in the appropriate ratio.

The schematic view of the steps followed to form composite of (PEG+ZNT) is presented in figure 1. The details for the optimization of the synthesis technique for ZNT is discussed elsewhere [13, 14]. Solution of PEG polymer with ZNT powder was prepared in a glass bottle and ultra sonicated for 30 minutes and probe sonicated for 30 seconds at 50W power to form a uniform solution. The sonicated solution was drop casted on different substrates (Si, ITO coated glass and CaF₂) with a 20 microliters pipette and further, spin coated at 1000 rpm for ~5 to 10 layers to form a thick layer of the composite and then dried on a heater plate at 110°C for 30 minutes. Their morphologies, composition was analyzed with Scanning electron Microscope (SEM) from Hitachi at an electron energy of 5keV with EDX performed at 10keV of energy and absorption properties of the composite samples were analyzed using FTIR spectrophotometer, IRAffinity-1S from SHIMADZU, USA for PEG and ZnO functional groups in transmittance mode from 400 to 4000 cm⁻¹. UV visible absorption spectra were measured using UV-2700 spectrophotometer from SHIMADZU, USA in the range of 450 to 700 nm. Methylene blue (Azo) dye solution (0.1µM)

was used as contaminant in deionized water and its photocatalytic degradation for different exposure times under tungsten UV lamp (~equivalent to one sun intensity) in the presence of catalysis solution was recorded using UV-vis spectroscopy in a quartz cuvette. The synthesis and characterization of the samples were performed in University of Southern Denmark (SDU), Denmark.

2. Results and Discussion

The samples prepared by chemical routes, were characterized with Surface profilometer for knowing the thickness of the layer which was found to be ~164 µm. The films surface was inspected by optical microscope first to know about its uniformity followed by SEM measurements.

SEM images shows the ZnO tetrapod formation with inset highlighting one of the tetrapods in figure 2 (inset) with EDX performed on one of the legs for compositional information. The dimension of the tetrapods was found to lie between 10 to 50 µm, with each of the leg arranged at 105° with respect each other to form a tetrapodal geometry, thus, forming a 3D network with PEG. The legs of the tetrapod's are ~2 micron thick and ~20 micron in length, getting tapered at the ends (see the inset). EDX was performed on one of the legs of ZNT and presence of Zn with other elements like C and O suggests the capping of PEG on ZNT. PEG is known to be an important

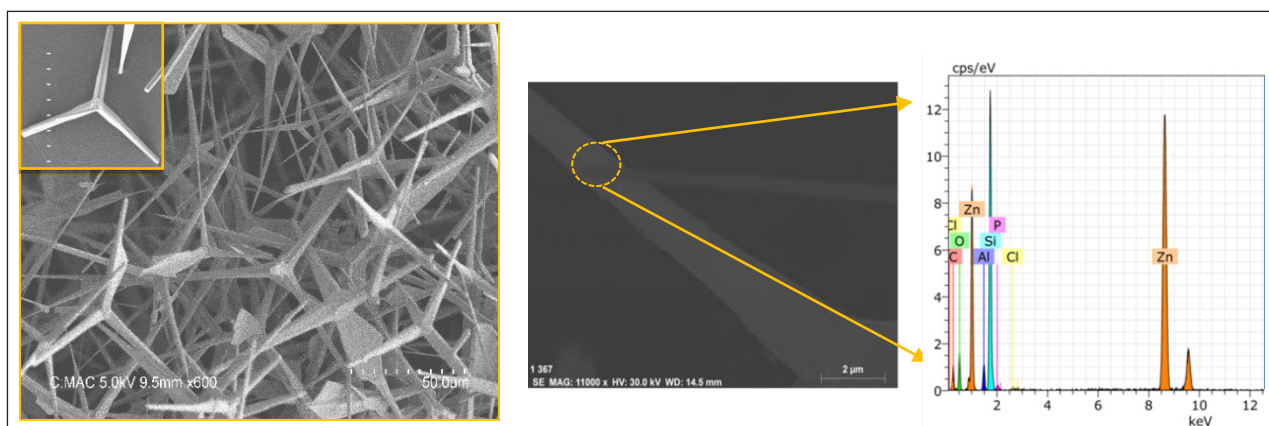


Figure 2: SEM image of the composite sample, inset showing one tetrapod, one of its legs shown with corresponding EDX

capping material which can bind to the ZnO thus, supports the growth in a particular direction. Therefore, due to the incorporation of PEG, the ZnO tetrapods have a capping of PEG along its legs. This is also He-ion microscopy images (not shown here).

IR spectroscopy gives qualitative information about the way in which the adsorbed PEG molecules are bound to the surface of ZnO. The peak between 3200 and 3600 cm^{-1} suggests the presence of strong (O-H) hydroxyl group, however, shifted to lower wavenumber 3437 cm^{-1} due to the formation of hydrogen bond at the ZnO-PEG interface [15,16] due to capping of PEG over ZNT. However, the characteristic sharp peak of Zn-O at 685, 585, 503 and 465 cm^{-1} are visible with splits into two peaks in the presence of PEG (as highlighted in the spectra) [16].

Table 1 shows the stretching and bending of various functional groups present in the composite material. As evident in the FTIR spectra that there are many peaks with lower transmittance are visible, however, major ones are shown here. The strong C-O stretching peak

observed between 1550 and 1690 cm^{-1} and the asymmetric stretching of the C-O between 1300 and 1390 cm^{-1} were also detectable.

Table 1: Functional groups present in the Composite sample

Functional Group	Wavenumber (cm^{-1})			Bending
OH	3437	2846	1965	(Symmetric stretching)
C-O-C	1652	1463	1360	(Asymmetric/symmetric stretching)
C-H	892	840		Bending
Zn-O	685	586 503	465	Stretching (metal oxide)

The presence of a peak at 830 cm^{-1} indicates that there are C-H groups from PEG. The peak at lower wavenumbers indicates the Zn-O at 494 to 685 cm^{-1} [16].

The absorbance spectra were recorded using the UV Visible spectrophotometer in the

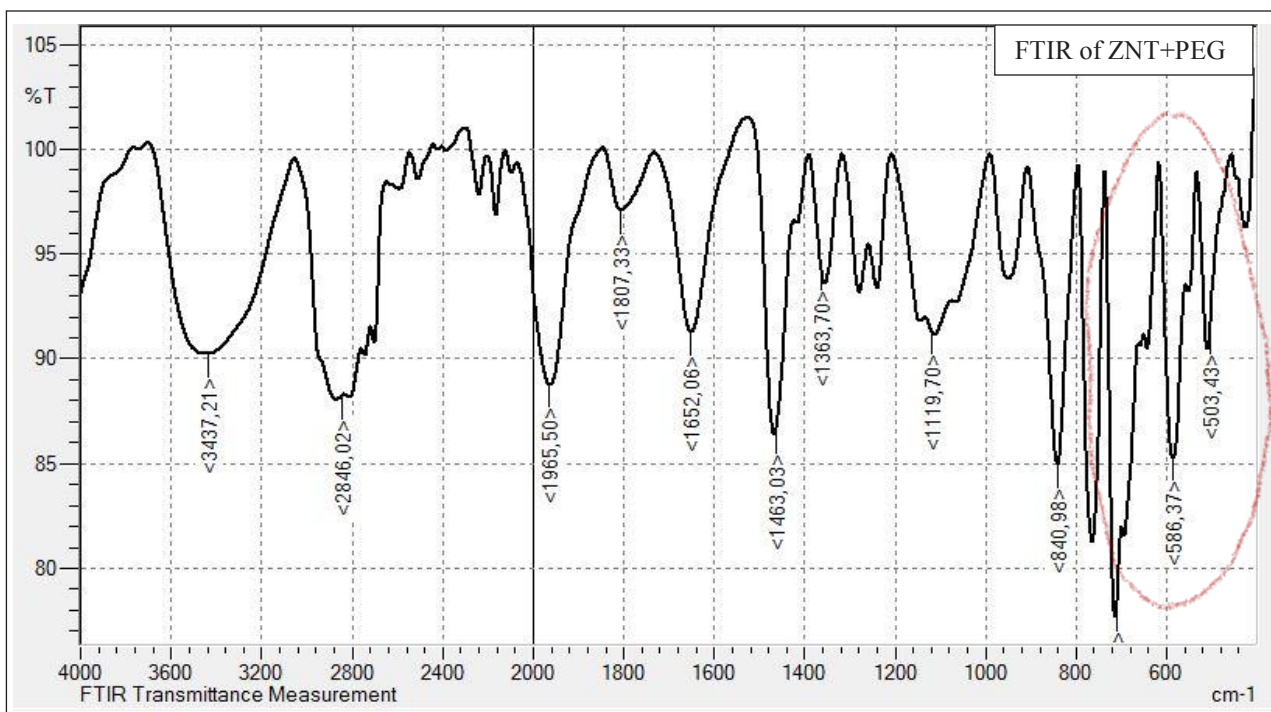


Figure 3: FTIR spectra of the polymer composite of PEG and ZNT sample

wavelength range of 200 to 700 nm as shown in figure 4. The absorption corresponding to PEG is visible at ~235 nm [16]. With incorporation of ZNT, the absorbance shifted to higher wavelength, due to the bond formation between Zn and H, as PEG has a capping over ZNT, and the peak corresponding to ZnO is visible at ~372 nm, shifted from its original position of 376 nm [17]. This is also suggested by FTIR and He-ion microscopy images.

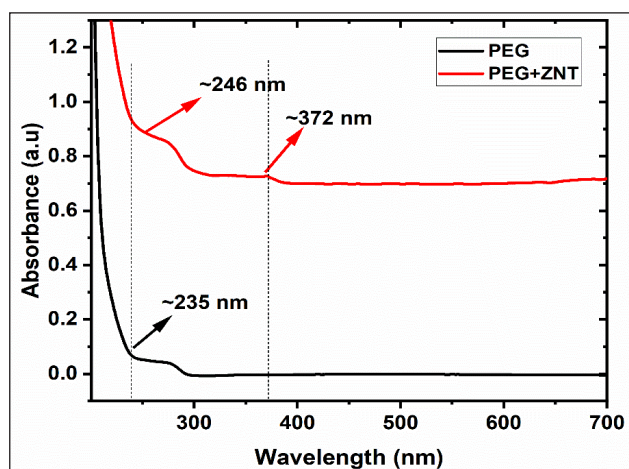


Figure 4: UV absorbance spectra of PEG and ZNT+PEG composite.

The photocatalytic activity of (ZNT+PEG) sample prepared in deionized water with methylene blue (azo) dye as contaminant was performed for different UV exposure time (up to 1 hour with 10 minutes exposure cycle) to monitor the degradation of the dye by optical absorption spectroscopy. 10 μ L solution of dye (0.1 μ M) was mixed with the 5 mL of catalyst solution (2.5 mg ZNT in 10 mL PEG) in deionized water. Figure 5 shows the absorption spectra of methylene blue dye exhibiting photocatalytic degradation in the presence of the catalyst for different UV light exposure time. The peak absorption of methylene blue is exhibited at ~665 nm with a shoulder at ~610 nm. Inset shows the rate of degradation. It can be clearly seen that absorption intensity falls with exposure time indicating dye degradation.

The kinetic of the dye degradation is described as,

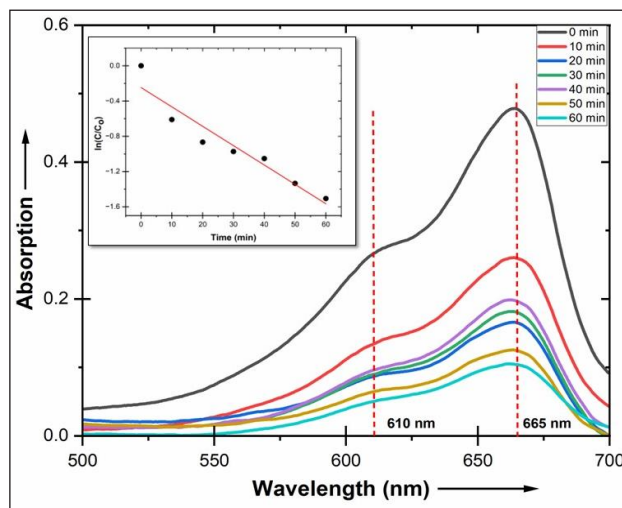


Figure 5: Absorption spectra of 0.1 μ methylene blue (Azo) dye showing photocatalytic reduction in the presence of composite solution mixed with deionized water, inset shows the photodegradation rate of the dye.

$$\ln\left(\frac{C_0}{C}\right) = kt \quad \text{-----} \quad (1)$$

where, C_0 is the initial concentration and C is concentration at time t of the dye, and k is the rate constant.

After a cycle of UV exposure, the concentration of the undegraded dye was estimated from the absorption intensities and the rate constant was determined by the slope of the plot of $\ln(C_0/C)$ versus time shown in the inset of figure 4 and found to be 0.02198 ± 0.00302 , indicating the degradation rate as ~0.022 per min.

As ZnO shows good photocatalytic degradation of organic compounds through indirect pathway involving hydroxyl radicals as the oxidizing agents, consequently, the as-synthesized ZnO tetrapods capped with PEG reported here should show a higher photocatalytic activity because of their unique structure which have more active surface area for the binding of organic (dye) molecules. Methylene blue can be activated by light to an excited state which in turn activates oxygen to yield oxidizing radicals (OH). When exposed to UV light, the conduction band electrons (e_{CB}^-) and valence-band holes (h_{VB}^+) are generated on the surface of ZnO tetrapods capped with PEG.

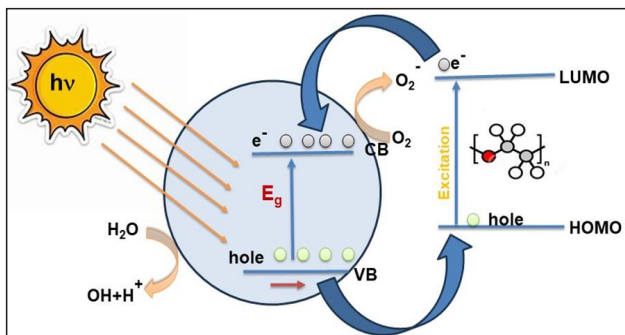
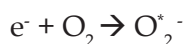
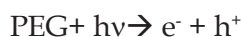
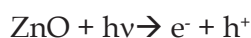


Figure 6: Schematic of photocatalytic action of composite material

The generated holes, reacted with PEG and water adhering to surfaces of ZnO to form highly reactive hydroxyl radicals (OH) which are responsible for degradation of organic dye [18] as shown in the schematic view in figure 6. The photocatalytic superiority of ZNT could be attributed to the presence of large specific area leading to the enhancement in dye adsorption, transportation and light harvesting. In addition to this, promotes the charge-transfer in the polymer composite material. Both the materials are UV sensitive and thus, the e-hole recombination was arrested. The mechanism of dye degradation in the presence of composite (ZNT+PEG) is given below:



Oxidation reaction: $h^+ + \text{methylene blue dye} \rightarrow \text{CO}_2$



Reduction reaction: $\cdot\text{OH} + \text{methylene blue dye} \rightarrow \text{CO}_2$

Further, the increase in charge transfer rates drastically reduces the direct recombination of the photogenerated electron/hole pairs [18-20] which is essential to enhance the photocatalytic efficiency in the degradation of dye molecule. Thus, resulted in an excellent photocatalytic performance. The studies are in progress to improve the properties with energetic ions for more efficient environmental remediation.

Conclusion

In this study, a novel 3D polymer composite material has been synthesized with Zinc Tetrapods and polyethylene glycol as an electrode for the photocatalytic activities. The sample shows good absorption peaks in the FTIR spectra confirming various functional groups of the PEG and ZnO. The length of ZNTs were found to lie between 10 to 50 μm . The samples have been tested for degradation of organic dye, methylene blue (azo dye) when mixed with deionize water (0.1mM) in the presence composite material in the solution form using absorption spectroscopy for different exposure time of UV light. The improved degradation was found for higher UV exposure time showing good photocatalyst response with rate of degradation as $\sim 0.022/\text{min}$, thus, provides a promising alternative for wastewater treatment. Further, have shown significant implications in the environment remediation and in the fabrication of functional devices.

Acknowledgements

The authors are grateful for the SIRE fellowship (SIR/2022/001573) awarded to IS from SERB, Department of Science and Technology, Govt. of India. University of Southern Denmark (SDU), Denmark is highly acknowledged for providing the experimental facilities to carry out this work at SDU, Denmark.

References

1. Yentekakis, I. V.; Dong, F. *Frontiers in Environmental Chemistry* **2020**, 5.
2. Kusvuran, E.; Gulnaz, O.; Irmak, S.; Atanur, O. M.; Yavuz, H. I.; Erbaturo, O. *Journal of hazardous materials* **2004**, 109 (1-3), 85-93.
3. Mills, A.; Le Hunte, S. *Journal of photochemistry and photobiology A: Chemistry* **1997**, 108 (1), 1-35.
4. Ma, Q.; Hu, X.; Liu, N.; Sharma, A.; Zhang, C.; Kawazoe, N.; Chen, G.; Yang, Y. *Journal of colloid and interface science* **2020**, 569, 101-113.
5. Liqiang, J.; Xiaojun, S.; Weimin, C.; Zili, X.; Yaoguo, D.; Honggang, F. *Journal of Physics and Chemistry of solids* **2003**, 64 (4), 615-623.
6. Nishikiori, H.; Nagaya, S.; Takikawa, T.; Kikuchi, A.; Yamakami, T.; Wagata, H.; Teshima, K.; Fujii, T. *Applied Catalysis B: Environmental* **2014**, 160, 651-657.
7. Lu, W.; Schmidt, H. *Advanced Powder Technology* **2008**, 19 (1), 1-12.

8. Sakthivel, S.; Baskaran, V.; Mahenthiran, S. *Journal of Pure Applied and Industrial Physics* **2015**,5 (2), 57-65.
9. Mishra, Y. K.; Kaps, S.; Schuchardt, A.; Paulowicz, I.; Jin, X.; Gedamu, D.; Wille, S.; Lupan, O.; Adelung, R. *KONA Powder and Particle Journal* **2014**,31, 92-110.
10. Li, D.; Zuo, S.; Xu, H.; Zan, J.; Sun, L.; Han, D.; Liao, W.; Zhang, B.; Xia, D. *Journal of colloid and interface science* **2018**,531, 28-36.
11. Kumbhakar, P.; Biswas, S.; Kumbhakar, P. *Optik* **2018**,154, 303-314.
12. Adhyapak, P. V.; Meshram, S. P.; Amalnerkar, D. P.; Mulla, I. S. *Ceramics International* **2014**,40 (1), 1951-1959.
13. Mishra, Y.K., Sören Kaps, Arnim Schuchardt, Ingo Paulowicz, Xin Jin, Dawit Gedamu, Stefan Freitag, Maria Claus, Sebastian Wille, Alexander Kovalev, Stanislav N. Gorb, Rainer Adelung., *Particle & Particle Systems Characterization*, 2013. **9**(30): p. 775-783.
14. Yogendra Kumar Mishra, Rainer Adelung; *Materialstoday*, 2018 **21**(6): p. 631-651.
15. Sudha, M., Senthilkumar S, Hariharan R, Suganthi A, Rajarajan M, *Journal of sol-gel science and technology*, 2013. **65**: p. 301-310.
16. Meshram, J., et al., *Materials Research Express*, 2018. **5**(4): p. 045016.
17. Aisida, S.O., et al., *Materials Chemistry and Physics*, 2020. **255**: p. 123603.
18. M.A. Tshabalala, B.F. Dejene and H.C. Swart; *Physica B: Condensed Matter* **2012** **407**(10) 2012, p. 1668-1671
19. Ye, C., Bando Y, Shen G, Dmitri G., *The Journal of Physical Chemistry B*, 2006. **110**(31): p. 15146-15151.
20. Jyoti Gaur, Mohinder Pal, Sanjeev Kumar, Harpreet Kaur, Gurmeet Singh Lotey, Kanchan Bala, Supreet and Arshdeep Kaur; *Functional Composites and Structures*, 2023 **5**(2), p. 025002.

	<p>Dr. Indra Sulania has been working as a Scientist at Inter University Accelerator Centre, New Delhi, for nearly 20 years. She has been awarded with prestigious SIRE fellowship from SERB, DST, Govt. of India. She has recently joined the Smart Materials Group, Nanosyd, Southern University of Denmark, Denmark with Prof. Y K Mishra and started working on smart materials based on the ZnO tetrapods for functional applications. She did her PhD in Physics from Jamia Millia Islamia, Delhi, in 2016. She has more than 100 papers in internationally reputed Journals with more than 1000 citations. Her areas of research are Sensors and catalysis, radiation resistant and shielding materials, ion beam induced modification of surfaces and applications, polymer composites and applications, ZnO tetrapod-based composites as functional materials etc.</p>
	<p>Prof. Yogendra Kumar Mishra is Professor MSO and Leader of Smart Materials group at Mads Clausen Institute, University of Southern Denmark (SDU), Sønderborg, Denmark. Before joining SDU, he was leading a group at Functional Nanomaterials Chair, Institute for Material Science, Kiel University, Germany. He did Ph. D. in Physics in 2008 from Inter University Accelerator Centre/Jawaharlal Nehru University, New Delhi, India. At SDU, NanoSYD, his main research focus is 'Smart Materials' for Advanced Sustainable Technologies'.</p>
	<p>Dr. Ambuj Tripathi is the Programme Leader of Materials Science Group. He has played a key role in setting up of materials science beamline and many in-situ/on-line facilities including in-situ STM, on-line ERDA and in-situ XRD facilities. His areas of research include Ion beam induced modification of carbon based 2-D materials and nanostructures, Ion beam induced modification of surfaces and interfaces and Synthesis and characterization of nanostructures.</p>
	<p>Dr. Ranjeet K Karn obtained his M.Sc. Physics in 2003 from IIT Guwahati. Afterward he joined for his Ph. D. In "Accelerator based Atomic Physics" at IUAC, New Delhi. Currently he is working as the Head of the PG Department of Physics at Jam. Cooperative College, Jamshedpur. He has developed his interest in various fields viz. X-ray Spectroscopy & Instrumentation, Ion-Atom /Solid Collision, Applied Nano-materials, Computational Physics, NLD & Physics Education for past ~17 Years.</p>
	<p>Ms. Elham Chamanehpour received her B.Sc. degree (2013) from Ferdowsi University of Mashhad and M.Sc. degree (2015) from University of Birjand, South Khorasan, Iran, in Environmental Science. She is pursuing her PhD from Iran and SDU, Denmark. Her research interests focus on the fabrication of smart nanoparticles, MOFs, and nanofibers for application in waste water treatment, medical uses and energy production.</p>
	<p>Ms. Ajani Lakmini Jayarathna J.A. is currently a master's student at Sirindhorn International Institute of Technology (SIIT), Thammasat University, Thailand. Her main research interests are 2D materials, composite materials, nano composites, and sensing applications</p>

A Chromene-Tetraphenylethylene AIEgen-based Chemodosimeter for Highly Selective Turn-off Detection of Bisulfite Ions and Nitroaromatics

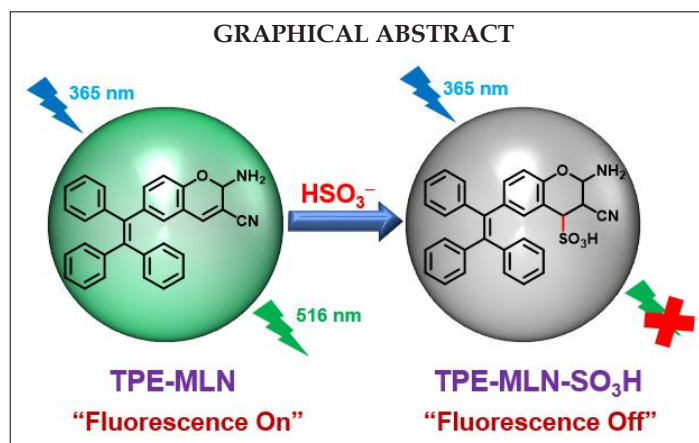
Akhil A. Bhosle, Mainak Banerjee,*Viraj G. Naik,Amrita Chatterjee*

Department of Chemistry, BITS Pilani, K K Birla Goa Campus, NH 17B Bypass Road, Zuarinagar 403726, Goa, INDIA

*E-mail: mainak@goa.bits-pilani.ac.in., amrita@goa.bits-pilani.ac.in

ABSTRACT

Bisulfite (HSO_3^-) is widely employed as an antioxidant, color stabilizer, and in the preservation of foods, pharmaceuticals and beverages. However, an excess of HSO_3^- can result in tissue damage, allergic reactions, and skin or eye discomfort. We have developed a chromene-coupled tetraphenylethylene-based aggregation-induced emission-active probe (TPE-MLN) and utilized it as a turn-off chemodosimeter for the selective detection of HSO_3^- ions. The AIE-active probe TPE-MLN is non-fluorescent in organic solvents and displays strong green emission at 516 nm at higher water fractions. The incremental addition of HSO_3^- ions resulted in a turn-off response by its nucleophilic addition across the olefinic bond of TPE-MLN. In the presence of numerous other interfering cations, anions, amino acids and neutral molecules, TPE-MLN remains indifferent and thus, it functions as a sensitive sensor for the detection of HSO_3^- ions with a limit of detection (LOD) as low as 9.36 ppb (0.9×10^{-7} M). Moreover, picric acid, one of the explosive nitroaromatics, was detected using the AIE property of TPE-MLN. Some benefits of this AIEgen over other molecular probes for HSO_3^- ions are its simple and affordable synthesis, quick response time, high selectivity and sensitivity and low LODs.



Keywords: Aggregation-induced Emission (AIE); Tetraphenylethylene (TPE); Bisulfite (HSO_3^-); Chemodosimeter, Nitroaromatics.

1. Introduction

The detection and precise quantification of bisulfite ions (HSO_3^-) plays a crucial role in the realm of environmental science, as it enables the effective monitoring of air and water quality. These ions serve as a direct indicator of sulfur dioxide (SO_2) pollution that upon extended exposure leads to various health concerns, including but not limited to asthma, chronic

bronchitis, lung cancer, as well as neurological and cardiovascular diseases.^{1,2} In contrast, its hydrated form bisulfite (HSO_3^-) is widely used in food and pharmaceutical preservation.^{3,4} The consumption of an excessive amount of HSO_3^- can lead to allergic responses, irritation of the skin and eyes, and potential harm to body tissues.⁵ In light of the adverse outcomes associated with these repercussions, a number of conventional analytical techniques have been devised to

evaluate the concentrations of these anions such as chromatography, electrochemical analysis, and capillary electrophoresis.⁶⁻⁹ However, the utilization of small-molecule fluorescent probes which can add HSO_3^- by nucleophilic addition to electron-deficient olefinic bonds has demonstrated itself as a more practical and efficient strategy for the prompt and highly sensitive identification of HSO_3^- .¹⁰⁻¹³ This process leads to a discernible alteration in fluorescence.

In 2001, Tang and co-workers introduced a breakthrough in the field of fluorescence with the discovery of aggregation-induced emission (AIE) active fluorophores.^{14,15} These innovative compounds offered a compelling solution to the persistent challenge of the aggregation-caused quenching (ACQ) effect that had plagued conventional fluorophores for years. Notably, these AIE-active fluorophores exhibit remarkable fluorescence when they are aggregated, effectively overcoming the limitations associated with classical fluorophores. Different AIEgens have been explored and demonstrated for sensing applications having scaffolds based on tetraphenylethylene (TPE), silole, borondipyrromethene, etc.¹⁶⁻¹⁹ Among AIEgens, TPE stands out as an exceptionally versatile luminogen owing to its straightforward and cost-effective synthesis, as well as its uncomplicated functionalization. TPE derivatives have become a popular choice for sensing and imaging applications, both within our research group and among other research groups.²⁰⁻²³

Heterocyclic frameworks incorporating 2-amino-3-cyano-4*H*-pyran, exemplified by compounds like 2-amino-4*H*-benzo[*h*]chromene-3-carbonitrile and 2-amino-5-oxo-4*H*,5*H*-pyrano[3,2-*c*]chromene-3-carbonitrile, represent significant structural motifs widely found in natural products and biologically active compounds.²⁴ Traditional chromene derivatives typically exhibit absorption peaks in the ultraviolet range, limiting their utility in biological applications.^{25,26} Consequently, there is a strong imperative to create analogs of chromene

that possess extended absorption and emission wavelengths. Although fluorescent probes based on TPE have been extensively investigated, the exploration of AIE-active chromene-based TPE for sensing purposes has been scarce. Bearing this in mind, our research endeavors focused on the development of a chromene-coupled TPE molecule, with the anticipated outcome of a bathochromic shift in the emission maxima of the TPE component.

Nitroaromatics are potent explosives that involve simpler synthetic protocols and are easily portable. When detonated, these substances affect the environment by contaminating the soil, water, and air systems. They are responsible for human health hazards, including cancer, liver dysfunction, respiratory issues, and skin ailments over long-term exposure. Nitroaromatic substances such as picric acid (PA), tri-nitrotoluene (TNT) and di-nitrotoluene (DNT) have been included in the Environmental Protection Agency's list of priority pollutants due to their substantial toxicity.^{27,28} Thus, highly accurate nitroaromatic compound detection is crucial and relevant. Numerous primary and advanced techniques have been used to detect such materials, including gas chromatography with a mass spectrometer, nuclear quadrupole resonance, X-ray diffraction and enhanced Raman spectrometry.²⁹ However, due to their high cost, complexity, lack of precision and labor-intensive nature of the manipulations, these techniques are not very practical for explosives detection in the field.³⁰ More interest has recently been shown in fluorescent chemosensors due to their operational simplicity, cost-effectiveness and reaction speed superiority.³¹ In this work, we demonstrate the synthesis of a chromene-coupled TPE molecule (TPE-MLN) and its utilization for the selective and sensitive detection of bisulfite ions and nitroaromatic compounds.

2. Experimental Section

2.1 Chemicals and reagents

Reagents like malononitrile and piperidine were obtained from TCI Chemicals.

Different inorganic salts and common solvents were procured from different commercial vendors and used as obtained. To monitor the progress of the reaction, thin-layer chromatography (TLC) was used with silica gel plates (0.25 mm, 60F-254). The TLC was visualized using UV lamps with wavelengths of 254 nm and 365 nm. Ultrapure deionized water was obtained using a Millipore water system (18 M Ω .cm) and was purged with N₂ for a duration of 15 minutes prior to its utilization.

2.2 Instrumentation and measurements

A 500 MHz Bruker Avance NMR spectrometer was used to record the NMR spectra. HRMS spectra were acquired from an Agilent LC-MS (model 6545 QTOF) equipped with an ESI ion source. JASCO V770 and FP-8500 model UV-vis spectrophotometer and spectrofluorimeter were used with the data pitch and bandwidth fixed at 1 nm and excitation and emission slit widths maintained at 2.5 nm for all the UV-vis and fluorescence experiments, respectively. The LCMS spectra were obtained using Agilent 6400B LC-MS, with ESI as the ion source.

2.3. Synthesis of 2-amino-6-(1,2,2-triphenylvinyl)-2H-chromene-3-carbonitrile (TPE-MLN):

The starting material, **TPE-OH-CHO**, was prepared using a two-step synthetic pathway in accordance with our previously documented method.³² In a 25 mL round-bottom flask, **TPE-OH-CHO** (0.38 g, 1 mmol) was taken and dissolved in 5 mL of ethanol. To this, malononitrile (66 mg, 1 mmol) and a catalytic amount (10 mol%) of piperidine were added. The reaction mixture was then refluxed for 3 h. After cooling the reaction mixture to room temperature, the precipitated product was collected by filtration and washed with water to afford a yellow solid. The crude product was further purified using flash chromatography, to afford the pure compound **TPE-MLN** as a yellow solid (0.39 g, yield: 91%); ¹H NMR (500 MHz, CDCl₃): δ (ppm) 8.71 (dd, $J_1 = 2.0$ Hz, $J_2 = 8.5$ Hz, 1H), 7.37 (dd, $J_1 = 2.0$

Hz, $J_2 = 8.5$ Hz, 1H), 7.23 (d, $J = 8.5$ Hz, 1H), 7.18-7.04 (m, 16H), 5.90 (s, 1H), 5.61 (s, 2H); ¹³C {¹H} NMR (125 MHz, CDCl₃): δ (ppm) 161.8, 161.7, 158.5, 157.3, 150.6, 143.1, 142.8, 142.7, 142.2, 141.9, 138.6, 137.5, 131.5, 131.2, 131.1, 128.12, 128.06, 127.7, 126.98, 126.93, 126.88, 118.0, 116.9, 115.8, 115.4, 98.7, 79.6; HRMS (ESI-TOF): m/z calcd for C₃₀H₂₂N₂O [M+H]⁺ 427.1805, found 427.1811.

2.4. Analytical procedures

In order to perform spectrofluorimetric analyses, a stock solution of 1 mM **TPE-MLN** in THF was prepared and further diluted to 10 μ M in 97% water-THF using deionized water (Milli-Q, 18 M Ω .cm) as per the requirement of the spectrofluorimetric studies. A 1 mM stock solution of bisulfite (HSO₃⁻) was prepared from its sodium salt. Similarly, for the selectivity studies, salts of sodium or potassium ions were used for different anions and nitrates or chlorides for different cations. The different pH solutions were prepared from three buffer systems: 0.1 M acetate buffer (pH 3-6), 10 mM HEPES buffer (pH 7-10) and carbonate buffer pH (11-12). Different food samples (white sugar, brown sugar, crystal sugar, mushroom, and vermicelli) were taken in water (1g of finely crushed sample in 5 mL water), sonicated for 30 minutes, and then further incubated for 24 hours in order to perform real sample analysis. For analysis, the supernatant solution was collected and spiked with known quantities of HSO₃⁻. Any particulate matter in the solutions was filtered out using a 0.22 μ m syringe filter prior to each analysis. After excitation at 365 nm, all of the fluorimetric data were acquired between 370 and 650 nm. The average data for each analysis is provided based on three repetitions carried out at room temperature (25 °C).

2.5 DFT studies

Quantum mechanical investigations were conducted using the Gaussian 09 program, encompassing semiempirical-CI (ZINDO/CI), density functional theory (DFT) and time-

dependent density functional theory (TD-DFT).^{33,34} The ground and excited state geometry optimization calculations of **TPE-MLN** were executed with Becke's three-parameter exchange functions (B3) coupled with the Lee-Yang-Parr correlation function (LYP), and a 6-31G basis set.

3. Results and discussion

3.1. Design and synthesis of the probe, **TPE-MLN**

A chromene-based tetraphenylethylene probe was expected to behave as a chemodosimeter for bisulfite ions by the addition of the analyte across the olefinic double bond. Accordingly, a D- π -A probe, 2-amino-6-(1,2,2-triphenylvinyl)-2*H*-chromene-3-carbonitrile (**TPE-MLN**) was designed and synthesized by incorporating a 2-amino-chromene-3-carbonitrile moiety into a tetraphenylethylene scaffold. It was envisaged that the presence of the strong electron-withdrawing group (-CN) would result in the quick addition of bisulfite ions across the electron-deficient olefinic bond of the chromene moiety leading to a change in fluorimetric response. The interruption in the extended conjugation of the probe by the addition of the analyte was expected to produce a turn-off response. The chemodosimeter, **TPE-MLN** was synthesized via a single-step reaction from **TPE-OH-CHO** (Scheme 1). The starting material, **TPE-OH-CHO** was synthesized by a two-step synthetic route following our previously reported procedure.³² Firstly, the McMurry coupling reaction of benzophenone with 4-hydroxy

benzophenone afforded **TPE-OH** in good yields. Further **TPE-OH** was formylated at the *ortho* position following Duff's procedure, to produce **TPE-OH-CHO** as a yellow solid. The target compound, 2-amino-6-(1,2,2-triphenylvinyl)-2*H*-chromene-3-carbonitrile (**TPE-MLN**), was synthesized by Knoevenagel condensation of **TPE-OH-CHO** and malononitrile in the presence of piperidine which upon further cycloaddition afforded the probe molecule as a yellow-colored solid with bright green fluorescence and an excellent yield of 91%. **TPE-MLN** was characterized using ¹H NMR, ¹³C NMR, and HRMS analysis (Fig. 1). The peaks at δ 8.71, 5.90 and 5.61 in ¹H NMR corresponded to the olefinic proton, the proton of the carbon-bearing -NH₂ group and of the -NH₂ group, whereas, the peaks at 115.39, 98.72 and 79.58 in ¹³C NMR correspond to the nitrile group, olefinic carbon-bearing nitrile group, and carbon-bearing -NH₂ group of chromene moiety, respectively, indicating the formation of **TPE-MLN**.

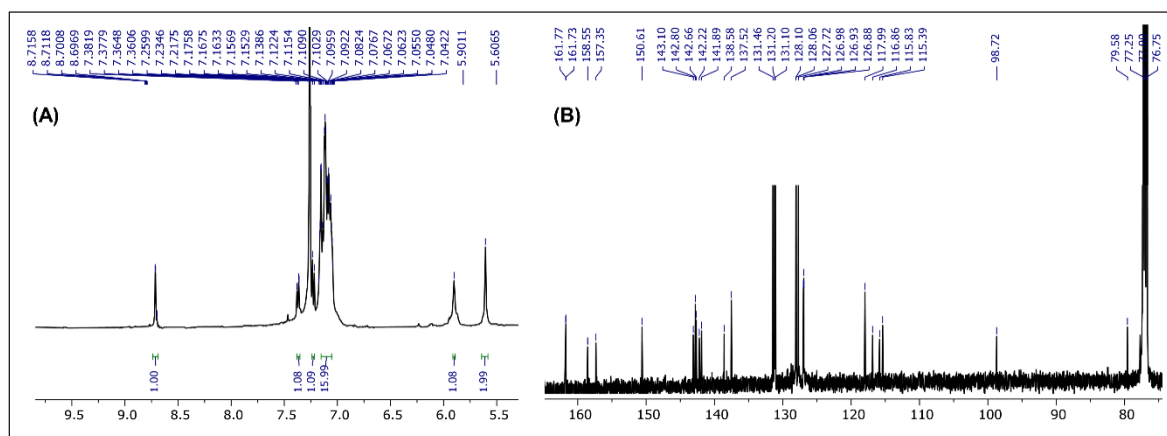
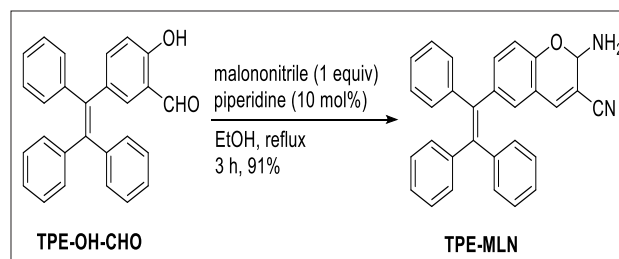


Fig. 1. (A) ¹H NMR (500 MHz) and (B) ¹³C NMR (125 MHz) spectra of **TPE-MLN** in CDCl₃.

3.2. AIE property of TPE-MLN

The AIE-active tetraphenylethylene scaffold was expected to give the chemodosimeter an aggregation-induced emission property. Accordingly, the solubility of the probe was first checked in different organic solvents. The probe was non-fluorescent in organic solvents and highly soluble in different polar protic and polar aprotic solvents such as THF, ACN, DMF, DMSO and EtOH. The UV-vis response of the probe (10 μ M) was first studied which showed an absorption band at 365 nm (Fig. 2A). Next, the emission properties of the probe (10 μ M) were investigated and a negligible emission was observed at λ_{max} 516 nm upon excitation at 365 nm in all the solvents. The aggregation-induced emission behavior of the probe was studied in THF by gradually increasing the water fractions in the water-organic solvent mixtures. The probe

displayed typical AIE behavior with negligible fluorescence emission in THF and water-THF till 60% water fractions (Fig. 2B,C). A further increase in the water fractions resulted in fluorescence enhancement with the maximum intensity being displayed at 97% water fraction. A slight decrease in emission intensity at 99% water fraction may be due to phasing out of the probe molecule due to its reduced solubility in the higher percentage of water. Subsequently, the higher water fractions (80-99%) were investigated with other organic solvents as well and it was observed that the AIE behavior is similar with comparable emission properties (Fig. 2D). However, the water-THF fraction was found to have higher intensities compared to other solvent-water fractions and hence 97% water-THF was considered as the ideal solvent system to conduct all the fluorimetric studies. In a subsequent study, the

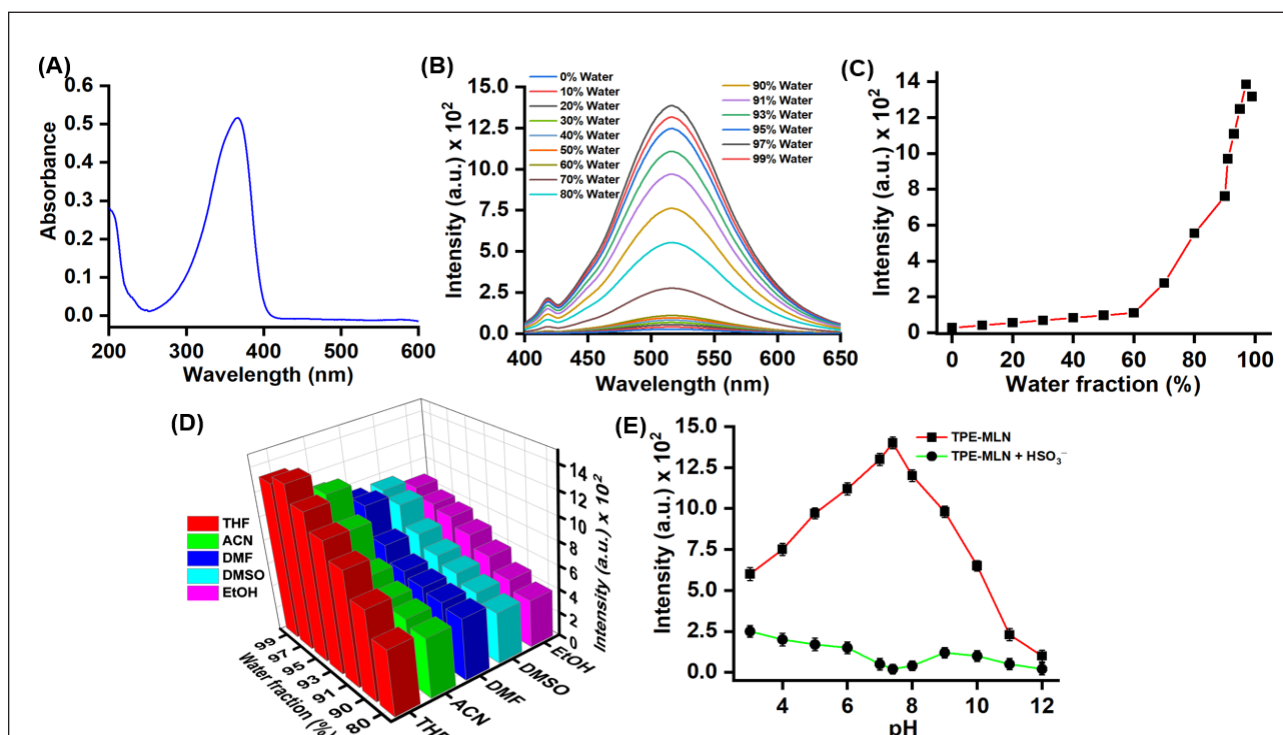


Fig.2. (A) The UV-vis absorption spectrum of TPE-MLN (10 μ M) in THF; (B) The change in fluorescence intensities of 10 μ M TPE-MLN at variable water-THF fractions (λ_{ex} 365 nm, λ_{em} 516 nm); (C) The change in the fluorescence intensity of TPE-MLN at 516 nm as a function of different percentages of the water fraction in THF; (D) The fluorescence response of TPE-MLN in different organic solvent-water fractions; (E) The effect of pH on the emission intensities of TPE-MLN (10 μ M) at λ_{max} 516 nm in the absence and the presence of 1.0 equiv of HSO_3^- (λ_{ex} 365 nm; λ_{em} 516 nm).

quantum yield of TPE-MLN in the aggregated state was recorded with fluorescein as the standard which displayed a decent fluorescence quantum yield (Φ_F) of 0.19 in 97% water-THF.³⁵ Next, we investigated the emission characteristics of TPE-MLN across a broad pH range (pH 3-12). Notably, TPE-MLN exhibited strong fluorescence within the near-neutral pH range (pH 6-8). As anticipated, the most intense emission occurred at the physiological pH of 7.4, underscoring the applicability of the probe for sensing purposes in biological samples at physiological conditions (Fig. 2E).

3.3. HSO_3^- sensing studies using TPE-MLN

In the next set of experiments, the fluorimetric responses of TPE-MLN (10 μM in 97% water-THF) were recorded upon the incremental addition of HSO_3^- . The addition of HSO_3^- ions resulted in a quick decrease in the emission intensities at 516 nm. The decrease was proportional to HSO_3^- ions concentration and saturation point was eventually obtained upon the addition of 10 μM (1.0 equiv) of HSO_3^- with almost 98% fluorescence quenching (Fig. 3). Further, the maximum fluorescence quenching of 10 μM TPE-MLN upon the addition of 1.0 equivalent of HSO_3^- required just 5 min (Fig. 4A). The pH-dependent response of TPE-MLN was examined across various pH ranging from 3 to 12. As anticipated,

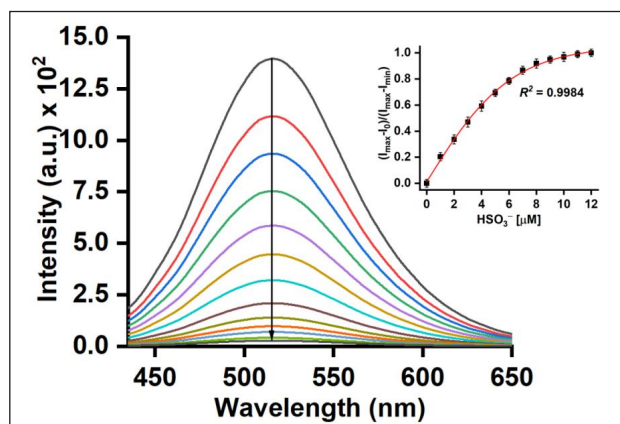


Fig. 3. The change in emission intensities of TPE-MLN (10 μM in 97% water-THF) upon incremental addition of HSO_3^- (0-12 μM) (λ_{ex} 365 nm; λ_{em} 516 nm); Inset: A plot of the ratio of fluorescence intensities vs concentration of HSO_3^- (0-12 μM).

TPE-MLN exhibited excellent sensitivity towards HSO_3^- within the near-neutral pH range of 6-8 (Fig. 2E). However, pH 7.4 was chosen as the optimal pH due to its best fluorescence output, and all subsequent analytical investigations were conducted at this pH with an incubation period of 5 min. A high regression coefficient of 0.9984 was obtained upon plotting the graph of the ratios of relative intensities of the probe at 516 nm as a function of HSO_3^- concentration (Inset, Fig. 3). In a complementary analysis, we focused on the detection of HSO_3^- ions at lower concentration ranges and observed a strong linear correlation

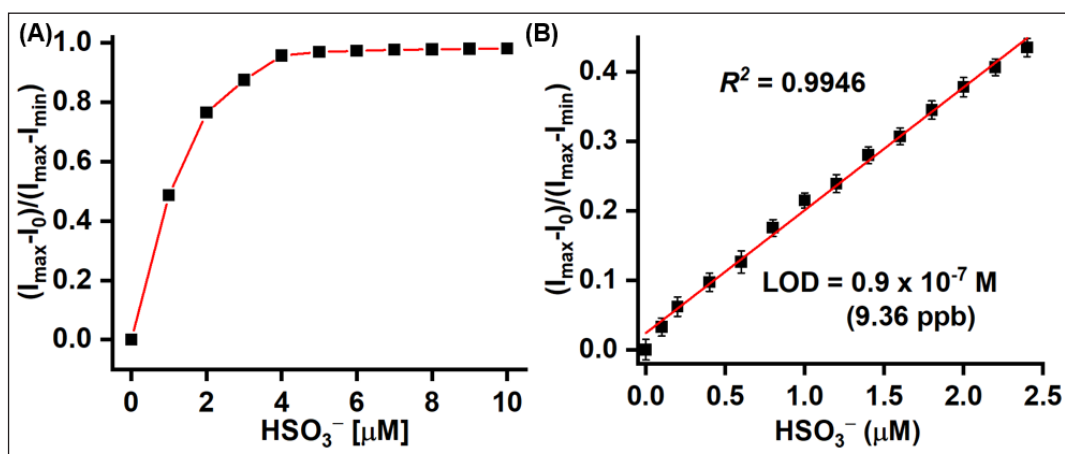


Fig. 4. (A) Time-dependent study and effect on the relative emission intensities of TPE-MLN (10 μM) upon addition of 1.0 equiv of HSO_3^- (λ_{ex} 365 nm; λ_{em} 516 nm); (B) The fluorimetric responses of TPE-MLN (10 μM) at the lower concentration range of HSO_3^- (0-2.5 μM) (λ_{ex} 365 nm, λ_{em} 516 nm).

within the 0–2.5 μM range, with a high regression coefficient ($R^2 = 0.9946$). Using this data, the limit of detection (LOD) was calculated as 0.9×10^{-7} M (9.36 ppb) according to the $3\sigma/k$ equation (Fig. 4B).

3.4. Selectivity of TPE-MLN towards HSO_3^-

After having successfully showcased the sensitive detection of HSO_3^- ions, the next crucial step was to ascertain and address the potential interference of other analytes in the sensing process. Consequently, a comprehensive evaluation was conducted to identify potential competitors to HSO_3^- , including anions like Cl^- , Br^- , I^- , F^- , CN^- , N_3^- , SH^- , OH^- , NO_3^- , NO_2^- , SO_4^{2-} , PO_4^{3-} , SCN^- , ClO^- , and S^{2-} . To assess their impact,

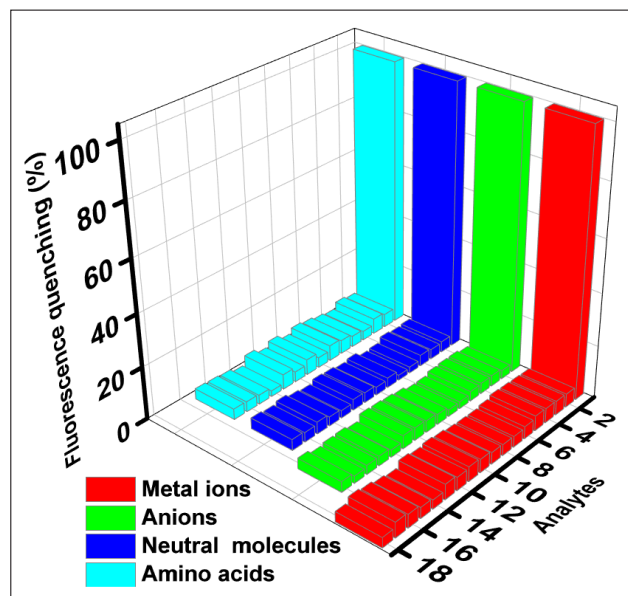


Fig. 5. The fluorimetric responses of various metal ions (2. Na^+ , 3. Mg^{2+} , 4. Al^{3+} , 5. K^+ , 6. Ca^{2+} , 7. Cr^{3+} , 8. Mn^{2+} , 9. Fe^{2+} , 10. Fe^{3+} , 11. Co^{2+} , 12. Ni^{2+} , 13. Cu^{2+} , 14. Zn^{2+} , 15. Pd^{2+} , 16. Ag^+ , 17. Hg^{2+} , 18. Pb^{2+}), anions (2. Cl^- , 3. Br^- , 4. I^- , 5. F^- , 6. CN^- , 7. N_3^- , 8. SH^- , 9. OH^- , 10. NO_3^- , 11. NO_2^- , 12. SO_4^{2-} , 13. PO_4^{3-} , 14. SCN^- , 15. ClO^- , 16. S^{2-}), neutral molecules (2. Urea, 3. HMTA, 4. dopamine, 5. Et_3N , 6. guanine, 7. benzylamine, 8. Et_2NH , 9. 2-aminopyridine, 10. 3-aminopyridine, 11. dicyclohexylamine, 12. pyridine, 13. melamine, 14. 4-aminopyridine, 15. dodecylamine), amino acids (2. tyr, 3. gly, 4. ala, 5. phe, 6. asp, 7. his, 8. pro, 9. cys, 10. arg, 11. val, 12. ser, 13. leu, 14. Lys, 15. L-DOPA) ($100 \mu\text{M}$) towards TPE-MLN ($10 \mu\text{M}$) under optimized conditions ($\lambda_{\text{ex}} 365 \text{ nm}$; $\lambda_{\text{em}} 516 \text{ nm}$) [Entry 1 is control (HSO_3^-)].

these analytes were introduced in substantial excess ($100 \mu\text{M}$) to a $10 \mu\text{M}$ solution of TPE-MLN, and their individual responses were meticulously recorded. Encouragingly, no significant reduction in fluorescence intensity at 516 nm was observed upon the addition of any of these analytes (Fig. 5). Subsequently, an extensive assessment was carried out to examine the potential interference of various metal ions (Na^+ , Mg^{2+} , Al^{3+} , K^+ , Ca^{2+} , Cr^{3+} , Mn^{2+} , Fe^{2+} , Fe^{3+} , Co^{2+} , Ni^{2+} , Cu^{2+} , Zn^{2+} , Pd^{2+} , Ag^+ , Hg^{2+} , Pb^{2+}), amino acids (tyr, gly, ala, phe, asp, his, pro, cys, arg, val, ser, leu, lys, L-DOPA), neutral amines (Urea, HMTA, dopamine, Et_3N , guanine, benzylamine, Et_2NH , 2-aminopyridine, 3-aminopyridine, dicyclohexylamine, pyridine, melamine, 4-aminopyridine, dodecyl amine). Each of these ions was added at a concentration of $100 \mu\text{M}$ to the probe solution ($10 \mu\text{M}$), yielding consistent results with no significant drop in emission intensities. These consistent outcomes in all the studies confirmed the selectivity of the probe, TPE-MLN towards HSO_3^- .

3.5. Theoretical calculations by DFT study

The electronic distribution of TPE-MLN in its energy-minimized ground and excited states was elucidated through the application of density functional theory (DFT) and time-dependent density-functional theory (TDDFT) methods.^{33,34} In TPE-MLN, the electron density is mostly located over the tetraphenylethylene moiety in the HOMO, which gets delocalized towards the chromene moiety in the LUMO. However, the electronic distribution is not completely delocalized and the electronic cloud is slightly located on the phenyl rings of TPE as well (Fig. 6). In contrast, the electronic density is completely shifted onto the electron-deficient chromene moiety of the probe in TPE-MLN- SO_3H . As the electronic transitions from the ground state to an excited state occur, the electron-withdrawing chromene segment forms a pathway for the displacement of the π -electron cloud due to HSO_3^- addition, and the extended conjugation is lost. This charge transfer process is effectively accompanied by non-radiative decay during

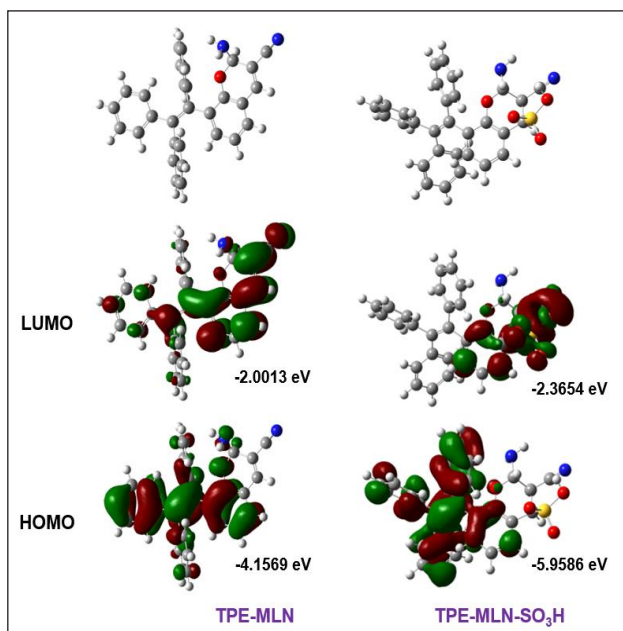


Fig.6. DFT optimized structures and electronic distributions in the HOMO and LUMO state of TPE-MLN and TPE-MLN-SO₃H.

the nucleophilic addition reaction, ultimately resulting in the extinguishing of TPE-MLN-SO₃H fluorescence.

3.6. Sensing mechanism

The nucleophilic addition of an analyte such as HSO₃⁻ across an olefinic double bond is well known and many chemodosimeters have been demonstrated adopting the nucleophilic attack of bisulfite across an electron-deficient olefinic bond as of now. However, to prove the sensing mechanism of the chemodosimeter towards HSO₃⁻, the Job's continuous variation plot was studied. Accordingly, the concentration of the probe, TPE-MLN and HSO₃⁻ ions were varied between 0–10 μM in the sensing assembly and their fluorimetric responses were recorded at optimized parameters. The Job's plot displayed a deviation point at 0.49 mole fraction of HSO₃⁻ indicating a 1:1 binding stoichiometry between

TPE-MLN and HSO₃⁻ ions (Fig. 7). As discussed in section 3.5, the electron-withdrawing chromene segment serves as a conduit for the displacement of the π-electron cloud, facilitated by the addition of HSO₃⁻ for the electronic transitions from the ground state to an excited state, leading to the loss of extended conjugation. This process effectively couples with non-radiative decay during the nucleophilic addition, ultimately quenching TPE-MLN-SO₃H fluorescence during the charge transfer (Scheme 2). Furthermore, the definitive

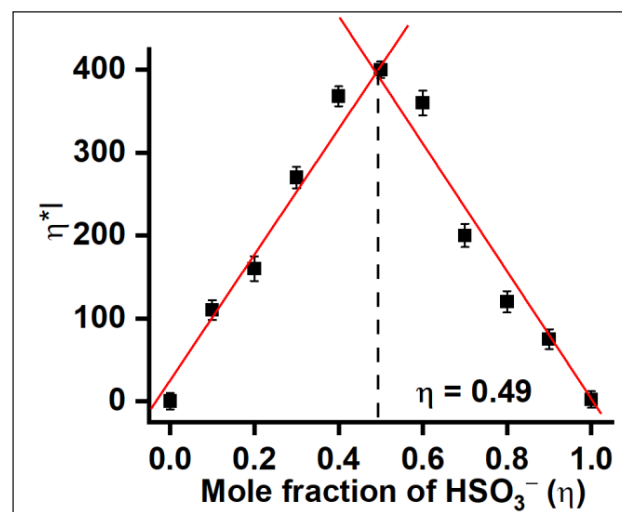
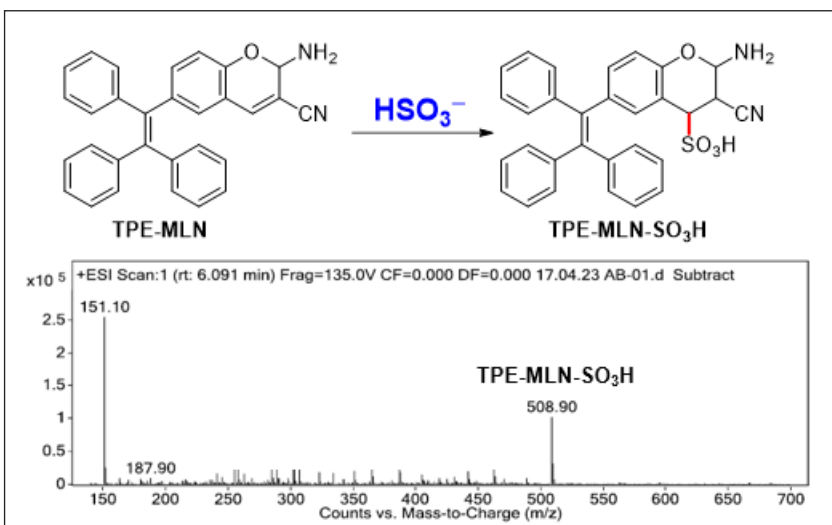


Fig. 7. Job's plot for the determination of the stoichiometry of TPE-MLN-SO₃H in the complex (λ_{ex} 365 nm; λ_{em} 516 nm).



Scheme 2. Plausible sensing mechanism by the nucleophilic addition of bisulfite ions across the olefinic bond of TPE-MLN and the corresponding LC-MS spectrum.

confirmation of nucleophilic addition of HSO_3^- across the olefinic bond (as depicted in Scheme 2) is reinforced by the prominent appearance of a peak at m/z 508.1, which corresponds to the molecular ion peak of **TPE-MLN-SO₃H** in the ESI-MS.

3.7. Determination of HSO_3^- in real samples

After demonstrating the high selectivity and sensitivity of **TPE-MLN** towards HSO_3^- , assessing the practical utility of **TPE-MLN** in real-world applications was crucial. To this end, the detection of HSO_3^- using **TPE-MLN** was carried out by spiking HSO_3^- ions into various food samples such as mushroom, vermicelli, crystal sugar, white sugar and brown sugar at lower concentration levels. The fluorescence intensities of the solutions, following the addition of **TPE-MLN** (at a concentration of 10 μM), were recorded. Subsequently, these intensities at 516 nm were utilized to generate %recoveries for the analytes within the real samples based on a standard graph. Remarkably, all the tested samples exhibited significant HSO_3^- recovery, irrespective of their source (Table 1). Overall, it can be concluded that the sensing system performs exceptionally well for the detection of HSO_3^- in real-world samples.

3.8. Nitroaromatics sensing studies using **TPE-MLN**

The AIE-active probe, **TPE-MLN** was expected to show a turn-off response towards nitroaromatic compounds (NACs) as these compounds being strong energy acceptors tend

to quench the AIE property of the AIEgens by intercalation in between the layers of the aggregated states of the electron-rich AIEgens. NACs such as picric acid (PA), tri-nitrotoluene (TNT) and di-nitrotoluene (DNT) have been included in the Environmental Protection Agency's list of priority pollutants due to their substantial toxicity. The gradual addition of picric acid was found to quench the emission intensities of **TPE-MLN** and complete quenching occurred around 140 μM of PA. The ultimate saturation was observed around 100 μM of PA and a very high regression coefficient of 0.9993 was obtained (Fig. 8A). Encouraged by the results, the sensing of PA was also studied at a lower concentration range and again high linearity was displayed for concentration ranges of 0–10 μM with a regression coefficient of 0.9969 (Fig. 8B). The limit of detection was calculated using the $3\sigma/k$ equation and was found to be as low as 0.05×10^{-6} M (11.4 ppb). Next, the selectivity studies were conducted in the presence of a few other NACs and electron-deficient and electron-rich aromatic compounds and selected neutral molecules. However, there was no discernible turn-off response, suggesting that **TPE-MLN** is only selective for nitroaromatics (Fig. 8C). The primary cause of fluorescence quenching can be attributed to the non-covalent interaction between the electron-rich aromatic rings of **TPE-MLN** and electron-deficient NACs. It is plausible that the intercalation of nitroaromatics within the organized array of **TPE-MLN**, driven by more favorable π - π interactions, disrupts its

Table 1. Real sample analysis data for different food samples pre-spiked with the known concentration of HSO_3^-

Sample	HSO_3^- added (μM)	HSO_3^- found (μM)	Recovery (%)	RSD (n = 3)
White Sugar	0.4	0.407	101.8	3.8
Brown Sugar	0.8	0.821	102.7	3.0
Crystal Sugar	1.2	1.202	100.2	3.4
Vermicelli	1.6	1.662	103.9	2.8
Mushroom	2.2	2.264	102.9	3.9

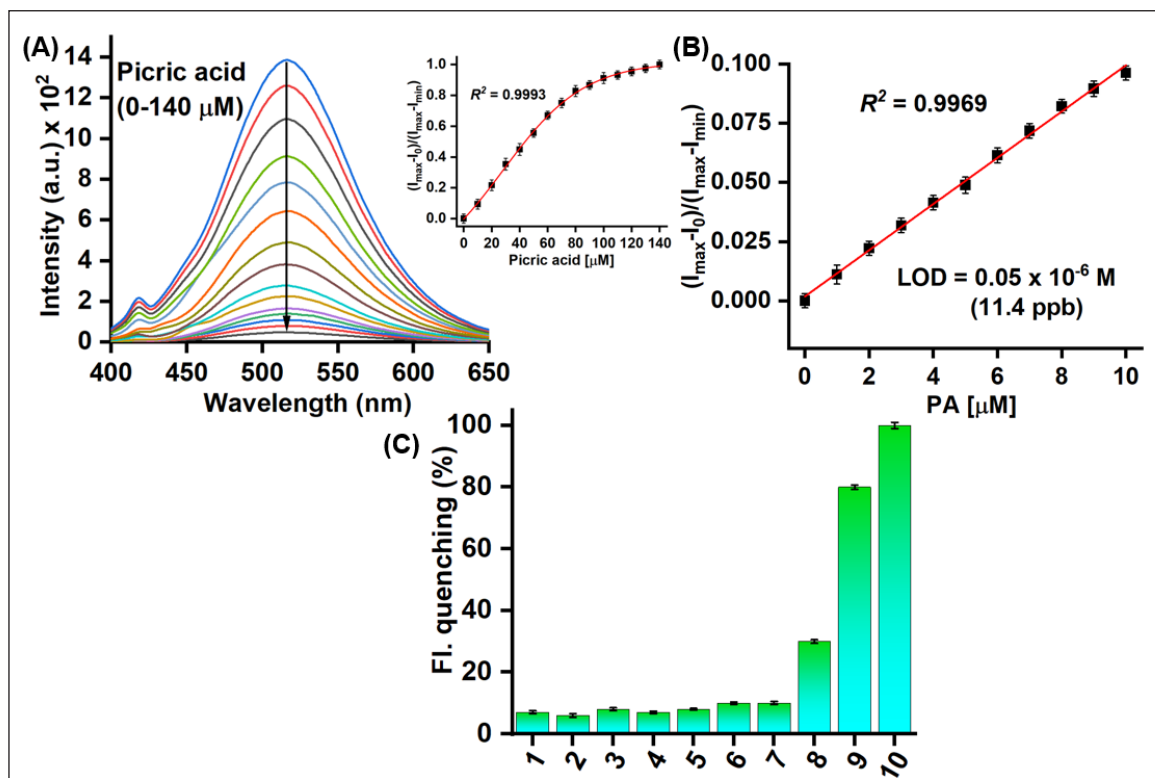


Fig. 8. The change in emission intensities of TPE-MLN (10 μM in 97% water-THF) upon incremental addition of picric acid (0–140 μM); Inset: A plot of the ratio of fluorescence intensities vs concentration of picric acid (0–140 μM); (B) The fluorimetric responses of TPE-MLN (10 μM) at the lower concentration range of picric acid (0–10 μM); (C) The fluorimetric responses of various competing species (300 μM) (1. aminophenol, 2. bromophenol, 3. toluene, 4. benzonitrile, 5. 2-nitropropane, 6. nitromethane, 7. nitrobenzene, 8. 4-nitrotoluene, 9. 2,4-dinitrochlorobenzene, 10. picric acid) towards TPE-MLN (10 μM) under optimized conditions (λ_{ex} 365 nm; λ_{em} 516 nm).

aggregation, resulting in the loss of AIE property of the probe. Consequently, TPE-MLN exhibits exceptional promise as a probe for detecting electron-deficient nitroaromatics.

4. Conclusion

In summary, we have successfully demonstrated the use of a chromene-coupled tetraphenylethylene-based aggregation-induced emission-active probe, TPE-MLN as a turn-off chemodosimeter for the selective detection of HSO_3^- ions and nitroaromatics. TPE-MLN was synthesized via Knoevenagel condensation followed by cyclization. The probe exhibits high solubility and negligible fluorescence in various organic solvents. It demonstrates the classical behavior of aggregation-induced emission (AIE) compound, with steady fluorescence

observed at elevated water fractions, reaching its peak emission intensity at a 97% water-THF mixture. It exhibits a descent quantum yield of 0.19 at 97% water-THF. Furthermore, TPE-MLN showed high selectivity towards bisulfite ions, distinguishing itself from a plethora of competing interfering species, including anions, cations, amino acids, and neutral molecules. The Job's plot and LCMS analyses established that the turn-off sensing occurs by the addition of the bisulfite ions across the olefinic bond of the chromene moiety in TPE-MLN. Notably, TPE-MLN boasts a remarkably low limit of detection (LOD) for bisulfite ions, quantified at 0.9×10^{-7} M (9.36 ppb). Moreover, the probe's AIE-quenching capability enabled the detection of picric acid, an explosive nitroaromatic, at the micromolar level, underscoring its versatility and

applicability in hazardous NACs sensing. **TPE-MLN** offers several notable advantages including its straightforward synthesis, rapid response kinetics, an ultralow limit of detection for bisulfite ions, exceptional selectivity, and effectiveness in high aqueous environments.

5. Acknowledgments

A.A.B. expresses gratitude to BITS Pilani for the research fellowship. DST-FIST (No. SR/FST/CSI-232-2011) is acknowledged for providing computational facilities in the department of chemistry. NMR and LCMS analyses were acquired from Central Sophisticated Instrumentation Facility (CSIF), BITS Pilani, K K Birla Goa Campus.

6. References

1. Shi, X. *J. Inorg. Biochem.* **1994**, *56*, 155–165.
2. Iwasawa, S.; Kikuchi, Y.; Nishiwaki, Y.; Nakano, M.; Michikawa, T.; Tsuboi, T.; Tanaka, S.; Uemura, T.; Ishigami, A.; Nakashima, H.; Takebayashi, T. *J. Occup. Health* **2009**, *51*, 38–47.
3. Fazio, T.; Warner, C. R. *Food Addit. Contam.* **1990**, *7*, 433–454.
4. Okamoto, N.; Bito, T.; Hiura, N.; Yamamoto, A.; Iida, M.; Baba, Y.; Fujita, T.; Ishihara, A.; Yabuta, Y.; Watanabe, F. *ACS Omega* **2020**, *5*, 6207–6214.
5. Gunnison, A. F.; Jacobsen, D. W.; Schwartz, H. J. *Crit. Rev. Toxicol.* **1987**, *17*, 185–214.
6. Urupina, D.; Gaudion, V.; Romanias, M. N.; Verrielle, M.; Thevenet, F. *Talanta* **2020**, *219*, 121318.
7. Villalobos, M. B.; Ibarra, J.; Gidi, L.; Cavieres, V.; Aguirre, M. J.; Ramirez, G.; Arce, R. *Catalysts* **2022**, *12*, 1675.
8. Fukana, N.; Sonsa-ard, T.; Chantipmanee, N.; Hauser, P. C.; Wilairat, P.; Nacapricha, D. *Sens. Actuators B* **2021**, *339*, 129838.
9. de Macedo, A. N.; Jiwa, M. I. Y.; Macri, J.; Belostotsky, V.; Hill, S.; Britz-McKibbin, P. *Anal. Chem.* **2013**, *85*, 11112–11120.
10. Feng, H.; Liu, J.; Qaitoon, A.; Meng, Q.; Sultanbawa, Y.; Zhang, Z.; Xu, Z. P.; Zhang, R. *TrAC Trends Anal. Chem.* **2021**, *136*, 116199.
11. Li, S.; Wang, L.; Ma, Y.; Lin, W. *Talanta* **2023**, *260*, 124615.
12. Li, H.; Yue, L.; Huang, H.; Chen, Z.; Guo, Y.; Lin, W. *J. Photochem. Photobiol. A* **2023**, *441*, 114684.
13. Tamima, U.; Santra, M.; Song, C. W.; Reo, Y. J.; Ahn, K. H. *Anal. Chem.* **2019**, *91*, 10779–10785.
14. Mei, J.; Leung, N. L. C.; Kwok, R. T. K.; Lam, J. W. Y.; Tang, B. Z. *Chem. Rev.* **2015**, *115*, 11718–11940.
15. Jimenez, E. R.; Rodriguez, H. J. *Mater. Sci.* **2020**, *55*, 1366–1387.
16. La, D. D.; Bhosale, S. V.; Jones, L. A.; Bhosale, S. V. *ACS Appl. Mater. Interfaces* **2018**, *10*, 12189–12216.
17. Zhao, Z.; He, B.; Tang, B. Z. *Chem. Sci.* **2015**, *6*, 5347–5365.
18. Tao, T.; Wang, S.-R.; Chen, L.; Qiu, H.; Xu, J.; Chen, M.-D. *Inorg. Chem. Commun.* **2015**, *62*, 67–70.
19. Wang, H.; Zhao, E.; Lam, J. W. Y.; Tang, B. Z. *Mater. Today* **2015**, *18*, 365–377.
20. Kumar, V.; Naik, V. G.; Das, A.; Bal, S. B.; Biswas, M.; Kumar, N.; Ganguly, A.; Chatterjee, A.; Banerjee, M. *Tetrahedron* **2019**, *27*, 3722–3732.
21. Naik, V. G.; Kumar, V.; Bhasikuttan, A. C.; Kadu, K.; Ramanan, S. R.; Bhosle, A. A.; Banerjee, M.; Chatterjee, A. *ACS Appl. Bio Mater.* **2021**, *4*, 1813–1822.
22. Khandare, D. G.; Joshi, H.; Banerjee, M.; Majik, M. S.; Chatterjee, A. *Anal. Chem.* **2015**, *87*, 10871–10877.
23. Naik, V. G.; Hiremath, S. D.; Das, A.; Banwari, D.; Gawas, R. U.; Biswas, M.; Banerjee, M.; Chatterjee, A. *Mater. Chem. Front.* **2018**, *2*, 2091–2097.
24. Feuer, G. in *Progress in Medicinal Chemistry*, eds. Ellis, G. P.; West, G. B. 1st edn, vol. 10 (North-Holland Publishing Company, New York, 1974), p. 85.
25. Liu, Y.; Ren, D.; Zhang, J.; Li, H.; Yang, X.-F. *Dyes Pigm.* **2019**, *162*, 112–119.
26. Lou, X.; Zhao, Z.; Hong, Y.; Dong, C.; Min, X.; Zhuang, Y.; Xu, X.; Jia, Y.; Xia, F.; Tang, B. Z. *Nanoscale* **2014**, *6*, 14691–14696.
27. Lehnert, A. L.; Kearfott, K. J. *Nucl. Technol.* **2010**, *172*, 325–334.
28. Chhatwal, M.; Mittal, R.; Gupta, R. D.; Awasthi, S. K. *J. Mater. Chem. C* **2018**, *6*, 12142–12158.
29. Singh, S. J. *Hazard. Mater.* **2007**, *144*, 15–28.
30. Moore, D. S. *Rev. Sci. Instrum.* **2004**, *75*, 2499–2512.
31. Zyryano, G. V.; Kopchuk, D. S.; Kovalev, I. S.; Nosova, E. V.; Rusinov, V. L.; Chupakhin, O. N. *Russ. Chem. Rev.* **2014**, *83*, 783.
32. Naik, V. G.; Hiremath, S. D.; Thakuri, A.; Hemmati, V.; Biswas, M.; Banerjee, M.; Chatterjee, A. *Analyst* **2022**, *147*, 2997–3006.
33. Parr, R. R.; Yang, R. G. *Density functional theory of atoms and molecules*, Oxford University Press: New York, 1989.
34. Jamorski, C.; Casida, M. E.; Salahub, D. R. *J. Phys. Chem.* **1996**, *104*, 5134–5147.
35. Qayyum, M.; Bushra, T.; Khan, Z. A.; Gul, H.; Majeed, S.; Yu, C.; Farooq, U.; Shaikh, A. J.; Shahzad, S. A. *ACS Omega* **2021**, *6*, 25447–25460.

	<p>Akhil A. Bhosle was born on 15th June 1995 in Goa, India. He has received his B.Sc. degree and M.Sc. degree in Chemistry in 2016 and 2018, respectively from Goa University. Later in January 2019 he joined the Department of Chemistry, BITS PILANI K K Birla Goa Campus, Goa, India as a Junior Research Fellow and is now pursuing his doctoral studies under the supervision of Prof. Mainak Banerjee and co-supervision of Prof. Amrita Chatterjee since August 2019. He developed several AIE-based molecular and supramolecular sensors and used mechanochemistry as the sustainable route for the synthesis of dyes and fluorophores.</p>
	<p>Dr. Mainak Banerjee was born in 1975 in Kolkata, India. He obtained his M.Sc. in Organic Chemistry from University of Calcutta in 1998. He received his PhD. degree in 2006 from Jadavpur University, Kolkata India. After two post-doc. stints in South Korea, he started his independent research career in 2009 as an Assistant Professor in the department of chemistry at BITS Pilani K K Birla Goa Campus. At present, he is a Professor in the same department. His current research interests include green chemistry, mechanochemistry, supramolecular chemistry, and chemical sensor.</p>
	<p>Viraj received his B.Sc. degree and M.Sc. degree in Chemistry in 2013 and 2016, respectively from Goa University. Subsequently, he joined the Department of Chemistry, BITS PILANI K K Birla Goa Campus, Goa, India as a Junior Research Fellow and has completed his doctoral studies (current status: thesis under evaluation) under the supervision of Prof. Amrita Chatterjee and co-supervision of Prof. Mainak Banerjee. He worked on tetraphenylethylene-based AIEgens as molecular sensors for the detection of variety of analytes during his doctoral studies. Currently, he is working as an ad-hoc lecturer in PES college, Ponda, Goa.</p>
	<p>Dr. Amrita Chatterjee was born in 1976 in Kolkata India. She obtained her Masters degree in Organic Chemistry from University of Calcutta in 2000 and PhD. degree in 2006 from Jadavpur University, Kolkata India. In 2006, she joined the group of Prof. Kyo Han Ahn's lab in POSTECH, and working in the area of the molecular sensor. In 2009, she joined BITS Pilani K K Birla Goa Campus as an Assistant Professor. Currently, she is a Professor at the same university. In her independent research career, she developed various molecular sensors (conventional dyes, AIE-based, carbon nanomaterial-based sensors) and focused on greener routes for the synthesis of the dyes and sensors.</p>

Application of nuclear technique for development of inhibitors for corrosion protection of different alloys

Jayashree Biswal^{1,2,*}, V. K. Sharma¹, H. J. Pant¹

¹Isotope and Radiation Application Division, Bhabha Atomic Research Centre
Trombay, Mumbai 400085, India

²Homi Bhabha National Institute, Anushakti Nagar, Mumbai 400094, India

*Email: jbiswal@barc.gov.in

Abstract

Corrosion is an unwanted phenomenon in oil and gas, petrochemical and other process industries and can cause significant economic loss to the industries. Thin layer activation analysis (TLA) is a nuclear technique widely used for corrosion monitoring of various industrial equipment. In the present article different corrosion inhibitors have been identified and tested for their efficacies in corrosion protection of bronze and carbon steel in acidic medium. In the first step, the alloy sample coupons were irradiated with proton beam of suitable energy to produce a small amount of radioactivity on their surfaces. Subsequently, the coupons were exposed to corrosive environment containing different type and concentrations of organic inhibitors. The corrosion was monitored by measuring loss of activity on the coupon by using a gamma spectrometer. The activity loss was correlated with the material loss by the help of a pre-generated calibration curve. The corrosion rates were estimated from the rate of material loss and the inhibitor efficiency was evaluated.

1. Introduction

Corrosion is an undesirable process responsible for a large loss of economy related to damage and maintenance costs. The oil and gas, petrochemical and other process-intensive plants are the major industries, which have to deal with the corrosion issues more frequently. Due to easy weldability, cost effective and shock resistant properties, carbon steel is a material of preference in pipelines in a number of industries [1,2]. However, the corrosion of carbon steel is a major problem in these industries. On the other hand, copper has a wide range of applications including heat exchanger tubing. Although, copper is generally resistant toward the influence of atmosphere and many mild chemicals, however, it is known that in aggressive media it is susceptible to corrosion. Corrosion monitoring in industry is essential due to one or more of following objectives: (i) for diagnosis of corrosion problems in operating device, (ii) to design suitable method or develop inhibitors for corrosion risk mitigation, (iii)

quality testing of lubricants and anticorrosive alloy, (iv) predict life of equipment and (v) facilitate scheduling of shutdowns. A number of conventional methods are available for corrosion monitoring in industrial equipment, however their applicability is limited to the complexity of corrosion process, accessibility of the part, in-situ measurements and sensitivity.

Thin layer activation analysis (TLA) is a well-established nuclear technique used for wear, corrosion and erosion monitoring of industrial components. It is a highly sensitive technique, faster, enables in-situ measurement (as well as ex-situ measurement) for monitoring corrosion process employing radioactive tracer [3-7]. This technique is well-suited for corrosion monitoring of a wide number of metals (and their alloys), such as, Mg, Al, Fe, Ti, V, Cr, Co, Ni, Mn, Cu, Zn, Cd, Ir, Pt, Pd, Au, Ta, Sn, Ti, Zr, Nb, Mo, Sn and W etc. Furthermore, the corrosion of non-metals can also be assessed by ultra-thin layer activation technique [5]. An important

feature of the technique is the low level of radioactivity involved in this technique, i.e, a few tens of micro Curie. This in turn removes elaborate safety arrangements during the testing. Due to these advantages TLA is a widespread method for wear and corrosion testing of a variety of materials. The methodology involves labeling the surface of a metallic component with desired radioactive isotope by irradiation with particle beams in a particle accelerator. The surface degradation of the labelled component is then monitored by measuring the remnant radioactivity on it using a gamma spectrometer.

Apart from monitoring the corrosion process, different means to control corrosion of industrial material is always a concern to plant engineers. The use of different types of inhibitors is a prudent approach for corrosion control of various metals and alloys. Amongst them there are inorganic inhibitors [8], but in much greater numbers there are organic compounds and their derivatives such as azoles [9-11], amines [12,13] and amino acids [14,15]. It is noticed that the presence of heteroatoms such as nitrogen, sulphur, phosphorous in the organic molecule improves its action as corrosion inhibitor. In the present study the corrosion inhibition of carbon steel (CS) and bronze have been studied by using two different organic inhibitors, such as, poly vinyl pyrrolidone (PVP) and hexamethylene tetramine (HMTA), respectively.

2. Principle of TLA technique

The overall principle of corrosion monitoring using TLA technique is depicted in Fig. 1. The technique employs irradiation of a metallic component with a beam of charged particles in an accelerator resulting in production of suitable radioisotope on the surface of the component. The radioactivity is confined to a circular area of 3-4 mmdiameter and 100-300 μm depth on the surface of the component. The irradiated

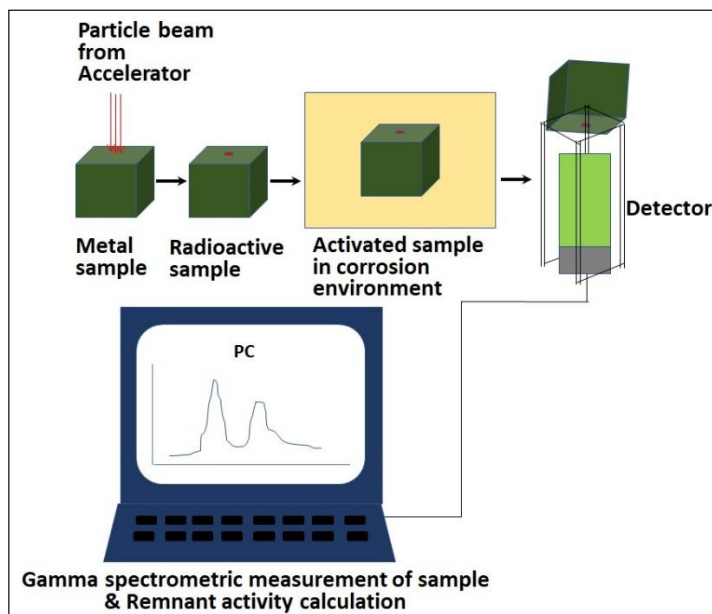


Fig 1. Principle of corrosion monitoring using TLA technique

component is subjected to chemical degradation in the corrosion media and the loss of material from the surface is estimated by measuring the residual radioactivity in the component. NaI(Tl) scintillation detector coupled with a multi-channel analyzer or HPGe detector coupled with a multi-channel analyser is used for measurement of activity. A calibration curve is generated by stacked foil irradiation under similar condition as that of the component. The residual activity in the component is converted to thickness loss with the help of the calibration curve. The thickness loss is plotted against time duration of corrosion and the corrosion rate is obtained from the slope of the plotted curve.

3. Experimental

3.1. Proton irradiation of samples

Bronze and carbon steel coupons of size $0.02\text{ m} \times 0.02\text{ m} \times 0.002\text{ m}$ each and two sets of stacked foils of iron and bronze were irradiated with proton beam at BARC-TIFR Pelletron accelerator facility at Mumbai. Bronze coupons and bronze stacked foils were irradiated with 11 MeV proton beam having beam current 200 nA for 4 hours. Similarly, CS coupons and pure iron stacked foils were irradiated with 13 MeV proton beam having

beam current 200 nA for 4 hours. The gamma spectra of the irradiated bronze and CS samples measured with a NaI(Tl) based spectrometer are shown in Fig 2. The radioactivity produced in these samples were estimated to be 190 – 400 kBq.

Iron (Fe) being the major element in the composition of CS, the radioisotope ^{56}Co is formed in irradiated CS coupon surface through nuclear reaction $^{56}\text{Fe}(p,n)^{56}\text{Co}$. The cross section and threshold energy of this nuclear reaction are 392 mb at 13 MeV and 5.44 MeV, respectively. The product isotope has half-life 77.3 days and gamma energies 847 KeV (100 %) and 1238 KeV(67 %). Throughout this study the 847 KeV peak was selected for activity measurement. Similarly, ^{65}Zn radioisotope is formed in irradiated bronze coupon surface through nuclear reaction $^{65}\text{Cu}(p,n)^{65}\text{Zn}$. The cross section and threshold energy of this nuclear reaction are 220 mb at 11 MeV and 2.2 MeV, respectively. The product isotope has half-life 244 days and gamma energy 1115 KeV (50 %).

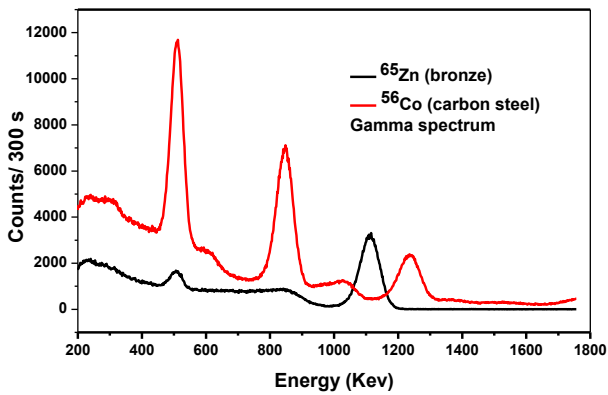


Fig 2. Gamma spectra of irradiated bronze and carbon steel samples

3.2. Determination of calibration curve

A stack of 15 bronze thin foils and iron thin foils were irradiated under similar conditions as that of the actual samples as mentioned in the previous section. The thickness of each bronze/iron foil was 25 μm . The remnant activity of the stacked foils was measured by removing one by one foil from the top (beam facing) by using

gamma spectrometer. The relative remnant activity (A/A_0) was calculated by dividing each measured counts (A) by initial counts (A_0). The calibration curve was obtained from the plot of remnant activity versus thickness removed. Fig 3 shows a typical calibration curve obtained by irradiating a stack of iron foils.

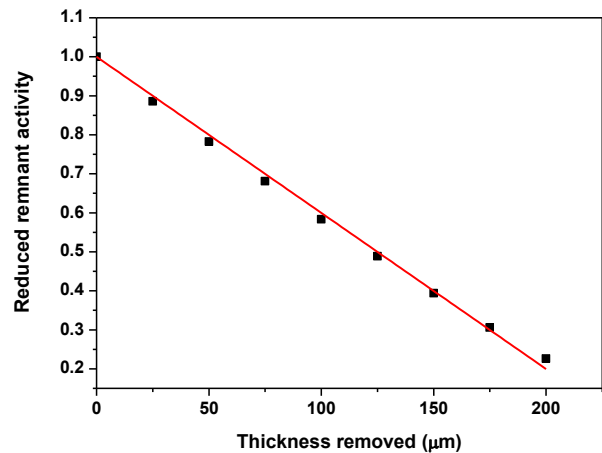


Fig 3. Calibration curve generated by stacked iron foil irradiation

3.3. Corrosion monitoring

The bronze corrosion was studied in a simulated acid rain solution containing $1.4 \times 10^{-3} \text{ mol dm}^{-3} \text{ Na}_2\text{SO}_4$, $2.4 \times 10^{-3} \text{ mol dm}^{-3} \text{ NaHCO}_3$. 0 to 300 ppm poly vinyl pyrrolidone (PVP) was added to the corrosion media as an inhibitor. After measurement of initial activity (A_0) in the irradiated coupon, the coupon was immersed in the corrosion media. The residual activity on the coupon was monitored intermittently by removing the coupon from the solution. The activity was measured at a fixed geometry with respect to the detector and the counts were recorded for a specific time. A relative residual activity was calculated as mentioned in section 3.2.

The corrosion of CS was measured in 1 mol dm^{-3} aqueous HCl solution under ambient condition and hexamethylene tetramine (HMTA) in the concentration range 0-1000 ppm was used as inhibitor. Similar procedure was adopted for estimation of relative residual activity of CS as above.

4. Results and discussion

Organic molecules having hetero atom in functional group have great potential to act as corrosion inhibitor for metallic structures. Organic inhibitors generally are of low cost and they form a protective layer on the metallic surface via chemisorption or physisorption thereby blocking the reaction sites on the surface. As a result, the corrosion of the metallic structure is slowed down. Both PVP and HMTA have electron donating nitrogen atoms, which can contribute to formation of covalent bond on CS and bronze surfaces, respectively.

As the rate of corrosion is a direct measure of material loss, similarly the effectiveness of a corrosion inhibitor is expressed in terms of the inhibition efficiency (η) (Eq (1)).

$$\eta(\%) = \frac{(r_0 - r_i)}{r_0} \times 100 \quad (1)$$

Where, r_0 and r_i are rate of corrosion in absence and rate of corrosion in presence of inhibitor, respectively.

4.1. Corrosion monitoring of bronze

The rate of corrosion of bronze in absence of and in presence of PVP (200 ppm) at ambient condition was measured to be 194.33 and 38.46 nm/h, respectively. The results of the study showed that, 200 ppm concentration of PVP is

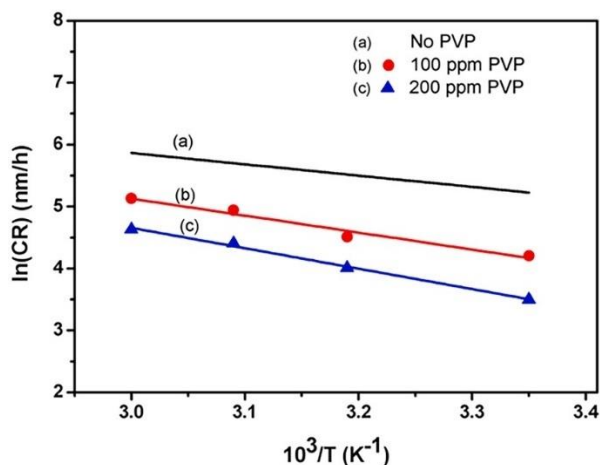


Fig 4. Variation of corrosion rate of bronze in acid rain with reciprocal of Temperature at different PVP concentration

sufficient to control the corrosion of bronze in acidic environment with an inhibition efficiency of 80.2 %. The rate of corrosion was found to be decreasing with increase in concentration of PVP, whereas, it increases with increase in solution temperature as shown in Fig 4.

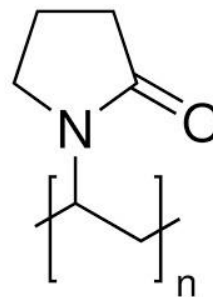


Fig 5. Molecular structure of polyvinyl pyrrolidone

The molecular structure of polyvinyl pyrrolidone is shown in Fig 5. PVP being amphiphilic in nature, it has a hydrophilic moiety (ring having heteroatoms), which interacts with the metal surface and a hydrophobic polymeric chain protruding toward the bulk solution. Due to these interactions PVP forms a protective film on metal surface by adsorption hence prevent the interaction of corrosive acids/ chemicals present in the environment/ moisture with metal. In addition to this the adsorbed PVP inhibitor molecules limit oxygen diffusion and the water access to the metal surface, so reducing the corrosion rate.

4.2. Corrosion monitoring of carbon steel in presence of HMTA

The corrosion rate of CS was monitored in the HMTA concentration range 0 to 1000 ppm at room temperature and the plot rate of corrosion with HMTA concentration is shown in Fig 6. A significant decrease in corrosion rate was observed in presence of 80 ppm of HMTA than in absence of the corrosion inhibitor. The CR is decreased from 1177.8 nm/h to 259.8 nm/h in absence and in presence (80 ppm) of HMTA, respectively. The corrosion rate is minimum for 500 ppm HMTA with η value 89.8 %. There is no significant decrease in the corrosion rate for

HMTA concentration above 500 ppm. The study suggested that 300-500 ppm HMTA concentration can be used to achieve adequate inhibition efficiency in corrosion protection of CS in acid medium.

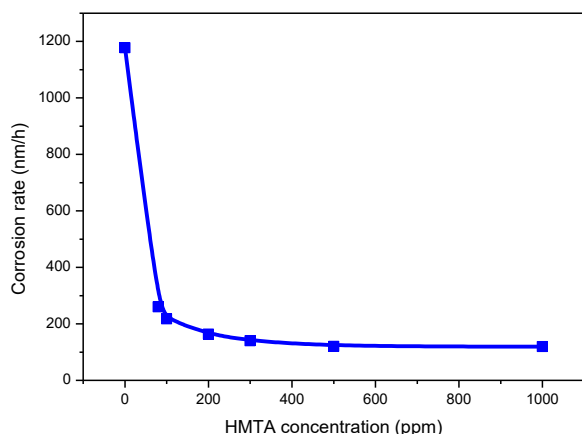


Fig 6. Variation of corrosion rate of carbon steel with HMTA concentration

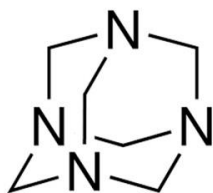


Fig 7. Molecular structure of hexamethylene tetramine

HMTA is a heterocyclic organic compound with tetrahedron cage like structure as shown in Fig. 7. The functional group, i.e., nitrogen atoms contain lone pair of electrons, which forms coordination bond with metal atoms on the metal surface. Moreover, HMTA is soluble in water as well as other organic solvents and stable at relatively high temperature. Due to these properties, HMTA could effectively play as an inhibitor for acid corrosion of carbon steel.

5. Conclusions

The thin layer activation analysis technique has been developed and standardized in Isotope and Radiation Applications Division and applied for monitoring corrosion processes of different

alloys. Small organic molecules containing heteroatoms were tested for corrosion inhibition of bronze and carbon steel using this technique. About 200 ppm concentration of polyvinyl pyrrolidone was observed to effectively control the corrosion of bronze in simulated acid rain with an inhibition efficiency of 80.2 %. Similarly, hexamethylenetetramine was demonstrated to be an effective corrosion inhibitor to control acid corrosion in carbon steel. The corrosion rate was minimum for 500 ppm HMTA with an inhibition efficiency 89.8 %. The study established that the TLA technique has the potential for solving wear and corrosion problems in various industries.

Acknowledgements

The authors are thankful to Shri. S. C. Sharma, Dr. A. K. Gupta and staffs at Pelletron Accelerator facility for their supervision and support in irradiation of various samples in the accelerator.

References

1. J. Enani, *Int. J. Sci. Eng. Res.* **2016**, 7, 1161–1164.
2. J. Kiefner, C. Trench, **2001**, Penspen Integrity, United Kingdom.
3. The thin layer activation method and its applications in industry. IAEA-TECDOC-924, **1997**, Vienna, Austria.
4. D. P. Chowdhury, J. Datta, and A. V. Reddy, *Radiochim. Acta.*, **2012**, 100, 139-145.
5. I.O. Konstantinov, N.N. Krasnov, *J. Radioanal. Chem.*, **1971**, 8, 357-371.
6. R. Evans, *Wear*, **1980**, 64, 311-325.
7. T.W. Conlon, *Contemp. Phys.*, **1982**, 23, 353-369.
8. A. Igual Muñoz, J. García Antón, J.L. Guiñón, V. Pérez Herranz, *Electrochimica Acta*, **2004**, 50, 957.
9. D-Q. Zhang, L-X. Gao, G-D. Zhou, *J. Appl. Electrochem.*, **2003**, 33, 361.
10. R.F.V. Villamil, G.G.O. Cordeiro, J. Matos, E.D'Elia, S.M.L. Agostinho, *Mater. Chem. Phys.*, **2002**, 78, 448.
11. J. Bartley, N. Huynh, S.E. Bottle, H. Flitt, T. Notoya, D.P. Schweinsberg, *Corros. Sci.*, **2003**, 45, 81.
12. E. Stupnisek-Lisac, A. Brnada, A.D. Mance, *Corros. Sci.*, **2000**, 42, 243.
13. H. Ma, S. Chen, L. Niu, S. Zhao, S. Li, D. Li, *J. Appl. Electrochem.*, **2002**, 32, 65.
14. J.B. Matos, L.P. Pereira, S.M.L. Agostinho, O.E. Barcia, G.G.O. Cordeiro, E.D'Elia, *J. Appl. Electrochem.*, **2004**, 570, 91.
15. G. Moretti, F. Guidi, *Corros. Sci.*, **2002**, 44, 1995.



Dr. Jayashree Biswal is Scientific Officer in Bhabha Atomic Research Centre and Assistant Professor in Homi Bhabha National Institute (HBNI), Mumbai. She received her PhD (Chemistry) from HBNI in 2013. Her research interest includes process optimization and evaluation of design of industrial chemical reactors by employing radioisotope techniques, development and application of various radiotracer techniques for flow measurement and troubleshooting in industrial systems; and wear and corrosion rate measurements of industrial components by ion beam technique. She has published about 35 papers in international journals.

Radiation-induced synthesis of semiconductor nanoparticles in aqueous solution – a promising method

A. Guleria and M. C. Rath

Radiation & Photochemistry Division, Bhabha Atomic Research Centre, Mumbai 400085

Homi Bhabha National Institute, Trombay, Mumbai 400094, India

Email: aguleria@barc.gov.in (AG), madhab@barc.gov.in (MCR)

Abstract

The field of nanotechnology has witnessed significant advancements in recent years, and undoubtedly, nanomaterials, particularly those derived from semiconductors, are anticipated to play a significant role across multiple facets of our daily lives. However, there remains a lack of cost-effective, environmentally friendly, easily scalable, and time-efficient methods for creating semiconductor nanomaterials while precisely controlling their morphology *vis-à-vis* properties. From this perspective, employing radiation-based approach may address these concerns. The article begins with an introduction to semiconductor nanoparticles, quantum confinement, and their general synthetic methodologies. Following this, it provides an outline of the use of high-energy ionizing radiations (like e-beams, γ -rays) in manufacturing semiconductor nanomaterials, particularly Si and II-VI metal chalcogenides, focusing primarily on their optical attributes. The core principle in radiation-assisted synthetic approach lies in the radiolysis of solvent, and subsequent reactions between the resulting radicals/intermediates and dissolved precursor compounds. Consequently, a brief discourse is presented on radiolysis and the proficient utilization of *in-situ* generated radicals to synthesize CdSe nanoparticles (as an illustrative example). The mechanism behind the formation of CdSe nanoparticles on irradiation of samples containing precursors has been succinctly elucidated. Furthermore, the radiolytic synthesis of another semiconductor-based nanomaterial, i.e., silicon (Si) has been described. The role of various experimental parameters, notably absorbed dose, dose rate, and capping agent, on the photoluminescence properties of Si-based nanomaterials has been discussed. Lastly, the article highlights the future prospects concerning nanomaterial synthesis through radiolytic approach.

1. Introduction

Nanomaterials exhibit distinct characteristics compared to bulk materials, primarily owing to their unique physicochemical properties encompassing mechanical, optical, thermal, magnetic, biological, electrical, and chemical traits, emerging at the nanoscale due to quantum effects [1-5]. Moreover, high surface area-to-volume ratio is one of the main characteristics of materials at nanoscale dimensions. It's undeniable that over the past three decades, nanotechnology has experienced remarkable progress and growth in terms of innovation and advancement [1-5].

Nanomaterials, especially semiconductor-based ones, are poised to revolutionize numerous sectors, including energy, healthcare, and the environment, in the near future [1-7]. Semiconductor materials could be of direct or indirect band gap type. In the case of a direct band gap, the carriers (electrons and holes) are generated by the absorption of a photon ($h\nu$) following the selection rule $\Delta k = 0$ (where 'k' is the wave vector). However, in the case of an indirect band gap, the generation of charge carriers is facilitated by the combination of photon absorption ($h\nu$) and phonon interaction ($h\omega$), as the two band minima do not occur at the

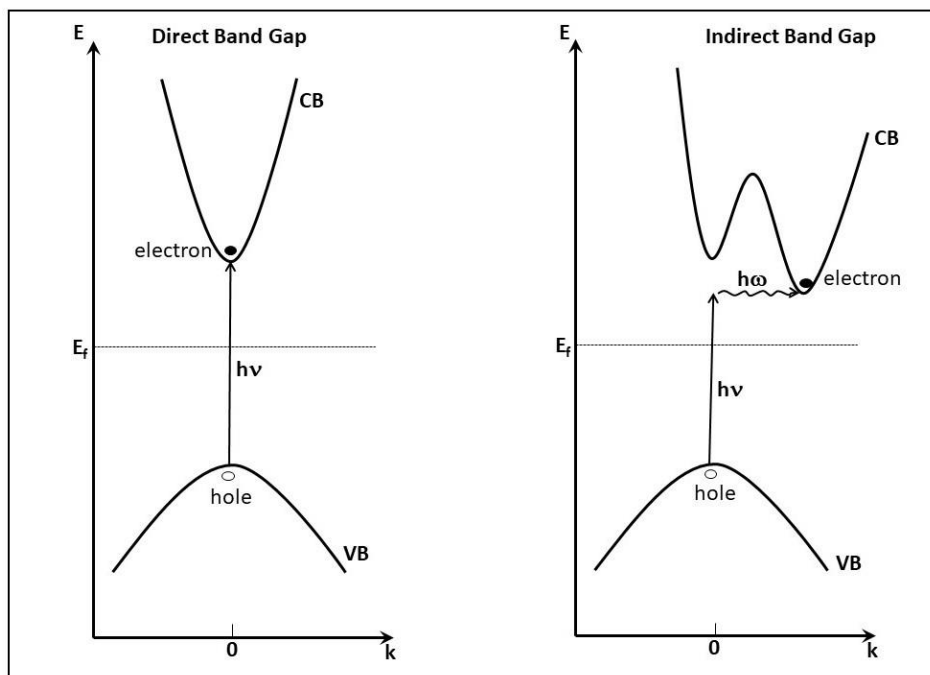


FIG. 1. Energy band diagram for direct and indirect band gap type semiconductors.

same k value as in the case of a direct band gap type (see Fig. 1 below).

Most II-VI semiconductors belong to the direct band-gap type, whereas most III-VI semiconductors exhibit an indirect band-gap type. In contrast, IV-VI semiconductors show a mixed type. Silicon and germanium are examples of semiconductors with an indirect band gap. These common semiconductors and their respective band gap natures and energy values are mentioned in Table 1. This article primarily discusses radiation-assisted synthesis related to II-VI semiconductor nanomaterials in aqueous media. It also provides a concise overview of radiation-assisted synthesis of silicon (Si)-based nanomaterials.

Nanoparticles could be of different shapes and sizes, such as nanoflakes, nanorods, nanotubes, nanoflowers, nanoseaurchins,

nanopetals etc. However, when the size (D_x) of semiconductor nanoparticles decreases below a certain size, i.e., the de Broglie wavelength of charge carriers (λ), a quantization effect occurs

Table 1. Type of band gap and band gap energy values of common semiconductors

Material	Type of Band gap	Band gap energy (eV) at 300 K
Si	Indirect	1.12
Ge	Indirect	0.66
ZnS	Direct	3.54
ZnSe	Direct	2.58
ZnTe	Direct	2.25
CdSe	Direct	1.74
CdS	Direct	2.42
CdTe	Direct	1.5
InP	Direct	1.35
InAs	Direct	0.36
GaAs	Direct	1.42
PbSe	Direct	0.27
PbS	Direct	0.37
PbTe	Direct	0.29

in the nanoparticles (see equation (1)). At this point, nanoparticles are called as quantum dots, showcasing a quantum confinement of the charge carriers [1-9].

$$\Delta x \approx \lambda = \frac{h}{p} = \frac{h}{\sqrt{mE}} \quad (1)$$

Alternatively, when the size of nanoparticles becomes equal to or less than the Bohr radius of the exciton, they are also referred to as quantum dots, experiencing a quantization effect in the valence and conduction bands. The exciton formed in the case of semiconductors has a dimension that is spread over a number of lattice points and moves freely within the lattice space, unlike in the case of insulators where the exciton is tightly bound to a fixed lattice point. Therefore, when the size of the semiconductor reduces below the Bohr radius of exciton, the movement of excitons is highly restricted due to the confinement in all three dimensional space. Similarly, when there is a confinement in two dimensions, then the exciton gets confined in those two dimensions and has a free movement only in the other dimension. In such a situation, the nanomaterials are called as quantum rods. In the case of a size confinement only in one dimension, the exciton has lost its freedom in one dimension and free to move in other two dimensions [1-9]. In this situation, when a semiconductor of lower band gap gets sandwiched by two other semiconductors of higher band gap, such kind of materials are called as quantum well structures (Fig. 2).

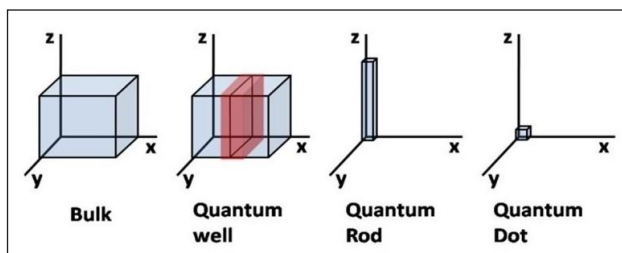


FIG. 2. Confinement in semiconductors.

This confinement leads to the quantization effect in their conduction and valence bands. Conduction band gets splitted into different quantized levels as represented either by 1, 2,

3 and so on or by the atomic orbitals, 1S, 2S, 2P etc. Similarly, valence band gets splitted into heavy hole and light hole bands (Fig. 3). Thus quantization effect is clearly observed in their structured pattern of the optical absorption spectrum.

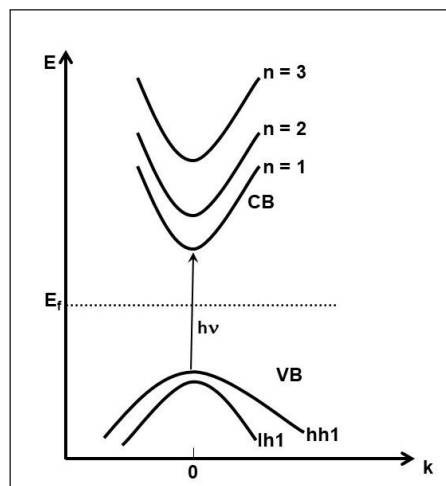


FIG. 3. Quantization effect in direct band gap type semiconductors.

Fig. 4 gives an artistic representation of quantum dots dispersed in a colloidal solution inside a cuvette. The colloidal particle sizes are often measured by dynamic light scattering and optical absorption spectra measurements.

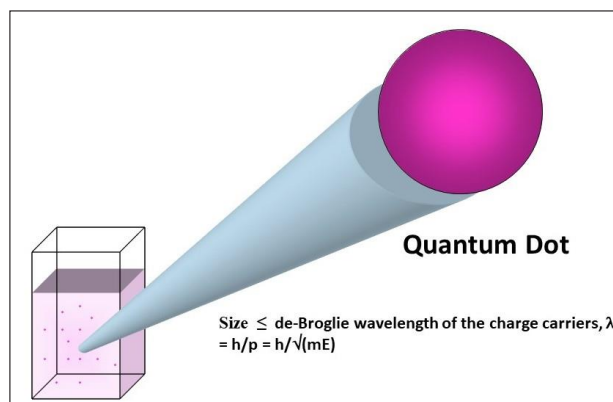


FIG. 4. An artistic representation of semiconductor quantum dots in colloidal solution inside a cuvette.

The semiconductor nanoparticles are synthesized by various methods [1-9] as shown below in Fig. 5.

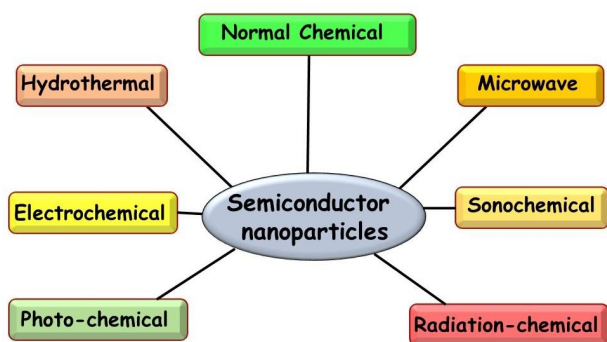


FIG. 5. Various synthesis methods of semiconductor nanoparticles

2. Radiation-assisted synthesis approach

Developing a sustainable and eco-friendly protocol for the synthesis of nanomaterials is crucial, aiming to minimize the use of corrosive, flammable reagents, and toxic/hazardous chemicals, such as reducing and capping agents. In this context, radiation-assisted synthesis (e.g., e-beam, γ -ray) of nanomaterials emerges as a potent and efficient method, eliminating the need for stringent laboratory conditions like high temperature and additional chemical reagents to initiate the synthesis reaction. Moreover, this approach presents numerous advantages, including a one-step synthesis, clean synthesis, scalability, *in situ* generation of reducing species (such as solvated electron, e^-_{sol}), and cost-effectiveness [10-25]. The nucleation and growth processes of the nanoparticles can be conveniently controlled by the suitable choice of the experimental conditions (e.g., absorbed dose and the dose rate).

By varying the structural and the fluidic aspects of the host matrix, its templating properties can be used to direct the formation of nanoparticles with desirable shapes and

sizes. In the radiation chemical route, synthesis is mostly carried out in aqueous solution. Thus, the primary event is the radiolysis of water, generating various free radicals that drive the radiation-induced synthesis. Radiolysis of water can occur through interactions with high-energy electromagnetic radiations such as gamma, synchrotron, and X-rays, as well as high-energy particle radiations like electrons, protons, and other ion beams (see Fig. 6) [26-28]. However, free radicals can also be generated through the interaction of light photons, a process known as photochemical routes. Therefore, both radiation chemical and photochemical routes are considered complementary to each other. However, in the latter case, the process is significantly slower compared to the former due to altogether different way of formation of free radicals. In photochemical routes, free radicals

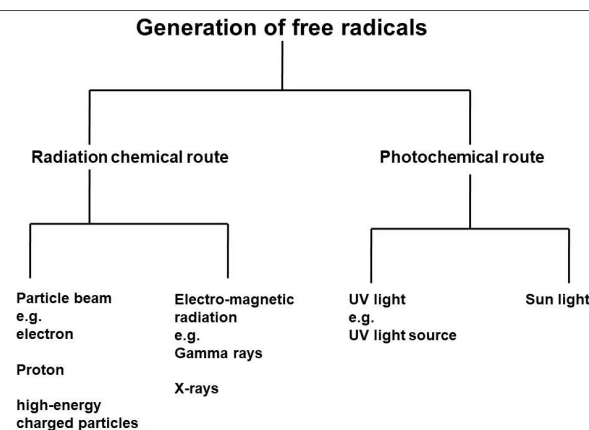


FIG. 6. Generation of free radicals by various types of radiations.

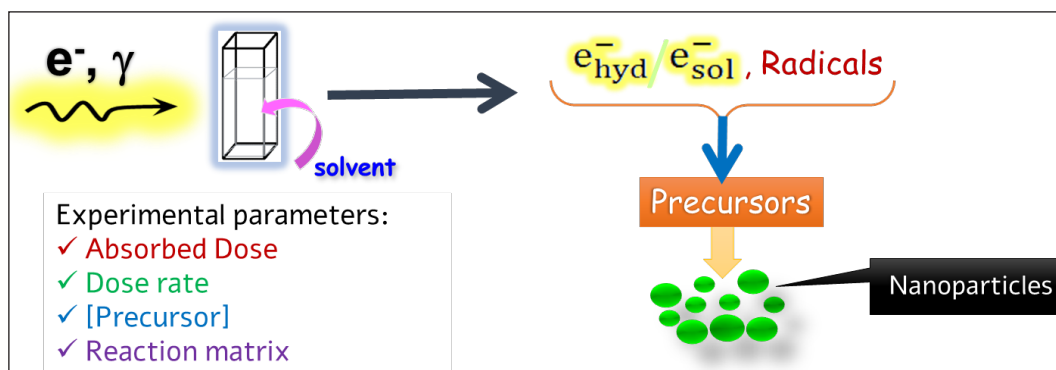


FIG 7. Diagrammatic depiction of a general scenario representing the radiation (e^- , γ) induced synthesis of nanomaterials.

are produced through the photo-excitation pathway of a specific solute or solvent. In contrast, in radiation chemical routes, free radicals are directly generated by the strong interaction between high-energy radiations and the solvent [26-28]. Nevertheless, in certain cases, free radicals produced through the interaction of light photons are considered to be very important.

In this chapter, our focus will be solely on discussing the synthesis of semiconductor nanoparticles using the radiation chemical method. Fig. 7 illustrates a diagrammatic representation of the general scenario involving the radiation-induced synthesis of nanomaterials.

3. Radiation-assisted synthesis of semiconductor nanoparticles

3.1. II-VI metal chalcogenides nanomaterials (CdSe: A case study)

Semiconductor nanoparticles, specifically those of compound-type semiconductors mainly consisting of group II and VI elements, recognized as II-VI semiconductors (also known as metal chalcogenides)—have been synthesized using radiation chemical route (see Fig.8 below) [13,16,24]. These are bipolar in nature and bound with ionic bond, however possess very low solubility product, rendering them insoluble in water. Apart from II-VI semiconductors, radiation induced synthesis of IV-VI semiconductor nanoparticles is also reported in the literature [29,30]. However, the preparation of III-V semiconductor nanoparticles via the radiation route in aqueous media remains sparsely reported to date. This limitation stems from

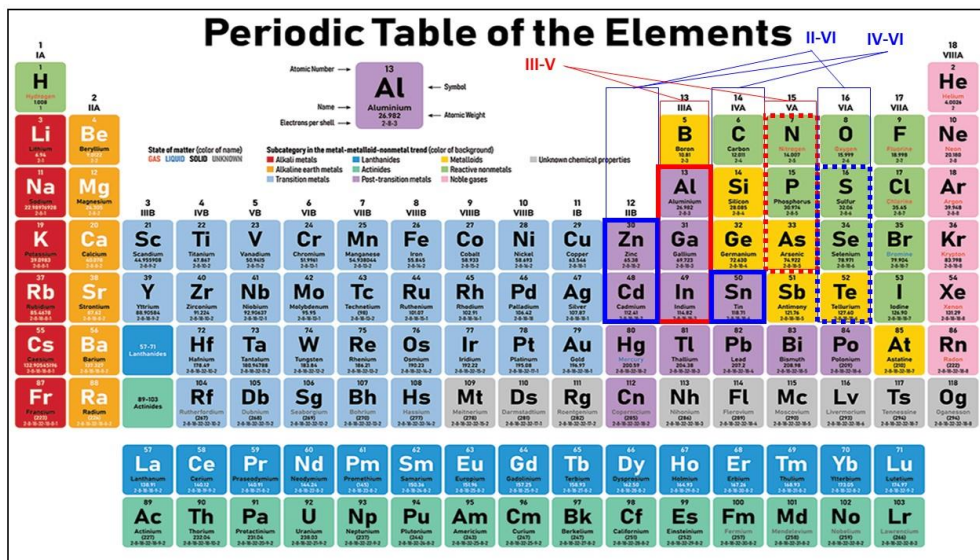


FIG. 8. II-VI, III-V and IV-VI type semiconductors are shown in the periodic table of elements

the fact that in radiation-induced synthesis, the precursor reagents are usually taken in aqueous media, making their solubility in water a critical factor due to the synthesis process relying on free radicals generated during water radiolysis. Therefore, finding out a suitable water soluble precursor becomes important in the radiation-induced synthesis of semiconductor nanoparticles. However, researchers are engaged in finding out suitable reagents to synthesize various types of semiconductor nanoparticles of interest.

As previously mentioned, II-VI metal chalcogenides nanomaterials (like CdSe, CdS, ZnSe, ZnS etc.) have found application across various emerging fields like sensors, photo-voltaics, LED and many others[1-9]. Their energy band gap values typically range from 1 to 3 eV, falling within the visible region. These materials are synthesized or grown using both top-down as well as bottom-up approaches [1-9]. Bottom-up approaches are easier to operate and less complicated as compared to top-down approaches. In bottom-up approaches various chemical methods are used, however, radiation induced method is one of the most efficient and considered to be environmental friendly. High-energy ionizing radiations like Cobalt-60

gamma radiation, X-rays, synchrotron radiation, and high-energy particle radiations like electron beam, proton beam and other ion beams are often used for the generation of free radicals during the synthesis [10-25]. Water-soluble precursors are utilized in different molar ratios and subjected to irradiation, leading to the formation of corresponding semiconductor nanoparticles. To achieve desired sizes and shapes, suitable capping agents are introduced alongside the precursors in the reaction mixture. Among these, sulfur-containing compounds are preferred due to the high affinity of cadmium and zinc towards sulfur. However, in certain cases, soft templates like micelles and microemulsions are also used for a desired size and shape of the nanoparticles. The detailed discussions about each of these nanoparticles are provided in the subsequent sections.

Radiation induced synthesis of CdSe nanoparticles has been investigated quite extensively in the recent past by various researchers and scientists [24,31,32]. Its synthesis requires aqueous soluble precursors of cadmium and selenium. Usually cadmium ions are complexed with either ammonia or other complexing agents for its slow release otherwise there won't be the formation of nanoparticles. Fig. 9 demonstrates the formation of water soluble cadmium complex with ammonia and the structure of tetraamine cadmium complex. Similarly, selenium is used in the form of either selenosulfate or selenite, however, the former one is more preferred precursor. It is normally synthesized through the refluxing of sodium sulfite and selenium powder at 70°C for about 7 hrs. A clear transparent solution containing Na_2SeSO_3 is obtained which is used as the precursor for selenium. Selenosulfate ions are analogous to thiosulfate and sulfate ions, and the bond length between sulfur-oxygen, sulfur-sulfur and sulfur-selenium increase in the order, $\text{S-O} < \text{S-S} < \text{S-Se}$, as shown in the Fig. 10 below. This characteristic facilitates the improved release of Se from the complex ion for the formation of CdSe.

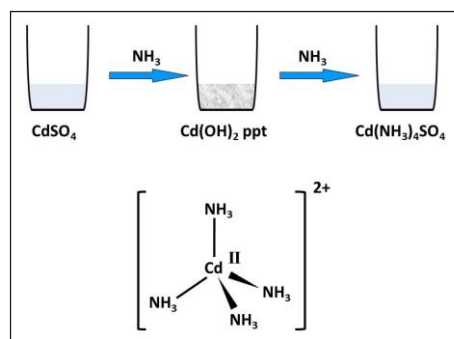


FIG. 9. Schematic representations of the preparation of water soluble cadmium complex with ammonia.

CdSe nanoparticles have diverse applications, mainly due to their ability to exhibit strong photoluminescence at room temperature (see Fig. 11). While the synthesis method plays a crucial role in determining their applicability, the major uses are often independent of specific synthesis routes. The radiation-induced synthesis route produces high-quality CdSe nanoparticles with a broad range of applications.

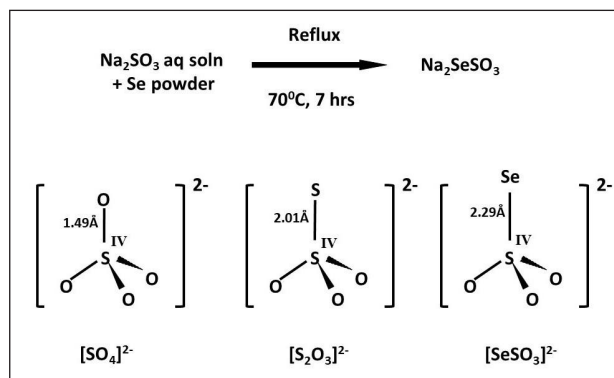


FIG. 10. Analogous 3D sketch of SO_4^{2-} , $\text{S}_2\text{O}_3^{2-}$ and SeSO_3^{2-} ions.

Cadmium precursor, tetraamine cadmium sulfate and selenium precursor, sodium selenosulfate are taken in aqueous solution in very low concentration to avoid self reaction between them. Tert-butanol is added to the reaction mixture to quench $\cdot\text{OH}$ radicals and create a reducing environment in the system during the irradiation. Because the radiolytic synthesis of II-VI compound semiconductor nanoparticles are synthesized via a reduction reaction pathway involving reducing free

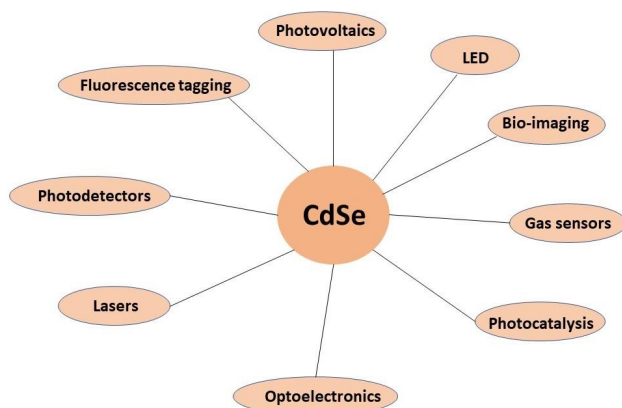
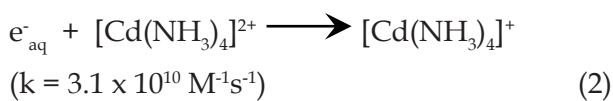


FIG. 11. Applications of CdSe nanoparticles in different fields.

radicals like hydrated electron, H atom or other secondary radicals like those generated from various alcohols.

The irradiation experiments are usually done in Cobalt-60 gamma chamber or high-energy (e.g. 7 MeV) electron accelerator. The total absorbed dose (in kGy) is usually estimated from the radiation chemical yield of the free radicals involved in the reaction and the initial concentration of the precursors. The clear transparent solution turns orange coloured solution after irradiation indicates the formation of CdSe nanoparticles which is further confirmed from XRD, FTIR and Raman spectroscopic measurements. Following are the most probable reactions those occur during the irradiation

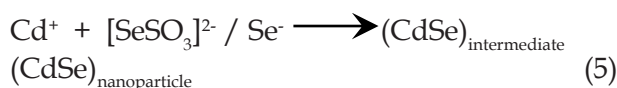


$(SeSO_3)^{2-}$ ions are analogous to $(S_2O_3)^{2-}$ ions, where S^- transient ions are released along with SO_3^{2-} ion from $(S_2O_3)^{2-}$ ions upon radiolysis. So similar reaction could be occurring in the case of $[SeSO_3]^{2-}$ ions as shown in the reaction (3) above.



Cd^+ or $[Cd(NH_3)_4]^+$ ions can react with $[SeSO_3]^{2-}$ and/or Se^- transient ions to form nascent

$CdSe$ molecular species (named as $(CdSe)_{intermediate}$) which will undergo nucleation and growth to form CdSe nanoparticles. Various other reactions such as radical-radical, radical-other ionic species like Cd^{2+} , Cd^+ , $[SeSO_3]^{2-}$, $[SeSO_3]^-$, etc might also be happening in this case. However, the most predominate reaction leading to the formation of CdSe nanoparticles is represented in the reaction (5) below. The appearance of an orange coloured sol was found only when both the precursors are present and in a reducing environment. This explains that formation of CdSe nanoparticles takes place through a reduction reaction pathway as mentioned here.



From the above reaction pathways, the formation of one CdSe molecular species requires two reducing radicals, i.e. e^-_{aq} and therefore a total of 20 mM e^-_{aq} will be required for a complete conversion. By the taking the G-value for e^-_{aq} as 0.28 $\mu\text{M}/\text{J}$, the precursor concentration as 10 mM and considering a complete conversion, the total absorbed dose required for the synthesis of CdSe nanoparticles will be around 71 kGy, with an assumption that there won't be any other reactions apart from those mentioned above. However, in practical, there might be some other reactions might be happening during the irradiation. Therefore, it is always better to give a slight higher absorbed than calculated value for a complete conversion. The complete conversion can be easily monitored by measuring the concentration of individual precursors in the supernatant.

The formation of CdSe nanoparticles through a reduction reaction pathway is also established by observing the effect of N_2O saturation (saturated concentration 25 mM) in the reaction mixture [33]. It is known that N_2O quenches e^-_{aq} to form $\cdot\text{OH}$ radicals. There will be a competition reaction of e^-_{aq} with N_2O to form $\cdot\text{OH}$ radicals and with $[Cd(NH_3)_4]^{2+}$ to form $[Cd(NH_3)_4]^+$ ions. Hence, there will be reduction in the yield of formed CdSe nanoparticles. It is

observed that the ratio of the yields of formation of these nanoparticles in the absence and presence of N₂O was about 100:60. Furthermore, it was observed that there was a formation of CdSe nanoparticles even in a very low concentration of precursors (0.5 mM) under a de-aerated condition, whereas there was no formation found under a N₂O saturated condition. Fig. 12 clearly shows the appearance of an absorption peak at around 560 nm, which is absent in all other cases, which indicates that there is formation of CdSe nanoparticles in the reaction mixture upon irradiation. The extended absorption beyond the peak indicates a broad size distribution and trap states present in these nanoparticles. In this case, as there was not any capping agents to arrest the further growth of the nanoparticles, there was an agglomeration of the nanoparticles. The size of primary nanoparticles can be calculated using Brus equation below.

$$E_g = E_g(0) + \frac{\alpha}{d^2} \quad (5)$$

where, $\alpha = 3.7 \text{ eV nm}^2$, $E_g(0) = 1.7 \text{ eV}$, d is the particle size (nm) and E_g is the band gap value in eV. The band gap (E_g) values were determined from the Tauc plot of $(\alpha' hv)^2$ versus hv , as this is a direct band gap semiconductor. The symbol ' α ' represents the absorption co-efficient multiplied with the concentration of the CdSe QDs and is equivalent to the relation $(2.303 A/l)$, where ' A '

is the absorbance and ' l ' is the optical path length of the cell (10 mm). The term ' $h\nu$ ' represents the photon energy. The size calculated from this equation from the above absorption spectra was about 3 – 5nm. The Bohr radius of exciton in the case of CdSe is 5.7 nm, and hence such nanoparticles can also be called CdSe quantum dots. The molar extinction coefficient of CdSe nanoparticles at 560 nm in methanol was found to be $1.3 \times 10^4 \text{ M}^{-1}\text{cm}^{-1}$.

The XRD patterns (Fig. 13) obtained for CdSe nanoparticles synthesized by Co-60 gamma and electron beam irradiation confirms their formation. The broadening of the peaks indicates the nanosize particles as well as the amorphous nature of these particles. The particle size is calculated from the XRD peaks using Scherrer's formula or modified formula.

$$d = \frac{0.9 \lambda}{\beta \text{Cos}\theta} \quad (6)$$

where, d is the particle size (nm), λ is the wavelength of the X-ray, 1.504 \AA , β is the FWHM of the XRD peak and θ is the angle of XRD peak position in degree. The sizes calculated from this equation matches well within an acceptable error of around 10 %.

$$\frac{\beta \text{Cos}\theta}{\lambda} = \frac{1}{d} + \frac{\eta \text{Sin}\theta}{\lambda} \quad (7)$$

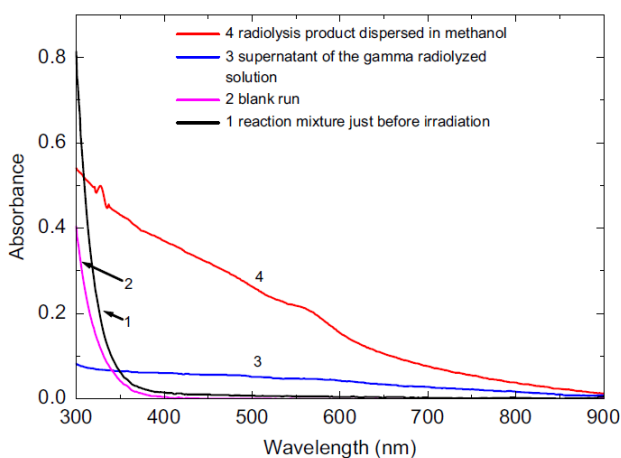


FIG. 12. Optical absorption spectra of unirradiated and irradiated solution containing 10 mM each precursor, ammoniated cadmium sulfate and sodium selenosulfate [24].

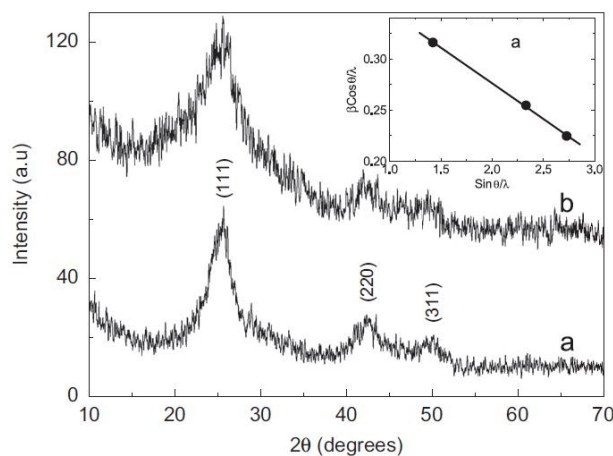


FIG. 13. XRD patterns obtained for the CdSe nanoparticles obtained in the Co-60 gamma irradiation (a) and electron beam irradiation (b)[24].

Where, η is the effective strain in the nanoparticles and other terms as described for the equation (6) above. A negative strain found in this case as seen from the inset of Fig. 13 indicates a compressive strain in these nanoparticles. A similar observation was found in the radiation induced ZnO nanoparticles as reported by Rath et al and not to be attributed to the radiation induced synthesis method [24]. The particle sizes match with those obtained from the optical absorption spectral analysis. However, the sizes in the case of nanoparticles obtained via electron beam irradiation are smaller as compared to those obtained in the gamma irradiation. A similar observation can be observed from their TEM images (Fig. 14). The primary nanoparticles are observed to get agglomerated into somewhat bigger sizes, as there was no capping agent used in this synthesis. Nevertheless, in the presence of a suitable capping agent such agglomeration won't occur. The SAED patterns in the inset of the TEM images indicates a cubic phase of CdSe nanoparticles.

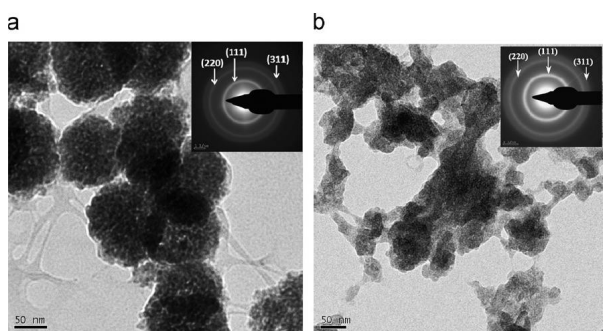


FIG. 14. TEM images obtained for the CdSe nanoparticles obtained in the Co-60 gamma irradiation (a) and electron beam irradiation (b) [24].

These CdSe nanoparticles are found to have ferromagnetic behaviour as seen from the hysteresis loop in their room temperature magnetization measurements [24]. The higher saturation magnetization value in the case of samples obtained via electron beam irradiation is due to the smaller particle size in this case as compared to that obtained in the gamma irradiation. Such a behaviour of the semiconductor nanoparticles is attributed to the unsaturated

surface states. The surface layer of the bare CdSe nanoparticles in this case mainly consists of Cd^{2+} and SeO_2 on aerial oxidation. This leads to the presence of surface defect states and surface unsaturation in these nanoparticles. A long tail in their optical absorption spectra is also due to the existence of such surface defect states, and it is inherent to the method of synthesis. Room temperature ferromagnetic behaviour in TOPO capped CdSe nanoparticles was also reported by Taylor et al. [24] on the basis of surface states. In these nanoparticles, the surface stoichiometry is 70 % Cd and 30 % Se and intrinsic to the high temperature synthesis route. The metal to ligand charge transfer process in the surface of these capped CdSe nanoparticles produces vacancy in the d-orbital of Cd atom which is the origin of such room temperature ferromagnetic behaviour in these nanoparticles. It is seen that the CdSe nanoparticles synthesized via radiation chemical route possess a better room temperature ferromagnetic behaviour as compared to those synthesized via hydrothermal routes using TOPO and TOP capping agents. However, CdSe nanoparticles synthesized either via hydrothermal route or solvothermal route are known to possess sharp excitonic absorption peaks, which is lacking in the case of radiation chemical route. Such a sharp excitonic absorption (Fig. 15)

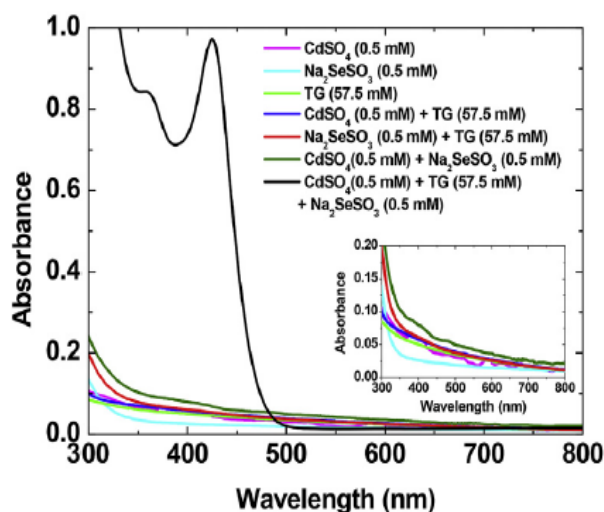


FIG. 15. Optical absorption spectra of different reagents, along with an intense absorption due to the CdSe nanoparticles in aqueous solution [34].

characteristics was also observed in the CdSe nanoparticles synthesized at room temperature through normal chemical route using thioglycerol as a reducing as well as capping agent [34]. It clearly confirms the presence of a strong capping agent forms bond with the surface unsaturated ions and thereby remove the surface defect states to a large extent.

3.2. Si-based nanomaterials

Of late, our group has reported the synthesis of Si-based nanomaterials using γ -rays as well as electron-beam irradiation in aqueous media [17-21]. Interestingly, the silicon nanomaterials obtained comprised of unique features (such as amorphous and porous characteristics), which otherwise require meticulous synthetic

procedures via conventional methodologies. The highlights of the research work carried out in this regard are presented in brief in the following sections.

In one of our works, silicon quantum dots (QDs) coated with a shell of silicon oxides (SiO_x , $0 < x < 2$) were obtained by γ -rays irradiation of an aqueous mixture of (3-Aminopropyl) trimethoxysilane (APTS) acting as a silicon precursor [17] (Fig. 16). The nanomaterials were found to be porous and amorphous with an average size of less than 2 nm. By varying the absorbed dose, the size of the QDs could be conveniently tuned. Further, the QDs displayed bright blue emission under UV light. Comprehensive investigations revealed the

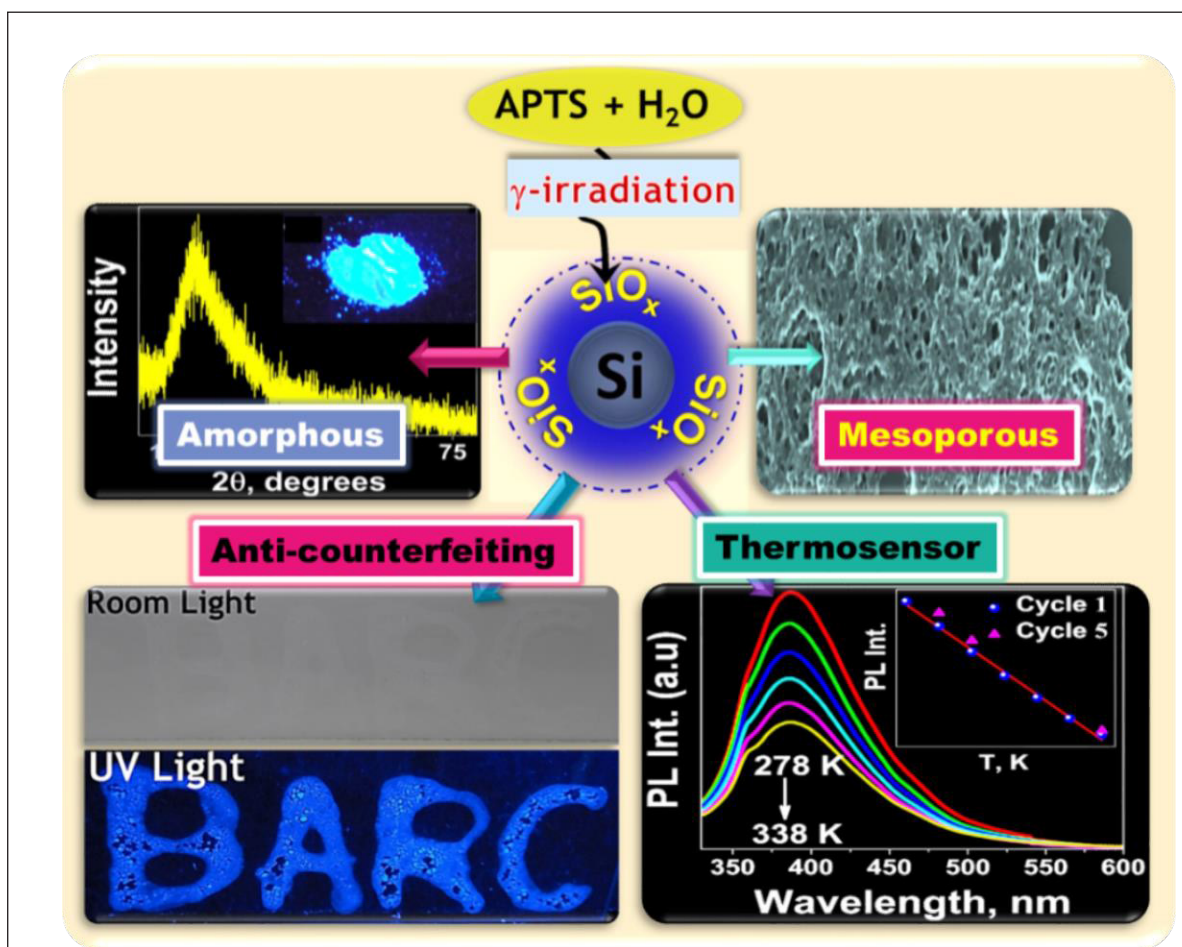


FIG 16. Schematic representation of the synthesis of silicon QDs (embedded within the SiO_x , $0 < x < 2$ shell) by γ -ray irradiation. Other highlights of this work, including blue emission, amorphous and porous characteristics, as well as the potential applications of these nanomaterials, are depicted [17].

origin of the blue photoluminescence attributed to defects located in the oxide shell as well as at/or near the Si/SiO_x interface. The QDs were found to be non-cytotoxic and showed highly sensitive and robust thermosensing properties. Further, the potential application of these QDs was demonstrated in anticounterfeiting measures.

In another work, photoluminescent organosilicon oxide nanoparticles (OSiNPs) in an aqueous solution were prepared by using an electron beam sourced from a 7 MeV linear accelerator (LINAC) [see Fig. 17A] [19]. This approach provides scope for the industrial-scale production of nanoparticles in a time-efficient manner without any involvement of toxic/hazardous capping or reducing agents. Furthermore, pulse radiolysis investigations were conducted to study the formation mechanism of OSiNPs. It was revealed that unlike the generally believed solvated electron (e⁻) driven process, the synthesis of OSiNPs proceeds through the reaction of the hydroxyl radical (•OH) with the precursor molecules. Apart from this, OSiNPs were functionalized with a biocompatible

ligand, i.e., L-Glutathione (L-Glu or GSH), which significantly enhanced the quantum efficiency (up to ~25%) of emission as well as colloidal stability. The applications of L-Glu@OSiNPs were demonstrated in fingerprinting (Fig. 17B) and cancer cell imaging (Fig. 17C). Nonetheless, it indicates their broad range of applications, which can be explored further as a replacement for toxic and costly materials currently used in the respective fields.

As mentioned earlier, the optical properties of silicon nanomaterials are highly sensitive to the nature of ligands present on their surface. Various biocompatible ligands such as cyclodextrin, polyethylene glycol (PEG), and Triton X-100 (TX-100) were used to functionalize the silicon nanomaterials. Importantly, functionalization was carried out *in situ* during the irradiation of the reaction mixture as a one-pot approach. As expected, the composition, as well as the photoluminescence properties of the nanomaterials obtained, were significantly different from each other while the same precursor (APTS) was used in the respective

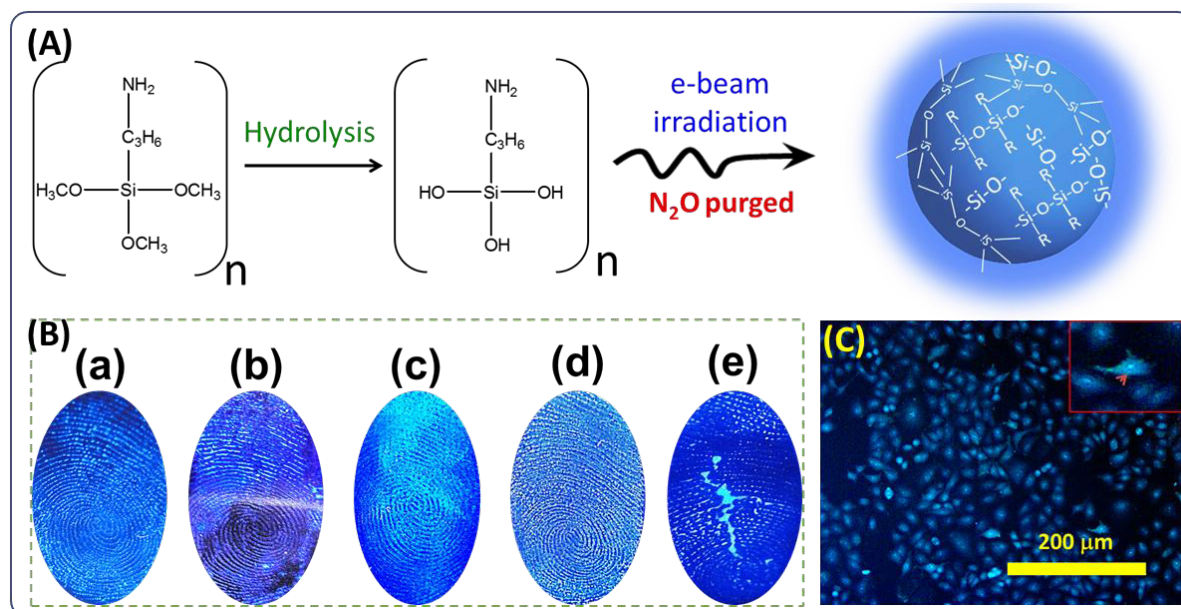


FIG 17. (A) Schematic representation of the formation of OSiNPs by electron beam irradiation. (B) Photographs of fingerprints (under UV light) developed with L-Glu@OSiNPs on various objects: (a) Aluminium foil, (b) glass cup, (c) CD/DVD, (d) aluminium metal sheet, and (e) plastic cover of a CD/DVD. (C) Fluorescence microscopy image using the colloidal solution of L-Glu@OSiNPs with pH ~6.5 in A549 lung cancer cells [19].

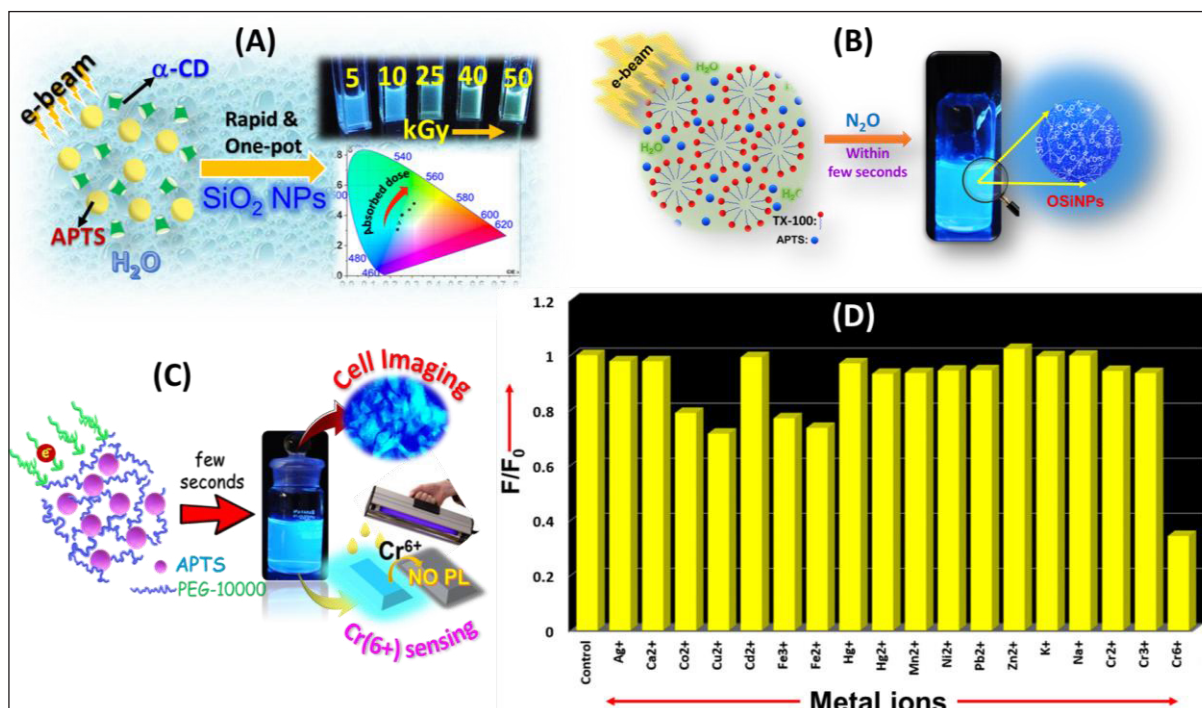


FIG 18. (A) Schematic representation of the radiation-assisted synthesis of α -CD@SiO₂ nanoparticles along with the absorbed dose-dependent photoluminescence tunability displayed by these nanoparticles [18]. (B) Schematic illustration of the electron-beam mediated synthesis of the blue light-emitting OSiNPs in the micellar medium of TX-100 [21]. (C) Schematic representation of the synthesis of PEGylated SiONCs by irradiation method along with their applications in cell imaging and Cr(VI) sensing [20]. (D) Plot of F/F₀ versus metal ions, showing maximum photoluminescence quenching of PEGylated SiONCs by Cr(VI) ions [20].

reaction mixtures. For instance, SiO₂ nanoparticles were formed in the presence of α -Cyclodextrin (α -CD). The photoluminescence properties of as-prepared α -CD functionalized SiO₂ nanoparticles (i.e., α -CD@SiO₂ NPs) could be tuned from blue to green by simply varying the absorbed dose (see Fig. 18A), and it was attributed to the formation of a particular kind of 'defects' at a proportionate absorbed dose [18]. The maximum quantum efficiency (QE) of α -CD@SiO₂ NPs was determined to be ~ 21 %. Using the micellar medium of TX-100, the photoluminescence QE of radiolytically synthesized OSiNPs enhanced from ~9 % to ~55 % (schematic illustration shown in Fig. 18B). Also, the nanoparticles were found to be comprised of siloxane/silicone and silica (SiO₂) like units as the major constituents [21]. In another work, the presence of PEG-10000 in the reaction mixture resulted in the formation of silicon oxide nanocomposites (SiONCs) on

irradiation (Fig. 18C). Various characterization studies indicated the presence of structures such as SiO_x (where x<2) and (Si(CH₃)₂-O)_n (as observed in polysiloxane) in the SiONCs. The maximum photoluminescence QE of SiONCs was determined to be ~49 %. In addition to the cell imaging applications, the PEGylated SiONCs showed highly sensitive and selective detection of Cr(VI) (detection limit = 0.74 μ M), as can be seen from Fig. 18D [20].

Si-based nanomaterials have attracted a lot of attention in the arena of nanoscience and nanotechnology. However, challenges are associated with their development, which may limit their practical applications. In this context, the radiation-assisted approach may contribute to a facile, eco-friendly, time-efficient, and cost-effective sustainable protocol for the preparation of photoluminescent water-soluble Si-based nanomaterials.

Nevertheless, various other semiconductor nanoparticles could also be synthesized through radiation induced methods in aqueous as well as organic solvents of choice. Moreover, instead of using multiple precursors, the radiation induced synthesis could also be performed with a single source precursor, where both the elements present in one organometallic compound. Such method is often considered as green route as there is no involvement of additional reducing agents and high temperature and hazardous experimental conditions. The synthesis could be scaled up for a large scale production of nanoparticles for industrial applications.

4. Conclusions and Future Scope

Semiconductor nanoparticles of different shapes and sizes of choice always remain the top priority as far as their applications are concerned. For example, nanorods, nanotubes, nanopetals, nanoflowers, nano-seaurchins, and many more such fascinating structures of very high surface to volume ratio are to be optimally synthesized for sensor and catalytic applications. Certain semiconductors like SnS_2/SnS , WS_2 can have fullerene like structures and called as inorganic fullerenes. Radiation-induced synthesis of such exotic nanoparticles are to be explored for their potential applications. Semiconductor nanoparticles in emerging media like deep eutectic solvents, room temperature ionic liquids, etc. needs to be understood for their future applications. The effect of extreme conditions like high temperature and high pressure, high bias voltage, etcon the formation of such nanoparticles could provide an insight into the geothermal conditions. In a similar line, the synthesis via low to moderate energy ionizing radiation will be very much useful in understanding their effect in biological media as well as upper atmosphere. It is needless to say that the exploration of radiation induced synthesis of semiconductor nanoparticles will always remain in demand in the years to come.

Acknowledgement

The authors thankfully acknowledges the members of the RPCD LINAC facility for their help in the pulse radiolysis and irradiation-based experiments. The authors would like to express gratitude for the support and inspiration received from both current and former colleagues of RPCD. The support and encouragement provided by Dr. Awadhesh Kumar, Head, RPCD, and Dr. A. K. Tyagi, Director, Chemistry Group, BARC is gratefully acknowledged.

References

1. C. N. R. Rao, A. Müller and A. K. Cheetham, eds., *The Chemistry of Nanomaterials*, Wiley-VCH Verlag GmbH & Co. KGaA, **2004**.
2. G.L. Hornyak, J.J. Moore, H.F. Tibbals, J. Dutta, *Fundamentals of Nanotechnology*, CRC Press, **2018**.
3. N. Baig, I. Kammakakam, W. Falath, *Mater. Adv.* **2021**, *2*, 1821-1871.
4. L.A. Kolahalam, I. V Kasi Viswanath, B.S. Diwakar, B. Govindh, V. Reddy, Y.L.N. Murthy, *Mater. Today Proc.* **2019**, *18*, 2182-2190.
5. S. Anu Mary Ealia, M.P. Saravanakumar, *IOP Conf. Ser. Mater. Sci. Eng.* **2017**, *263*, 32019.
6. F.P. García de Arquer, D. V Talapin, V.I. Klimov, Y. Arakawa, M. Bayer, E.H. Sargent, *Science* **2021**, *373*, eaaz8541.
7. J. Owen, L. Brus, *J. Am. Chem. Soc.* **2017**, *139*, 10939-10943.
8. K. Grieve, P. Mulvaney, F. Grieser, *Curr. Opin. Colloid Interface Sci.* **2000**, *5*, 168-172.
9. D. Bera, L. Qian, T.-K. Tseng, P.H. Holloway, *Materials (Basel)*. **2010**, *3*, 2260-2345.
10. J. Belloni, *Catal. Today.* **2006**, *113*, 141-156.
11. Q. Chen, X. Shen, H. Gao, *Adv. Colloid Interface Sci.* **2010**, *159*, 32-44.
12. A. Abedini, A.R. Daud, M.A.A. Hamid, N.K. Othman, E. Saion, *Nanoscale Res. Lett.* **2013**, *8*, 1-10.
13. M.C. Rath, Photo- and Radiation-Induced Synthesis of Nanomaterials BT - Handbook on Synthesis Strategies for Advanced Materials : Volume-I: Techniques and Fundamentals, in: A.K. Tyagi, R.S. Ningthoujam (Eds.), Springer Singapore, Singapore, 2021: pp. 623-656.
14. K. Čubová, V. Čuba, *Radiat. Phys. Chem.* **2020**, *169*, 108774.
15. K. Guo, A. Baidak, Z. Yu, Recent advances in green synthesis and modification of inorganic nanomaterials by ionizing and non-ionizing radiation, *J. Mater. Chem. A.* **2020**, *8*, 23029-23058.
16. S. Singh, A. Guleria, A.K. Singh, M.C. Rath, S. Adhikari, S.K. Sarkar, *J. Colloid Interface Sci.* **2013**, *398*, 112-119.
17. A. Guleria, S. Neogy, D.K. Maurya, S. Adhikari, *J. Phys. Chem. C.* **2017**, *121*, 24302-24316.
18. A. Guleria, A.P. Chavan, A. Tomy, C.M. Baby, S. Neogy, A.K. Debnath, S. Adhikari, *Ceram. Int.* **2020**, *47*, 2649-2655.

19. A. Guleria, A.P. Chavan, S. Neogy, V. V. Gandhi, A. Kunwar, A.K. Debnath, S. Adhikari, *ACS Appl. Nano Mater.* **2020**, 3, 5123–5138.
20. A. Guleria, V. V. Gandhi, A. Kunwar, S. Neogy, A.K. Debnath, S. Adhikari, *Colloids Surfaces A Physicochem. Eng. Asp.* **2022**, 640, 128483.
21. A. Guleria, A. Tomy, C.M. Baby, V. V. Gandhi, A. Kunwar, A.K. Debnath, S. Adhikari, *J. Mol. Liq.* **2021**, 334, 116072.
22. A. Guleria, J. Aishwarya, A. Kunwar, S. Neogy, A.K. Debnath, M.C. Rath, S. Adhikari, A.K. Tyagi, *Dalt. Trans.* **2022**, 52, 1036–1051.
23. A. Guleria, V. V. Gandhi, A. Kunwar, A.K. Debnath, S. Adhikari, *Dalt. Trans.* **2022**, 51, 6366–6377.
24. Singh, S., Rath, M. C., Singh, A. K., Mukherjee, T., Jayakumar, O. D., Tyagi, A. K., Sarkar, S. K., *Radiat. Phys. Chem.*, **2011**, 80, 736–741.
25. A. Guleria, J. Aishwarya, A. Kunwar, S. Neogy, A.K. Debnath, M.C. Rath, S. Adhikari, A.K. Tyagi, *Dalt. Trans.* **2023**, 52, 1036–1051.
26. J.W.T. Spinks, R.J. Woods, *An Introduction to Radiation Chemistry*, 3rd ed., John Wiley and Sons, New York, **1990**.
27. J. Grand, S.R. Ferreira, V. de Waele, S. Mintova, T.M. Nenoff.; *J. Phys. Chem. C* **2018**, 122, 12573–12588.
28. G.G. Flores-Rojas, F. López-Saucedo, E. Bucio, *Radiat. Phys. Chem.* **2020**, 169, 107962.
29. Z. Li, L. Peng, Y. Fang, Z. Chen, D. Pan, M. Wu, *Radiat. Phys. Chem.* **2011**, 80, 1333–1336.
30. L. Das, A. Guleria, S. Neogy, S. Adhikari, *RSC Adv.* **2016**, 6, 92934–92942.
31. Qiao, Z., Xie, Y., Huang, J., Zhu, Y., Qian, Y., *Radiat. Phys. Chem.* **2000**, 58, 287–292.
32. Ge, X., Ni, Y., Liu, H., Ye, Q., Zhang, Z., *Mat. Res. Bull.* **2001**, 36, 1609–1613.
33. Janata, E., Kelm, M., Ershov, B. G., *Radiat. Phys. Chem.* **2002**, 63, 157–160.
34. Singh, A., Tripathi, V. S., Neogy, S., Rath, M. C., *Mat. Chem. Phys.* **2018**, 214, 320–329.



Dr. Apurav Guleria, Scientific Officer/F in the Radiation and Photochemistry Division, Chemistry Group of BARC, works in the field of Radiation Chemistry and Nanomaterials. His research interests encompass radiation and photochemical investigations, primarily focused on microheterogeneous media like microemulsions, room temperature ionic liquids, and deep eutectic solvents. His research also includes the synthesis of nanomaterials/nanocomposites with novel features through green methodologies and high energy ionizing radiations for biomedical, optical, and sensing applications. He has published more than 50 research articles in peer reviewed national and international journals. Dr. Guleria is a recipient of “Young scientist award-2016” by Department of Atomic Energy and Young Associate, Maharashtra Academy of Sciences-2021.



Dr. M. C. Rath has obtained his M. Sc. degree in Chemistry from Utkal University, Bhubaneswar in 1990, and joined BARC in 1992 as a trainee officer in Chemistry and subsequently joined then Chemistry Division in 1993 after the completion of training. Since then, he has been working in the field of radiation and photochemistry and obtained Ph. D. degree from Mumbai University in 1999. He has worked for two years from 2001 to 2003 at JAIST, Japan in the field of carrier relaxation dynamics in semiconductor quantum well structures. He has been working in the field of radiation induced synthesis of various nanomaterials for more than two decades. His current research interests include free radicals assisted synthesis of chalcogenide, oxide nanomaterials and degradation of toxic chemicals, radiation chemical studies at high temperature high pressure, radiation chemistry of CO₂ and exotic solvents like deep eutectic solvents.



INDIAN SOCIETY FOR RADIATION AND PHOTOCHEMICAL SCIENCES

(Reg. No. 617/1985, GBBSD, Bombay; Trust No. F-10965)

Radiation & Photochemistry Division

Bhabha Atomic Research Centre, Mumbai - 400 085

Member Enrolment Form

1. Name in Block Letters:
2. Date of Birth:
3. Highest Academic Qualification:
4. Present Position:
5. Addresses:

Photograph

Office	Residence
Telephone	Telephone
E-mail	E-mail

6. Address for Correspondence: Office / Residence
7. Category of Membership Applied for: Annual / Life / Corporate member
8. Remittance: DD in favour of 'ISRAPS' payable at MUMBAI
For Bank Transfer:
A/c No.10536133801, SBI, BARC Branch, IFSC SBIN0001268
(e-mail the money transfer details along with the details requested above to israps.secretary@gmail.com and CC to jyotim@barc.gov.in)

Category	Fees	Admission fee	Total Amount
Annual	Rs 200/-	Rs 100/-	Rs 300/-
Life Member	Rs 2000/-	Rs 100/-	Rs 2100/-
Corporate Member	Rs 20000/-	Rs 1000/-	Rs 21000/-

9. Brief Resume of activities and research interests:
10. List of memberships of other professional bodies, if any:
11. List of prizes/awards/fellowships received, if any:
12. Number of Publications:

I agree to abide by the constitution and bye-laws, and rules and regulations of the SOCIETY.

Place:
Date:

Signature



Solvents For High Performance Liquid Chromatography (HPLC)

Salient Features

- High purity and UV transmittance
- Low levels of Non-volatile matter
- Low moisture content, acidity and alkalinity
- Low backgrounds free of additional peaks
- Lot-to-lot consistency
- Filtered through 0.2 micron filter
- Available pack sizes from ampules to 4L bottles
- Residue analysis by HPLC and 1H NMR



WATER LC/MS Grade

Salient Features

- Filtered through 0.1 micron filter
- Clear baseline with minimum UV absorbance
 - UV abs 210 nm – Max 2 mAU
 - UV abs 254 nm – Max 0.5 mAU
- Provides high sensitivity & resolution
- Low acidity, alkalinity and evaporation residue
- Offers consistent & reliable results in both ESI/APCI positive & negative ionization modes
- Packed in 1 L & 4 L amber colored glass bottles



GC-MS Grade Solvents

Salient Features

- High-grade purity for precise and reliable analyses.
- Ultra-low impurity levels to minimize interference in results.
- Specially formulated for Gas Chromatography-Mass Spectrometry applications.
- Excellent solvent properties for a wide range of compounds.
- Residue-free, ensuring minimal instrument contamination.
- Facilitates superior peak separation and detection sensitivity.
- Indigenously made and Advent is first to introduce GC-MS grade solvents, meeting the current highest industry needs.



AD TRACE® series of High Pure Acids for Trace Metal Analysis

Salient Features

- Used as digestion reagents for Trace metal Analyses (in AAS & ICP)
- Used for smelting and digestion in Environmental, Water and Food analyses
- Virgin material of highest quality used for processing
- Purified by redistillation through vacuum, achieving up to ppm/ppb level ionic impurities
- Analysed up to 80 individual cation and anion traces
- Packaged in compatible high-quality containers
- Produced and packed under class 100 cleanroom conditions
- **AD TRACE®** : Ideal for analyses in the ppm level
- **AD TRACE® G** : Impurities in the ppb range for high-precision analyses



GC-MS Premium Solvents

Salient Features

- Meticulously refined to achieve a purity level of 99.99%, ensuring minimal interference and accurate analysis.
- Experience reliable results with extremely-low levels of impurities, enhancing the precision and sensitivity of the Head-space Gas Chromatography (GC-MS) analysis.
- Each batch undergoes rigorous quality control measures to guarantee consistency and reliability across every analysis.
- Designed with low volatility to eliminate interference with the analysis of volatile compounds from your samples.



Low non-volatile (LN) Grade

Salient Features

- Least non-volatile impurities in solvents leads to proper characterisation through LC and NMR techniques of the research molecules in pharma, Agri-research and CRO applications.
- With extraordinary low non-volatile material, LN grade assures high yield and minimal impurities in product purification.
- Advent provides NMR test analysis on request to customers.
- Excellent consistency in product quality with batch-to-batch reproducibility for dependable results.



Pharmacopoeial Labelled Solvents

Product Name	USP	BP	EP	JP	Product Name	USP	BP	EP	JP
Acetic acid, glacial	✓	✓	✓	✓	Methanol	✓	✓	✓	✓
Acetone	✓	✓	✓	✓	N,N-Dimethylacetamide	✓	✓	✓	✓
Benzyl alcohol	✓	✓	✓	✓	Nitric acid	✓	✓	✓	✓
Chloroform	✓	✓	✓	✓	N-Methyl-2-pyrrolidone	✓	✓	✓	✓
Dichloromethane	✓	✓	✓	✓	2-Phenoxyethanol	✓	✓	✓	✓
Dimethyl sulfoxide	✓	✓	✓	✓	Propan-2-ol	✓	✓	✓	✓
Formaldehyde solution	✓	✓	✓	✓	Propyl-2-ol	✓	✓	✓	✓
Glycerol	✓	✓	✓	✓	Propylene glycol	✓	✓	✓	✓
Hydrochloric acid	✓	✓	✓	✓	Triethanolamine	✓	✓	✓	✓

- Salient Features**
- Labelled USP, BP, Ph. Eur., JP & IP solvents in customized packs
 - All Time Ready auditable facility
 - FDA approved cGMP compliant plant
 - Dossier (all documentary support & declarations) on customer's request



Conjugated Bile Salts

Conjugated bile salts, because of their physiologically important acid-base properties, are used as ingredients in microbiological culture media for dissolution testing of drugs (including in vitro & in vivo Bioequivalence studies) and other biological applications. ADVENT has been successful in synthesizing the following conjugated bile salts in Kg scale.



Sodium Lauryl Sulphate, 99% (HPLC)

Main Applications

- It is used in ion-pairing reversed-phase high-performance liquid chromatography in the separation of some isomeric and other closely related basic compounds in pharmaceutical analysis.
- Skin cleanser in topical applications
- Tablet lubricant (for dispersible tablets)
- Wetting agent in dentifrices (toothpastes)
- Releasing agent in suppositories and pessaries
- Dissolution/wetting agent in solid oral dosage forms
- Foaming / lathering agent in shampoos



Fmoc Amino Acids and short Peptides from ADVENT : Advanced Building Blocks for Peptide Synthesis

- Salient Features:**
- Optimized synthetic processes for Highest Purity
 - Characterized by analytical data such as Mass, IR, 1H NMR, SOR etc.
 - Absence of related interfering & isomeric impurities
 - Customized combinations of amino acids as per the end application
 - Available in Gram to Kg scale

Readily Available in Gram to Kg scale*:

Name of Fmoc Amino Acid	CAS No.	Name of Fmoc Amino Acid	CAS No.
Fmoc-Asn-OH	71989-16-7	Fmoc-β-Ala-OH	35737-10-1
Fmoc-Phe-OH	35661-40-6	Fmoc-Cys(Trt)-OH	103213-32-7
Fmoc-Pro-OH	71989-31-6	Fmoc-Gly-Gly-OH	35665-38-4
Fmoc-Gln-OH	71989-20-3	Fmoc-β-Ala-Gly-OH	NA
Fmoc-Gly-OH	29022-11-5	Fmoc-β-Ala-Cys(Trt)-OH	NA
Fmoc-Ala-OH	35661-39-3	Fmoc-Gly-Gly-Gly-OH	170941-79-4

*The list is not exhaustive and new Fmoc amino acids and short peptides are being added to the ever-expanding basket continually. Kindly send your queries to sales@adventchembio.com.

Working Standards for Amino Acids, their Fmoc & other derivatives and short Peptides

ADVENT CHEMBIO has a wide range of working standards of simple Amino Acids, their Boc/Fmoc/Cbz/Ester derivatives, and Fmoc-modified di- and tri-peptides etc. in its range to cater to their growing demands in Peptide Industry. These molecules, especially Fmoc amino acids & related peptides, possess eminent self-assembly features and have distinct potential applications due to their inherent hydrophobicity and aromaticity of Fmoc moiety, thus promoting the association of these bio-inspired building blocks.

Benefits:

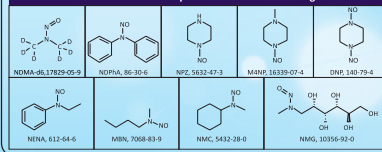
- Thoroughly analysed for Highest Purity
- Characterized by analytical data such as Mass, IR, 1H NMR, SOR etc.
- Absence of related interfering & isomeric impurities
- Customized combination of amino acids as per the end application
- Available in mg to g scale

N-Nitrosamine Impurities

Salient Features of ADVENT Nitrosamines:

- Available in high purity
- Ready stock
- Customized packs from mg to gram scale
- CoA is provided along with all characterization data such as Mass, IR, 1H NMR and 13C NMR etc.

Structures and CAS numbers of some representative Nitrosamines are given below:



W-279, TTC Industrial Area, MIDC, Rabale, Navi Mumbai-400 701, Maharashtra, INDIA.

+91 7777084837

sales@adventchembio.com

www.adventchembio.com



Copyright © ADVENT CHEMBIO PVT. LTD.

ART No: ACB/SD/5/091023-1



LASER SCIENCE

BRINGING TOMORROW'S TECHNOLOGY TODAY



ASTRELLA: ONE-BOX TI:SAPPHIRE AMPLIFIER



APPLICATIONS

- Time-resolved Spectroscopy
- Multidimensional Spectroscopy

CHAMELEON TI:SAPPHIRE



APPLICATIONS

- Multiphoton Excitation (MPE) Microscopy
- Non-linear Optics



AXON



APPLICATIONS

- Multiphoton Excitation (MPE) Microscopy
- Two Photon Polymerization

HARPIA - COMPREHENSIVE SPECTROSCOPY SYSTEM



APPLICATIONS

- Transient absorption and reflection in bulk and microscopy
- Multi-pulse transient absorption and reflection



www.laserscience.co.in



sales@laserscience.in



7710012972



[@laserscienceservices](https://www.linkedin.com/company/laserscienceservices)

<p>Smart Evaporator C1  BioChromato <i>Mining ideas, Aiding laboratories</i></p>  <ul style="list-style-type: none"> ❖ DMSO/DMF/water evaporation with no bumping ❖ Compatible with various containers ❖ Minimizes the loss by sample transfer ❖ Faster concentration with inert gas 	<p>Parts and components for Liquid Chromatography</p>  FLOM Japan  <p>For Enquires sales@anatekservices.com</p>	<ul style="list-style-type: none"> Single & Dual plunger pumps with SS, PEEK, PCTFE heads & Degasser Manual Injector for LC, solvent & Column switching valves LC Tubing and Fittings (ETFE, SUS, Peek)
 JEOL	 JASCO	<p>HiQ sil™ Japan HPLC Columns</p>  <p>C18 - C8 - C4 - C1 - CN Phenyl - NH2 - Silica</p>  SUNTEK
 <ul style="list-style-type: none"> ❖ GC AccuTOF™ ❖ GC - TQ MS ❖ GC-MS ❖ HR -MS ❖ DART - MS ❖ MALDI - TOF MS ❖ XRF Spectrometer <p>ANATEK SERVICES PVT. LTD.</p>	 <ul style="list-style-type: none"> ❖ UV Vis Spectrometer ❖ FTIR Spectrometer ❖ Fluorescence Spectrometer ❖ Digital Polarimeters ❖ Circular Dichroism Spectrometer ❖ Raman Spectrometer ❖ HPLC / UPLC / SFC <p>www.anatekservices.com</p>	



Quality Manufacturing Company

CONSULTANTS, ENGINEERS & FABRICATORS
MFGRS. OF : OPTO MECHANICAL COMPONENTS & LASER SYSTEMS
HIGH VACCUM ASSEMBLIES, COMPONENTS FOR IPIG & CPIG

Works : 5, Subhash Industrial Estate, Behind Saraf Kaskar Industrial Estate, Oshwara Bridge Lane, Off S. V. Road, Jogeshwari (W), Mumbai - 400 102.
 Regd. Off. : 53/15 B, Yashwant Nagar, Asha Wadi, Opp. Shopper's Stop, S. V. Road, Andheri (West), Mumbai - 400 058.
 Mobile : 9324484838 • Fax : (022) 2679 3373 • Email : qmc02@yahoo.co.in

 HV SWITCH	 AIR MONITORING SYSTEMS	 HIGH VOLTAGE S SHORTING DEVICE	 HV PNEUMATIC PRESSURE SWITCH
 VOLTAGE DIVIDER	 TAPERED TRANSFORMER	 LIQUID DIODE RESISTOR	 SHORTING DEVICE
			 ATTENUATORS AND INTEGRATORS



Educational & Research Aids Co.

42/402, Surya Niwas, L.T. Nagar Road No.3, M.G. Road, Goregaon (W), Mumbai - 400 104.

09326323661 / 9920018225 / 9769009152

info@eraco.in / sales.eraco@gmail.com @eraco2020

ANALYTICAL INSTRUMENTS



Analytical Weighing Balance



UV Spectrophotometer



Digital Water Bath



Kjeldhal Distillation



Ultra Centrifuge



Vacuum Cabinet Desiccator

LABORATORY CONSUMABLES



MICROPIPETTE TIPS



Nitrile Gloves



Laboratory Chemicals



Tissue Culture Ware



Laboratory glass ware



Filter Paper

LIFE SCIENCE SOLUTIONS



Bunsen Burner



Gel Documentation



DD PCR System



Incubator Shaker



Microscopes



Real Time PCR Machine



Nucleic Acid Extraction Machine



Centrifuge



Micropipette



Fermenter



Cell Culture Media



Ultra Low Deep Freezer



OUR PRODUCTS ARE AVAILABLE ON



AUTOMATED LIQUID HANDLING

“Era Is A One Stop Solution For All Your Educational, Research And Scientific Needs”

IT'S WHAT'S INSIDE THAT COUNTS...

SNR 10,000:1
UV-VIS-NIR measurement
TCSPC down to 25ps
Micro-PL upgrade



FS5



FLS1000

SNR 35,000:1
Hexagonal sample chamber
AGILE supercontinuum Laser
Customized design and configuration

Truly Confocal
Integrated narrowband Raman Laser
5 position grating turret
InGaAs array, CCD, EMCCD

RM5



RMS1000

Truly Confocal
Dual Spectrograph
Four simultaneous detector
FLIM, PL microscopy, Time-resolved



DISCOVER THE SPECTROSCOPY



ATOS



Fast IC MOS, EMCCD, CCD & PMT detectors, High resolution imaging spectrographs, Raman, Fluorescence, Micro spectroscopy (UV-VIS-NIR), Plasma spectroscopy

ATOSCOPE



Flow Cryostats for 3K and 77K measurements with ultra low vibration system. Cryogen free cryostats for 4K measurements for optical & transport experiments

CRYOSTATS - OPTICAL/ELECTRICAL/MAGNETIC MEASUREMENTS

4K Closed Cycle Cooling System with ultra low vibration, Custom design



ECDL TUNABLE DIODE LASERS LITTROW & LITTMAN, MOPA UP TO 4W

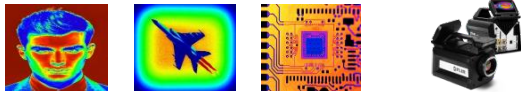
Absorption spectroscopy Rb, Cs, Li & K Tera Hertz & Quantum Cascade Lasers



IR THERMOGRAPHY CAMERAS



Temperature Measurement: - 80 °C to 3500 °C <20mK Sensitivity, World Best calibration



NEW COMPACT FT-IR SPECTROMETERS SOLIDS, LIQUIDS & GASES



Wide spectral ranges: 900nm - 16µm High resolution 4cm-1, up to 0.5 cm-1

THE WORLD'S FIRST TRULY TURN-KEY MULTI-PHOTON MICROSCOPE

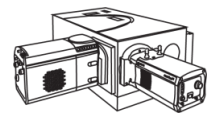
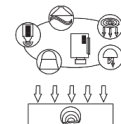
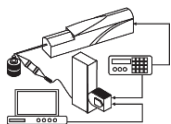
- Its Portable – No need of an optical table
- Plug & Play – Hassle free of maintenance.
- Inbuilt 700 -1300nm femtosecond fiber laser



ALL VERSION OF FIBER LASERS



3W Supercontinuum VIS-IR white light laser 15 Femtosecond, 950-1150 nm broad band laser



ATOS Instruments Marketing Services

ATOSCOPE Instruments Pvt. Ltd

www.atosindia.com

atos@atosindia.com